



CONTRACT NO. A932-161  
FINAL REPORT  
OCTOBER 1993

# Sensitivity of Flame Structure and Particulate Matter Emissions to the Operating Configurations of a Combustion Wind Tunnel

CALIFORNIA ENVIRONMENTAL PROTECTION AGENCY



AIR RESOURCES BOARD  
Research Division



Sensitivity of Flame Structure and Particulate Matter  
Emissions to the Operating Configurations  
of a Combustion Wind Tunnel

Final Report

Contract No. A932-161

*Prepared for:*

California Air Resources Board  
Research Division  
2020 L Street  
Sacramento, California, 95814

*Prepared by:*

B.M Jenkins  
I.M. Kennedy  
D.P.Y. Chang  
O.G. Raabe  
S.Q. Turn  
R.B. Williams  
S.G. Hall  
S. Teague

University of California, Davis  
Davis, California 95616

October 1993



**Determination of Emissions from Open Burning of Agricultural and Forestry Wastes:  
Flame Characterization**

***Sensitivity of Flame Structure and Particulate Matter Emissions to the  
Operating Configurations of a Combustion Wind Tunnel***

**Abstract**

Particulate matter (PM) emissions and flame structure were investigated for spreading fires in a combustion wind tunnel using rice straw. Four operating configurations were investigated. The wind tunnel configuration was modified by extending or retracting an overhead adjustable ceiling, and by adding or removing a sheet steel floor directly underneath the fuel bed. PM emission factor varied from 0.7% of fuel mass for a 2 m s<sup>-1</sup> wind speed and a configuration in which the ceiling was retracted and the floor was removed, to a low of 0.5% for a 3 m s<sup>-1</sup> wind speed with the floor added and the ceiling extended to just ahead of the flame. Flame structure was examined through measurements of local temperatures, gas concentrations, and soot volume, the latter obtained by laser light extinction. Flame temperature profiles were altered substantially by changing wind speed and ceiling position, but peak flame temperatures were similar. Wind speed was a dominant parameter affecting the emission of particles. Higher wind speeds gave greater mixing rates, with reduced flame lengths and flame residence times, and lower soot formation and PM emission. The floor was also observed to significantly influence particle emissions, possibly by restricting air flow through the smolder zone behind the fire, decreasing particle emission when present. Ceiling position by itself was not observed to significantly affect particle emission factor. Retracting the ceiling decreased streamwise air velocities and increased vertical velocities at the fire. Inlet velocity profiles with the ceiling retracted at low wind speed were distinctively different than at higher speeds or with the ceiling extended, suggesting flow separation due to an extremely adverse pressure gradient. Local turbulence intensities in the boundary layer were comparable with reported field values, as were surface roughness heights and friction velocities for the ceiling extended and the higher wind speed ceiling retracted configurations. Future experiments with spreading fires should make use of the ceiling extended high wind speed and ceiling retracted low wind speed configurations to evaluate the variability induced by the wind tunnel in emission factors of other species and with different fuels. Average values should be suitable for determinations of emission offset allowances.



## Table of Contents

	<u>page</u>
Abstract	2
List of Tables	4
List of Figures	5
Nomenclature	9
Introduction	11
Wind Tunnel Configurations	15
Materials and Procedures	16
Inlet velocities and turbulence characteristics	17
Particulate matter and particle size distributions	22
Time-temperature histories of the flame	24
Local flame temperatures	25
Flame radiation	26
Local gas concentrations	28
Soot volume	29
Operating conditions	31
Results	33
Inlet velocity profiles and turbulence characteristics	35
Ceiling extended configuration	35
Ceiling retracted configuration	36
Particle size distributions	61
Temperature profiles	62
Flame radiation	63
Local gas concentrations	72
Soot volume fractions	76
Discussion	76
Conclusions and Recommendations	84
Acknowledgements	86
References	87
Appendix	Vol. 2

## List of Tables

	<u>page</u>
1. Means of operating results for four configurations and two wind speeds.	34
2. Three-way incidence table on PM emission factor (% , number of experiments shown in parentheses).	34
3. Computed wind speed, boundary layer thickness, roughness height, and friction velocity.	55
4a. Particle size distributions for replicates of CEWF high wind speed configuration.	61
4b. Particle size distributions for replicates of CRNF low wind speed configuration.	61
5. Total emitted power, heat release, and fraction emitted as flame radiation.	71
6. Local gas concentrations, CEWF, high wind speed.	72
7. Local gas concentrations, CRNF, low wind speed.	73

## List of Figures

	<u>page</u>
1. Exterior schematic of combustion wind tunnel.	13
2. Schematic of the wind tunnel conveyor system.	14
3. Longitudinal schematic of wind tunnel showing approximate upstream and downstream positions used for anemometer probe traverses.	18
4. View across wind tunnel showing location of thermocouples in array.	25
5. Location of radiation sensor.	27
6. Transmission electron micrograph of soot particles collected from the flame region, 63 mm above the fuel surface, on a point to plane electrostatic precipitator. The length of the reference bar represents 250 nm.	32
7a. Streamwise velocity, CEWF, high wind speed, upstream position.	37
7b. Vertical velocity, CEWF, high wind speed, upstream position.	37
7c. Streamwise turbulence intensity, CEWF, high wind speed, upstream position.	38
7d. Vertical turbulence intensity, CEWF, high wind speed, upstream position.	38
7e. Streamwise velocity, CEWF, high wind speed, downstream position.	39
7f. Vertical velocity, CEWF, high wind speed, downstream position.	39
7g. Streamwise turbulence intensity, CEWF, high wind speed, downstream position.	40
7h. Vertical turbulence intensity, CEWF, high wind speed, downstream position.	40
7i. Streamwise velocity, CEWF, low wind speed, upstream position.	41
7j. Vertical velocity, CEWF, low wind speed, upstream position.	41
7k. Streamwise turbulence intensity, CEWF, low wind speed, upstream position.	42
7l. Vertical turbulence intensity, CEWF, low wind speed, upstream position.	42
7m. Streamwise velocity, CEWF, low wind speed, downstream position.	43
7n. Vertical velocity, CEWF, low wind speed, downstream position.	43

### List of Figures (con't)

7o.	Streamwise turbulence intensity, CEWF, low wind speed, downstream position.	44
7p.	Vertical turbulence intensity, CEWF, low wind speed, downstream position.	44
8a.	Streamwise velocity, CRNF, high wind speed, upstream position.	46
8b.	Vertical velocity, CRNF, high wind speed, upstream position.	46
8c.	Streamwise turbulence intensity, CRNF, high wind speed, upstream position.	47
8d.	Vertical turbulence intensity, CRNF, high wind speed, upstream position.	47
8e.	Streamwise velocity, CRNF, high wind speed, downstream position.	48
8f.	Vertical velocity, CRNF, high wind speed, downstream position.	48
8g.	Streamwise turbulence intensity, CRNF, high wind speed, downstream position.	49
8h.	Vertical turbulence intensity, CRNF, high wind speed, downstream position.	49
8i.	Streamwise velocity, CRNF, low wind speed, upstream position.	50
8j.	Vertical velocity, CRNF, low wind speed, upstream position.	50
8k.	Streamwise turbulence intensity, CRNF, low wind speed, upstream position.	51
8l.	Vertical turbulence intensity, CRNF, low wind speed, upstream position.	51
8m.	Streamwise velocity, CRNF, low wind speed, downstream position.	52
8n.	Vertical velocity, CRNF, low wind speed, downstream position.	52
8o.	Streamwise turbulence intensity, CRNF, low wind speed, downstream position.	53
8p.	Vertical turbulence intensity, CRNF, low wind speed, downstream position.	53
9.	Velocity profile, CEWF, with fire, high wind speed, upstream position, with logarithmic law-of-the-wall model shown for comparison ( $u^* = 0.61 \text{ m s}^{-1}$ , $z_0 = 0.05 \text{ m}$ ).	56

## List of Figures (con't)

10.	Non-dimensional velocity profiles for CEWF high wind speed and CRNF low wind speed configurations (data for zero pressure gradient and separating flows from reference 26, p 470).	57
11.	Energy spectrum, CEWF, with fire, high wind speed, upstream position (locations shown are height above rod conveyor).	59
12.	Energy spectrum, CRNF, with fire, low wind speed, upstream position (locations shown are height above rod conveyor).	60
13.	Temperature contours and relative frequency densities of temperature from fast response thermocouple at indicated positions in flame, CEWF high wind speed configuration. Contour interval = 100°C, height given above fuel surface.	64
14.	Temperature contours and relative frequency densities of temperature from fast response thermocouple at indicated positions in flame, CRNF low wind speed configuration. Contour interval = 100°C, height given above fuel surface.	65
15.	Temperature profiles showing mean and standard deviation for the CEWF high wind speed configuration. (a) upwards through flame center, (b) upwards over glowing combustion zone.	66
16.	Temperature profiles showing mean and standard deviation for the CRNF low wind speed configuration. (a) upwards through flame center, (b) upwards over glowing combustion zone.	67
17.	Temperature contours and relative frequency densities of temperature from fast response thermocouple at indicated positions in flame, CENF high wind speed configuration. Contour interval = 100°C, height given above fuel surface.	68
18.	Temperature contours, field burn in rice straw spreading against the wind (Contour interval = 100°C).	69
19.	Flame radiation for four configurations. (a) low wind speed, (b) high wind speed (see Figure 5 for definition of D).	70
20.	Radiation emitted as a fraction of total fire heat release.	71
21.	Gas concentration profiles for the CEWF high wind speed configuration. (a) upwards through the flame center, (b) upwards over the glowing combustion zone.	74
22.	Gas concentration profiles for the CRNF low wind speed configuration. (a) upwards through flame center, (b) upwards over glowing combustion zone.	75

**List of Figures (con't)**

- |     |  |    |
|-----|--|----|
| 23. | Profiles of soot volume fraction for five streamwise positions. (a) CEWF high wind speed, (b) CRNF low wind speed. Positions shown are distances downstream from the leading edge of the fire. | 77 |
| 24. | Estimated fluid time scales based on integral length scales and velocity fluctuations for the CEWF high wind speed and CRNF low wind speed configurations.                                     | 80 |

## Nomenclature

$a$	empirical constant of King's law equation	
$b$	empirical constant of King's law equation	
$D$	particle diameter	$m$
	distance from fire front to flame radiation sensor	$m$
$\mathcal{D}$	diffusivity	$m^2 s^{-1}$
$Da$	Damköhler number	
$E$	spectral energy	$m^3 s^{-2}$
$E_{ci}$	corrected voltage based on temperature of anemometer	$V$
$E_j$	uncorrected voltage signal from anemometer	$V$
$E_k$	turbulence kinetic energy	$m^2 s^{-2}$
$f$	frequency	$s^{-1}$
$f_s$	sampling frequency	$s^{-1}$
$I$	attenuated light intensity as photodiode output	$V$
$Im$	imaginary part of complex number	
$I_0$	unattenuated light intensity as photodiode output	$V$
$I_u$	local streamwise turbulence intensity	
$I_v$	local vertical turbulence intensity	
$j$	sample number	
$k_{ext}$	extinction coefficient	$m^{-1}$
$\ell$	integral length scale	$m$
$L$	path length for laser light (width of tunnel)	$m$
$MMAD$	mass median aerodynamic diameter	$m$
$m$	refractive index of particles	
$N$	total number of samples	
	particle concentration	$m^{-3}$
$Nu$	Nusselt number	
$n$	empirical constant of King's law equation	
$Re_\ell$	Reynolds number based on integral length scale	
$R_s$	Reynolds stress	$N m^{-2}$
$R_{u'u'}$	autocorrelation coefficient on $u'$	
$r$	separation distance	$m$
$t$	time	$s$
$T_{cal}$	calibration air temperature for anemometer	$K$
$T_e$	air temperature at anemometer during testing	$K$
$T_s$	anemometer wire temperature	$K$

## Nomenclature (con't)

$U$	time averaged streamwise velocity	$m\ s^{-1}$
$u$	instantaneous streamwise velocity	$m\ s^{-1}$
$u'$	streamwise velocity fluctuation	$m\ s^{-1}$
$u^*$	friction velocity	$m\ s^{-1}$
$V$	time averaged vertical velocity	$m\ s^{-1}$
$v$	instantaneous vertical velocity	$m\ s^{-1}$
$v'$	vertical velocity fluctuation	$m\ s^{-1}$
$x$	longitudinal position	$m$
$z$	height	$m$
$z_0$	surface aerodynamic roughness height	$m$
$\alpha$	size parameter, $\pi D/\lambda$	
$\Delta y$	flame thickness	$m$
$\phi$	soot volume fraction	
$\eta$	Kolmogorov length scale	$m$
$\kappa_1$	longitudinal wavenumber	$m^{-1}$
$\lambda$	wavelength of incident light	$m$
$\nu$	kinematic viscosity	$m^2\ s^{-1}$
$\rho$	density	$kg\ m^{-3}$
$\sigma_g$	geometric standard deviation	
$\sigma_T$	non-dimensional heat release rate	
$\sigma_{u'}$	standard deviation of $u'$	$m\ s^{-1}$
$\tau$	time lag	$s$
$\tau_C$	characteristic chemical reaction time scale	$s$
$\tau_F$	characteristic fluid time scale	$s$
$\chi_{st}$	scalar dissipation rate at stoichiometric location	$s^{-1}$

### Wind Tunnel Configurations:

<b>CENF</b>	Ceiling extended, no floor
<b>CEWF</b>	Ceiling extended, with floor
<b>CRNF</b>	Ceiling retracted, no floor
<b>CRWF</b>	Ceiling retracted, with floor

## **Introduction**

In 1983, California enacted legislation (AB 1223) allowing emission offset credits to facilities that would burn agricultural and forest biomass (crop and forest residues) for the generation of steam and electricity. In enacting AB 1223, the legislature recognized the potential for reducing air pollution from the open burning of waste materials when these same materials are used as fuel for power plants. Each year, farmers burn approximately  $1.7 \times 10^6$  metric tons (dry basis) of crop residues in the state (1, 2). Many types of crop residues are burned, but the most important contributions to air pollution come from rice straw, almond and walnut tree prunings, and wheat straw, which together account for about 95% of the agricultural biomass burned (1). More recent legislation restricts the amount of rice straw which can be burned in the field, but retains the emission offset allowance for facilities that use it as fuel.

The procedure for determining the emission offset credits developed under the initial legislation has subsequently been modified, but it still involves the use of so-called emission factors for each type of fuel considered by each facility. For each pollutant, a quantity expressing the mass of pollutant emitted per unit mass of fuel burned (called the emission factor) is required for the procedure. Darley (3, 4, 5) used a laboratory burning tower to obtain estimates of pollutant emission factors for a large number of crop residues. Emission factors have also been reported in the compilation by EPA (6). Some uncertainty exists in these laboratory results because of the high temperatures maintained in the sampling duct above the fire, and because of the small quantity of fuel burned. Field studies (e.g. 7, 8, 9) rely on elemental mass balances (generally carbon balances) to relate pollutant concentrations measured in the sample volume to the mass of fuel burned, and so to determine the emission factors. Emission factors determined in this way are sensitive to the concentration of CO<sub>2</sub> measured in the plume of the fire, and this is one of the reasons that results from field studies vary widely.

To update pollutant emission factors, a combustion wind tunnel was developed at UC Davis (10, 11). The emission factors are determined directly, and the tunnel allows different inlet air flow rates and velocity profiles to be used. A system of conveyors continuously moving fuel into the fire zone provides extended sampling times when testing spreading fires. As with Darley's experiments, a full simulation of the field conditions is not possible in the wind tunnel. There are several features of the design, however, which

can be adjusted to change the operating configuration of the wind tunnel. This report describes a series of experiments conducted to assess the effect of the different configurations on the fire structure and particulate matter emissions for a fire spreading through rice straw. In trying to assess the effect of the tunnel configurations on the fire behavior, one objective was to try to retain fuel properties, loading rate, and bed structure constant. The results reported here were therefore intended to pertain to the variations in particulate matter emission rates due to changes in the wind tunnel configuration, and not to changes in the fuel condition (e.g. moisture content).

The wind tunnel is an open-circuit, forced-draft type consisting of a fuel feed table, inlet section, combustion test section, and stack sampling section. The air flow is produced by a 45 kW centrifugal blower. Maximum air speeds (duct flow rate divided by duct area) of  $10 \text{ m s}^{-1}$  are possible, but in the set of tests described here, speeds under  $4 \text{ m s}^{-1}$  were used. Such velocities were found in field measurements to be typical of the average wind velocity in the first 1 m above the straw layer during open burning (10). The tunnel flow is straightened with a series of wire mesh screens located downstream of the blower. Details of the tunnel construction are given in (10). A schematic of the wind tunnel appears in Figure 1.

The conveyor system is used with spreading fires to translate the fuel bed downstream at a rate equal to the upstream fire spreading rate. The wind tunnel has so far only been used to simulate fires spreading against the wind ("backing" fires). Wind-aided fires ("heading" fires) generally spread at rates in excess of the maximum speed of the conveyor, and there is no provision to load fuel for fires of this type. The opposed flow condition is consistent with state regulations concerning field burning, although in practice many fields are burned with some combination of backing and heading fires. The wind tunnel is therefore limited in the extent to which it can simulate actual field conditions. Fields are not normally burned by a single fire line spreading upwind, as the spreading rates are rather slow, and the burn duration long. Instead, multiple fire lines are lit parallel to the wind direction (strip light), so that the fires spread principally in opposition to the wind but the total length of time to burn the field is reduced considerably.

The simulation is also limited by how well the fuel bed structure in the tunnel compares with that in the field. No attempt was made to try to reproduce all the possible fuel bed conditions found in the field. Instead, two configurations of the wind tunnel floor beneath the fuel bed were used to represent the cases of a straw layer resting on top of uncut

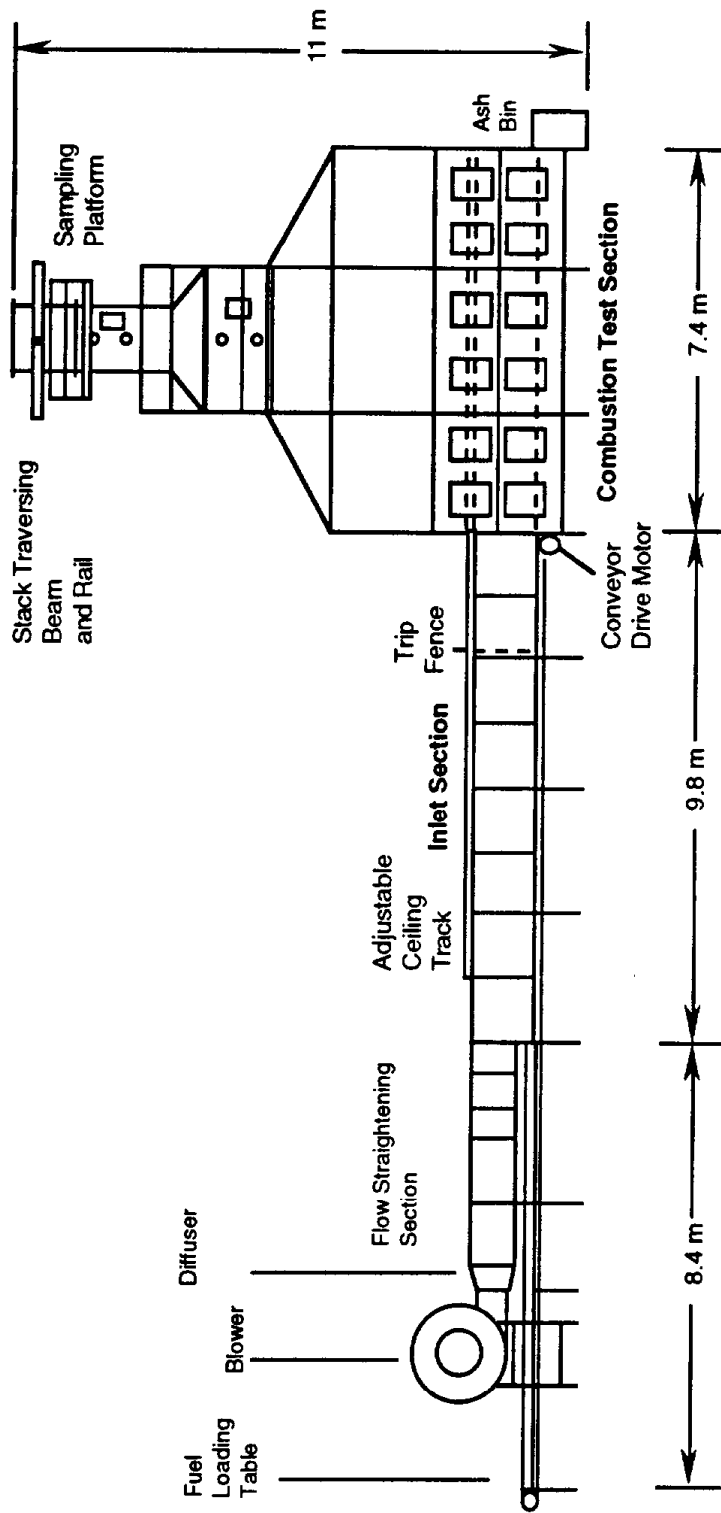


Figure 1. Exterior schematic of combustion wind tunnel.

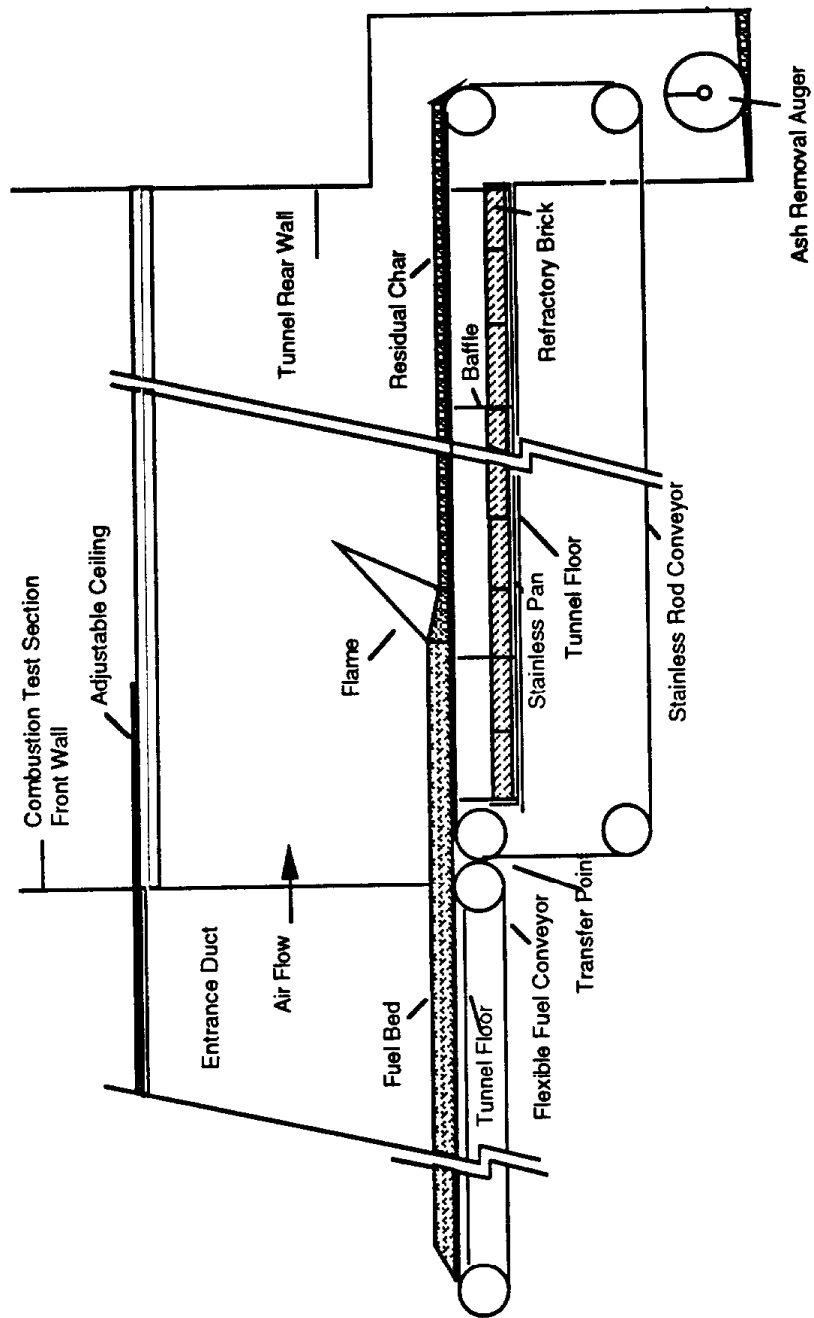


Figure 2. Schematic of wind tunnel conveyor system.

stubble, and the straw layer resting on the ground, as when the harvester is cutting in lodged or down rice.

Two conveyors are used in the tunnel. In the inlet flow development section, a flexible belt conveyor extends from the fuel loading table, where it is exposed for loading, to the junction with the combustion test section. This conveyor passes under the blower and flow straightening section, and joins the air flow 8 hydraulic diameters upstream of the combustion test section. At the front of the combustion test section, the fuel is transferred to a stainless steel rod conveyor that runs the full length of the test section. The fuel is burned on this conveyor. Both conveyors are driven at the same linear speed by a single variable speed DC motor. The rod conveyor is located 150 mm above a refractory brick floor, and unloads into an ash bin at the end of the combustion test section. Ash is removed from the bin by a motor driven auger emptying into a collection bag. The rod conveyor returns to the front of the combustion test section underneath the tunnel floor. Twelve windows are located along the length of the combustion test section on each side, and there is one window in the rear wall. Lower pairs of windows along the sides are located in doors hinged at the top. Access to the test section is through these doors.

A movable ceiling extends horizontally into the combustion test section from the front wall and can be positioned anywhere along the test section to aid in shaping the inlet velocity profile. The inlet section is 1.2 m square, and the ceiling is located at a height just above the top of the inlet section. A schematic of the conveyor and ceiling arrangement is given in Figure 2.

Above the test section, the stack tapers upwards in two stages to a final 1.2 m square cross section. The sampling plane is approximately 9.8 m above the top surface of the rod conveyor, and is located 2 duct widths downstream and 0.5 duct widths upstream from the nearest flow disturbance. Stack samples are collected with a track-mounted traversing platform (Figure 1).

### **Wind Tunnel Configurations**

The operating configurations of the wind tunnel were altered by adjusting the position of the movable ceiling above the fire, and by installing a sheet metal floor directly beneath the fuel bed and rod conveyor to block ventilation from below. With these two adjustments, four configurations were possible:

1) ceiling extended downstream to the front or leading edge of the fire, with no floor installed between the fuel bed and the refractory brick (designated CENF for ceiling extended, no floor),

2) ceiling retracted to the front wall of the combustion test section, with no floor installed (designated CRNF for ceiling retracted, no floor),

3) ceiling extended to the front edge of the fire, with the floor installed beneath the fuel bed from the entrance of the combustion test section to approximately 4 m downstream of the entrance (designated CEWF for ceiling extended, with floor), and

4) ceiling retracted to the front wall, with the floor installed (designated CRWF for ceiling retracted, with floor).

Two wind speeds were also tested--a low wind speed of about  $2 \text{ m s}^{-1}$ , and a higher wind speed of  $3$  to  $3.5 \text{ m s}^{-1}$ , where the wind speed is the superficial velocity in the inlet duct, i.e., the volumetric flow rate divided by the duct cross sectional area. The air flow rate was adjusted by changing the vane angle and effective aperture on the inlet vanes of the blower. For each experiment, the fire was either held at the second window, approximately 2 m downstream of the entrance to the combustion test section, or was allowed to spread upstream from the third window to the first window, approximately 3.5 to 1 m from the test section entrance (Figure 1).

## Materials and Procedures

For each operating configuration, measurements were made to describe the approach flow, flame structure, and particulate emissions. The approach flow velocity profiles and turbulence characteristics were determined using a two-wire x-probe type hot-film anemometer. Particulate matter (PM) concentrations were determined using an in-stack sampling method based on CARB method 17 (12). Particle size distribution was determined with a cascade impactor, also used in-stack. Flame structure was analyzed by measuring flame temperatures, flame radiation, and local gas concentrations. Average line-of-sight soot volume concentrations were determined by laser light extinction through the flame and post-flame regions. Fuel moisture content and residual ash weight were determined for each experiment. Fuel loading rate was constant at  $680 \text{ g m}^{-2}$  wet basis. Inlet air temperature and relative humidity, conveyor speed, stack gas velocity, and stack gas temperature were continuously recorded.

Due to instrument limitations, not all measurements could be made simultaneously, and repeated tests were conducted with all controlled variables held constant. Measurements of PM and operating parameters were always taken, the PM results serving as a means of evaluating repeatability. Each test was replicated. A total of 64 experiments were conducted, 19 in the CRNF configuration, 17 in the CENF configuration, 15 in the CEWF configuration, and 13 in the CRWF configuration.

#### Inlet velocity profiles and turbulence characteristics:

A two-axis, x-probe type hot-film anemometer (TSI model 1246-20, St. Paul, MN)\* coupled to two anemometer signal conditioners (Dantec model 56C17, Skovlunde, Denmark) was used to measure the inlet flow field along vertical center lines at two separate positions upstream of the fire. The first vertical traverse was taken 120 mm upstream of the front or leading edge of the fire. A second vertical traverse was made approximately 600 mm upstream of the leading edge of the fire. The first position closest to the fire was designated the downstream position, while the second position was designated the upstream position. The absolute positions of the probe were in all cases the same. The two positions are illustrated in Figure 3. At the downstream position with a fire present in the tunnel, the flow could not be probed near the fuel surface because of possible damage to the anemometer caused by the flame. Velocity measurements were also made in cold flow without the fire present, with the probe at the same absolute positions, and in this case descending to the fuel surface at the downstream position. The probe was oriented to measure both the streamwise and vertical velocity components of the flow. Full details of the procedures used are included in (13).

The anemometer was routinely calibrated over a range of 0.15 to 5.5 m s<sup>-1</sup> with a bench top calibration wind tunnel (TSI model 8390, St. Paul, MN). Analog outputs from the signal conditioners were converted to digital form by a 12 bit A/D board (GW Instruments model Macadios II Se, Somerville, MA) and stored on a microcomputer. The voltage signal was converted to velocity by fitting a King's law equation:

$$E_i^2 = a + bu_i^n \quad [1]$$

---

\* Mention of specific products or tradenames does not constitute an endorsement by the University of California.

where  $E_i$  is the voltage,  $a, b,$  and  $n$  are empirical constants, and  $u_i$  is the velocity in the  $i$ th direction. Separate equations were determined and used for each velocity component. Temperature at the probe was monitored with a bare bead, Inconel clad (0.5 mm diameter) type K (chromel-alumel) thermocouple placed 20 mm downstream of the tip. A corrected transducer voltage was computed from the deviation of actual air temperature from calibration air temperature as:

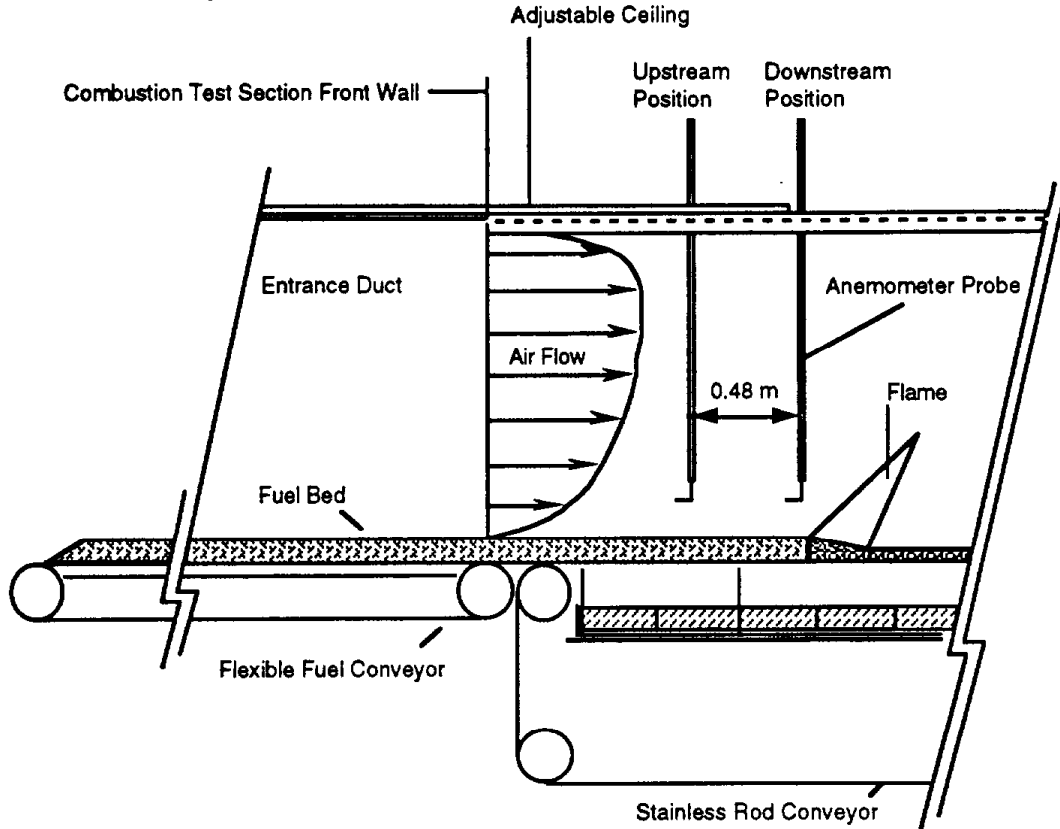


Figure 3. Longitudinal schematic of wind tunnel showing approximate upstream and downstream positions used for anemometer probe traverses.

$$E_{ci} = \left( \frac{T_s - T_{cal}}{T_s - T_e} \right)^{1/2} E_i \quad [2]$$

where  $E_{ci}$  is the temperature corrected voltage,  $E_i$  is the original uncorrected voltage,  $T_s$  is the sensor temperature (250°C),  $T_{cal}$  is the air temperature during calibration, and  $T_e$  is the test air temperature. After correcting for temperature, the streamwise and vertical velocities

were computed from vector sums on the effective velocities normal to each wire. For all tests,  $T_{cal}$  remained nearly constant at 27°C, and  $T_e$  varied between 19 and 42°C.

The anemometer probe was mounted facing upstream on the vertical arm of a stepper motor controlled positioning system capable of traversing the height of the combustion test section up to 1.2 m and 0.48 m in the streamwise direction (see Figure 3). Each traverse consisted of 15 to 18 sample locations spaced from 0.09 to 1.2 m above the surface of the rod conveyor (see Figures 7 and 8 for actual positions). The lowest point sampled was normally 30 to 60 mm above the mean fuel surface. Individual fuel elements often extended above this height, and care had to be taken to avoid breaking the wires on these fuel pieces when the conveyors were moving. At each location, a burst of 8,500 samples from each channel was acquired at 2.2 kHz for approximately 3.9 seconds. The sampling rate was selected to be in excess of the Nyquist criterion based on the frequency spectrum of the flow obtained initially on a Wavetek model 5820B spectrum analyzer (see also frequency spectra in results section). For the velocities tested, the highest observed frequency was in the neighborhood of 800 Hz. The sampling time was adequate to yield average velocities deviating less than one percent from sampling times greater than five seconds. Computer memory limitations required transferring data from each burst to disk before starting another burst. The sampling time was selected to enable a traverse to be completed in a reasonably short interval (~0.5 h). Replicated traverses were made at each position for each of the configurations, each of the two wind speeds, with and without a fire present in the wind tunnel. Mean velocities and local turbulence intensities were computed at each sampling location for both the streamwise and vertical directions. The turbulence intensities were computed in the normal manner whereby the instantaneous velocity is decomposed into a mean velocity and fluctuation:

$$u'(j) = u(j) - U \quad [3]$$

$$v'(j) = v(j) - V \quad [4]$$

where  $u(j)$  and  $v(j)$  are the streamwise and vertical instantaneous velocities, respectively, at sample number  $j$ ,  $U$  and  $V$  are the time averaged quantities of  $u(j)$  and  $v(j)$ , respectively, and  $u'(j)$  and  $v'(j)$  are the fluctuations from the means. The turbulence intensity is defined

for each velocity component as the root mean square of the fluctuations referenced to a characteristic mean flow velocity. In the streamwise direction,

$$I_u = \frac{(\overline{u' u'})^{1/2}}{U} \quad [5]$$

and in the vertical direction,

$$I_v = \frac{(\overline{v' v'})^{1/2}}{U} \quad [6]$$

where  $I_u$  and  $I_v$  are the streamwise and vertical turbulence intensities, respectively. The overbar denotes the time average of the quantity. Thus,

$$\overline{u' u'} = \frac{\sum_{j=1}^N (u' u')}{N} \quad [7]$$

where  $N$  is the number of data points in the sample ( $N=8500$ ). The turbulence intensities given by equation [5] and [6] are referred to as local turbulence intensities because  $U$  is the local average streamwise velocity measured at the same time and location as the fluctuations.

The Reynolds stress was calculated from the streamwise and vertical velocity fluctuations for the purposes of estimating boundary layer thickness,

$$R_s = -\rho \overline{u' v'} \quad [8]$$

Estimates of the aerodynamic roughness height,  $z_0$ , and friction velocity,  $u^*$ , were also made. In the overlap layer, between the wall layer and outer layer of the boundary flow, a logarithmic law-of-the-wall model describes the velocity:

$$U = \frac{u^*}{k} \ln\left(\frac{z}{z_0}\right) \quad [9]$$

where  $k$  is von Karman's constant,  $k=0.41$ , and  $z$  is the height. When the measured velocities are plotted against  $\ln(z)$ , and a line is fit through the portion of the profile near the fuel surface, the friction velocity,  $u^*$ , is determined from the slope and the roughness height,  $z_0$ , is determined from the intercept.

Energy spectra were derived from fast Fourier transforms (FFT) of the velocity data. Measures of the integral length scales of wind tunnel turbulence were derived from autocorrelations of the same data. The energy spectra were determined as functions of the longitudinal wavenumber,  $\kappa_l$  ( $m^{-1}$ ),

$$\kappa_l = \frac{2\pi f}{U} \quad [10]$$

where  $f$  is the frequency ( $s^{-1}$ ) of the turbulent fluctuations given from the FFT. The lower values of  $\kappa_l$  represent long wavelengths or large eddies, which contain most of the energy, and this region is generally classified as the production range in a typical energy spectrum (14). The integral length scale is associated with the wavenumber at the peak energy in this range. The viscous dissipation range occurs at high wavenumbers. The Kolmogorov length scale,  $\eta$ , is found in this range. Intermediate to these two ranges is the inertial subrange. The energy,  $E$ , in this range is proportional to  $\kappa_l^{-5/3}$ , and a plot of  $\ln(E)$  against  $\ln(\kappa_l)$  should yield a  $-5/3$  slope if the turbulence is well developed.

The integral length can also be found from an autocorrelation on the longitudinal velocity fluctuation through application of Taylor's hypothesis (15). The autocorrelation coefficient,  $R_{u'u'}(\tau)$  on  $u'$  was computed as

$$R_{u'u'}(\tau) \equiv \frac{\overline{u'(x_i = 0, t)u'(x_i = 0, t + \tau)}}{(\sigma_{u'})^2} \quad [11]$$

where  $t$  is time (s), and  $\tau$  is the time lag equal to  $j/f_s$  where  $j$  is the sample number from the start of sampling, and  $f_s$  is the sampling frequency ( $s^{-1}$ ). The parameter  $x$  defines the longitudinal position of the probe, which in this case was invariant for each sampling position. The parameter  $\sigma_{u'}$  is the standard deviation of the longitudinal velocity fluctuation,  $u'$ . The time lag is related to the separation in space,  $r$  (m), under the assumption of frozen turbulence by Taylor's hypothesis,  $r = U\tau$ . The integral length scale was computed by integrating equation [11] over  $r$  up to the first zero crossing for  $R_{u'u'}$  positive.  $R_{u'u'}$  is by definition unity at zero lag.

#### Particulate matter and particle size distribution:

Emission factors for particulate matter (PM) were used to measure gross changes in emission characteristics as a result of changes in the wind tunnel operating configuration. PM was determined in a manner similar to that described under the California Air Resources Board Method 17 in-stack sampling protocol (12). The test procedure deviated from the standard method in two aspects. The stack traverse utilized a smaller number of traverse points than called for by CARB Method 1 (referred to by Method 17), and the weight of PM cleaned from the probe nozzle was not determined after initial attempts failed to recover accurately measurable amounts. The nozzle was simply cleaned between runs. Particle size distribution was determined using a cascade impactor (Sierra Instruments model 228, Carmel Valley, CA) in the stack.

The stack cross section was divided into twelve equal rectangular areas each 305 mm by 406 mm. Although for the conditions of the stack CARB Method 1 specifies 24 or 25 traverse points, twelve was thought to be adequate for these relative comparisons after testing against a single point measurement at the center of the stack. Because the flow was fully turbulent in the stack, PM concentration was rather uniform across the stack. Two tests on two different days of the 12 point traverse against a single center point measurement on 48 minute runs produced concentrations of 10.05 and 12.61  $mg\ m^{-3}$  for the traverse and 10.35 and 12.59  $mg\ m^{-3}$  for the single point determination. The values appeared to be quite close given the variability in fire conditions that can occur between runs.

Samples were drawn at the center of each area, with 4 longitudinal positions and 3 transverse positions. The PM and cascade impactor probes, along with a type-K thermocouple (ungrounded, Inconel sheathed with 1.5 mm outside diameter) for

monitoring stack gas temperature and a single axis hot-film anemometer (Kurz Instruments model 455, Carmel Valley, CA) for monitoring stack gas velocity, were carried on a 100 mm by 75 mm rectangular steel beam which could be extended into the tunnel from the side wall. The beam itself was carried on a rail at the wall and could be moved along the wall. By moving the beam longitudinally and extending it transversely, the probes could be positioned at the different traverse points in the stack. When fully extended to the innermost traverse points, the beam and probes occupied less than 5% of the stack area. A sheet steel curtain moving with the beam kept the stack wall closed against gas leakage at all probe positions.

The PM probe consisted of a 12.7 mm stainless steel tube extending through the beam to which a 47 mm stainless steel filter holder and stainless steel buttonhook nozzle were attached. The inside diameter of the nozzle was 9.5 mm. A teflon tube was attached between the outer end of the stainless tube and the inlet of an impinger train. The impingers were connected through a check valve to an air tight sample pump, dry test meter, and mass flow meter. A thermocouple was used to continuously record impinger outlet temperature. The system was leak checked with each test. A vacuum gauge was connected ahead of the pump to monitor filter pressure drop. The standard S-type pitot tube was replaced with the calibrated hot film anemometer because the flow dynamic pressure was too low to accurately gauge gas velocity. The stack velocity was observed manually by the operator at the sampling platform, and was also continuously recorded electronically. This anemometer was calibrated when clean, and checked after operating in the stack flow. The probe retained calibration within 0.3% over all 64 tests. The probe operator read stack velocity and manually adjusted probe flow rate to maintain isokinetic conditions.

The cascade impactor was mounted alongside the PM probe, and also employed a stainless steel buttonhook nozzle. The nozzle inside diameter was 12.7 mm. Clearances between all probes were maintained in accordance with CARB method 2 (12). The outlet of the cascade impactor was connected to a stainless steel tube passing through the carrier beam, a desiccant column, air tight sample pump, dry test meter, and orifice meter. This system was also leak checked with each test. As with the PM probe, the operator adjusted flow to maintain isokinetic conditions.

Typical flow rates were 10 L min<sup>-1</sup> for the PM probe, and 20 L min<sup>-1</sup> for the impactor. PM samples were collected on weighed, desiccated, glass fiber filters (Gelman Sciences type

A/E, Ann Arbor, MI). Coated stainless steel membranes were used as collection surfaces in seven stages of the cascade impactor, with a glass fiber final filter. Total sampling duration was 48 minutes, with 4 minutes at each traverse location. After each 48 minute run, filters were removed, sealed in plastic filter cases, and taken to the laboratory. Filters were desiccated for 24 hours, and weighed.

#### Time-temperature histories of the flame:

Time-temperature histories of the fires for each of the four configurations and each wind speed were obtained by allowing the fire to burn past a stationary vertical array of thermocouples. In the case of the ceiling extended configurations, the ceiling was moved manually to follow the fire.

The array consisted of 5 thermocouples spaced uniformly upwards at intervals of 127 mm with the first thermocouple placed on the fuel surface (Figure 4). The array was located 2 m downstream of the entrance to the combustion test section at the trailing edge of the second window. Each thermocouple was hung on a vertical 12 mm diameter mild steel rod and projected horizontally outwards 150 mm from the rod to the center of the tunnel. The rod was bent 90° above the highest thermocouple and extended through the side wall to a fixed outside support. Exposed-bead, Inconel clad, type-K (chromel-alumel) thermocouples made from 125 µm diameter wires were used. The time constants of these thermocouples were too large (approximately 150 ms) to gauge true flame temperatures, but they gave representative measures of flame position. No melting of the thermocouples was experienced because of averaging effects as the temperature fluctuated between ambient and flame in the turbulent flow.

To conduct a test run, the thermocouple array was lifted off the fuel surface and the conveyor speed was increased to move the fire downstream of the array (to a position approximately 3.5 m downstream of the entrance to the combustion test section of the tunnel). The conveyor drive motor was stopped, the array positioned, and the fire allowed to spread upstream. At the same time, the data acquisition system was started to record temperatures on all five thermocouples. Thermocouples were sampled at 30 Hz using the same data acquisition system described for the anemometer. The run was stopped when the fire had passed the array or when it had come to within 0.5 m of the flexible conveyor. Temperature data were later compiled into contour and surface plots displaying approximate flame shape. No corrections were made for radiation or conduction.

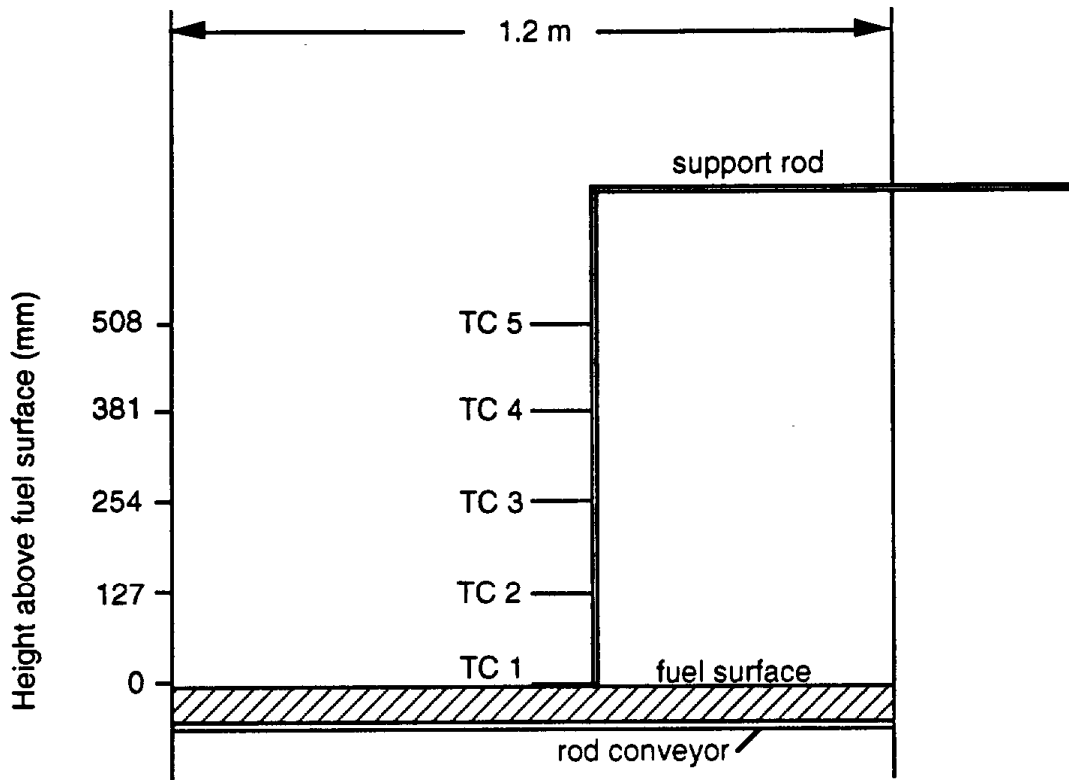


Figure 4. View across wind tunnel showing location of thermocouples in array.

#### Local flame temperatures:

A fast response, type-R (Pt/Pt+13% Rh) thermocouple was used to measure local flame temperatures. This thermocouple was of the exposed-bead type, constructed of 25  $\mu\text{m}$  diameter wires, with a bead diameter of approximately 40  $\mu\text{m}$  and an estimated time constant of 5 ms. The wire was strung through 5 mm diameter ceramic insulating beads which in turn were inserted through a 6 mm diameter stainless steel tube for support. The wire and bead extended approximately 20 mm from the end of the ceramic insulator. The assembly was inserted through the side wall of the tunnel into the flame to a depth of 0.4 m from the wall and fixed in position while the temperature was monitored. Vertical traverses 2 m downstream from the entrance to the combustion test section were completed by

moving the fire into position with the conveyor, and keeping it in position by adjusting conveyor speed as needed. The probe height was adjusted manually. The flame temperature was probed from the flame tip downwards to the fuel surface through the flame center, and behind the flame over a region of glowing combustion in the char bed.

At each position, the probe was sampled for six seconds at 1 kHz using the same data acquisition system described above for the anemometer. Relative frequency densities were computed from each data file using a 50 K interval width. No radiation or conduction corrections were applied to the temperature measurements. Difficulties with using thermocouples in sooting flames are well known, and the results are qualitative in nature. They do serve for purposes of comparing the relative differences among the temperature fields of the various configurations. The error due to radiation is estimated to be in the range of 20 to 100 K at a thermocouple temperature of 1670 K (about the highest measured) and a wall temperature of 300 K with an assumed Nusselt number,  $Nu = 2$ , and emittance varying from 0.2 to 0.95 (16,17). Actual instantaneous peak flame temperatures are higher than reported due to heat losses and to the finite response time of the probe which was subject to rapid fluctuations in temperature as the flame moved in the turbulent flow.

#### Flame radiation:

Flame radiation was measured from a position above and in front of the flame as shown in Figure 5. A water-cooled, gas purged Schmidt-Boelter type sensor (Medtherm model 64-01-22, Huntsville, AL) was used. The sensor and pre-amplifier were installed in a water cooled aluminum case fixed on the end of a 25 mm steel square tube inserted through the side wall of the tunnel. The transducer view angle was  $150^\circ$ , centered on the fuel surface 2 m downstream from the entrance to the combustion test section. The view angle was large enough to see the entire flame up to positions directly beneath the sensor, although the fire was never run this far forward when measuring flame radiation. With the ceiling retracted, the sensor view included about  $55 \text{ m}^2$  of wind tunnel wall area.

The pre-amplifier output was connected to a signal conditioner which boosted the voltage signal to an acceptable range for the data acquisition system described previously. The radiation sensor was read simultaneously with the type-R thermocouple, and at the same sampling rate of 1 kHz. This rate was well in excess of that required for this transducer,

which had a time constant of approximately 1.5 s. The distance of the flame from the sensor varied as the sampling position for the type-R thermocouple was changed.

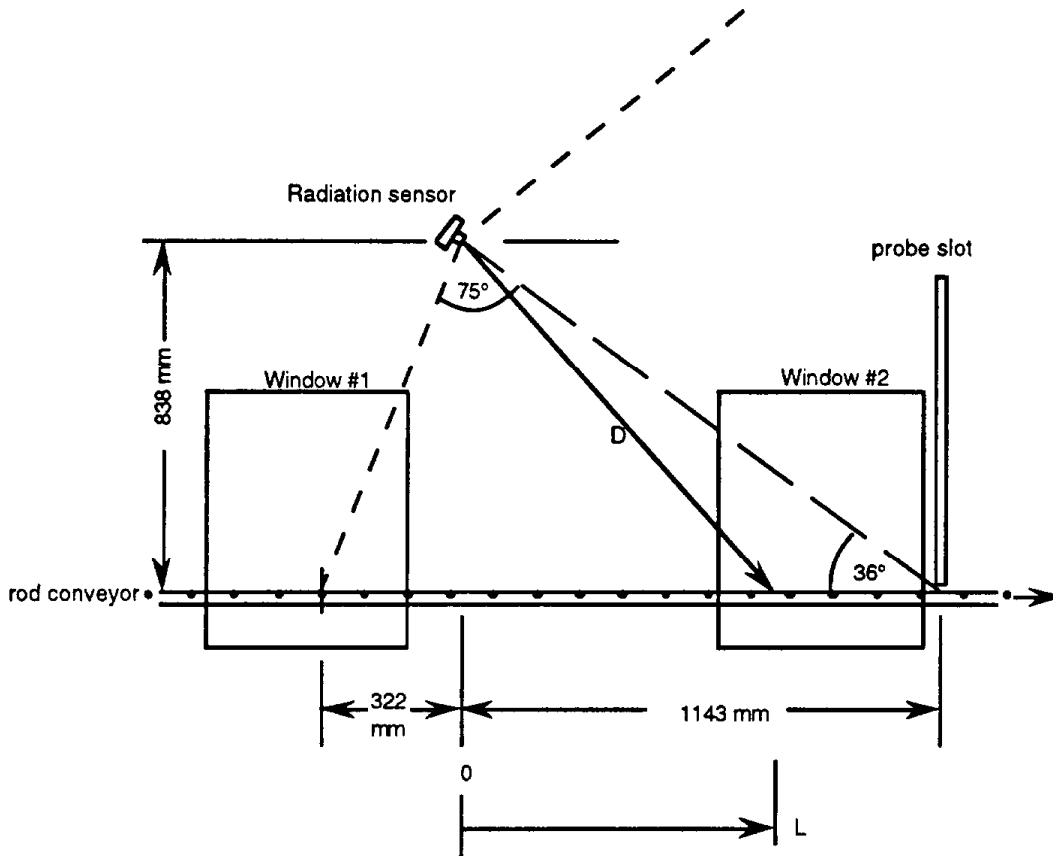


Figure 5. Location of radiation sensor.

The longitudinal separation of the leading edge of the fire from the sensor position was recorded at each sample. The separation,  $D$ , from the sensor to the leading edge of the fire was then computed. Estimated total flame radiation and fraction of total heat release were computed by integrating across the area above the fuel surface at radius  $D$ . An estimate of the background radiation due to heating of the tunnel walls and surfaces was made by rapidly extinguishing the fire while recording sensor output. This background normally amounted to about  $200 \text{ W m}^{-2}$ .

### Local gas concentrations:

Local gas samples were collected from the flame region using a 9.5 mm outside diameter, L-shaped, stainless steel water-cooled probe. The probe was inserted through a slot to a depth of 0.4 m from the tunnel side wall, 2 m downstream from the test section entrance (Figure 5). The final 75 mm of the probe were bent 90° to the rest of the probe so that the probe tip faced upstream during sampling. At the fuel surface, the probe tip was rotated downwards to probe within the fuel bed. The height of the probe was adjusted manually and fixed in position during sampling. The conveyor speed was adjusted as needed to keep the fire in position during the sampling period.

The gas sample was drawn through a 1.5 mm diameter stainless steel tube running inside the water-cooled probe. Initially, a static pressure tap located just inside the probe nozzle was to be used to adjust the flow for isokinetic conditions. Plugging from tar condensing at this tap when sampling near the fuel surface caused this method to be abandoned in favor of a mass flow transducer at the outlet of the sample line. The mass flow sensor was used to set sample flow rate from velocity measurements obtained with the anemometer near the sampling location. When sampling within the fuel bed, plugging of the gas sample line also occurred frequently.

The outlet of the gas sampling line was connected through a teflon line and glass fiber filter to a teflon lined sample pump, impinger, and 2 mL glass sample collector. Actual sample locations are shown in the results section. Background samples were collected upstream of the fire. The sample line was purged for 3 minutes at each location before taking the sample. Typical flow rates ranged from 0.1 to 0.25 L min<sup>-1</sup> depending on height. Samples were analyzed within one day by gas chromatography for permanent gases and light hydrocarbons. All gases were analyzed using a Hewlett-Packard 5730A gas chromatograph. Oxygen, nitrogen, and carbon monoxide were analyzed using a thermal conductivity detector (TCD) and separated on a 1.8 m x 3 mm molecular sieve 5A column with an injector temperature of 150°C, detector temperature of 200°C, and oven temperature of 80°C. Helium was used as carrier gas. Carbon dioxide was analyzed on the TCD following separation on a 1.8 m x 3 mm Porapak Q column at an oven temperature of 45°C using helium carrier. Hydrogen was analyzed on the mol sieve column with nitrogen carrier. Hydrocarbons including methane, ethane, ethylene, and acetylene were analyzed by flame ionization detector (FID) following separation on a 1.8 m x 3 mm Porapak N

column with nitrogen carrier and 50°C oven temperature. Calibration was performed after every ten sample injections.

#### Soot volume:

Line-of-sight average soot volume fractions were computed from measurements of laser light extinction through the flame. An argon ion laser (488 nm wavelength, 50 mW maximum output power CW, Omnicrome model 532, Chino, CA) was used in conjunction with a photodiode (Silicon Detector Corp. model SD444-42-12-261, Camarillo, CA) to monitor laser light intensity on the opposite side of the tunnel. An interference filter (OFR model FL-488.0, Caldwell NJ) and neutral density filter (OFR model FD-1.0) were placed ahead of the photodiode to restrict wavelength and attenuate intensity. All optical elements were protected from ambient light. The laser and photodiode were located on an external U-shaped mounting platform extending around the walls and under the floor of the tunnel. The laser and photodiode were moved vertically together by lifting the open end of the platform on a roller carriage. A low-pass filter was used on the photodiode output to provide a longer time constant (on the order of 1 - 2 s) to obtain better averages of light extinction. The output signal was acquired on the same data acquisition system described above. Full details of this analysis are included in (18).

The light beam was passed through a vertical series of 16 mm diameter holes in the wind tunnel wall. All holes not in use were kept covered. Sampling heights were 76, 127, 178, 229, 330, 432, 533, and 686 mm above the rod conveyor. Scans were conducted by holding the conveyor stationary and allowing the fire to burn past the laser in the same manner used for obtaining the time-temperature histories with the type-K thermocouple array. This technique proved more consistent than attempting to hold the fire stationary at each sampling location. Samples were acquired at 1 Hz, with a total scan duration of approximately 240 seconds at each height. Ambient background radiation was removed by referencing all intensities to the upstream intensity ahead of the flame. An estimate of the error from flame (non-laser) radiation was made by allowing the fire to spread past the photodiode without the laser operating. A maximum diode response of approximately 10 mV was observed, giving errors of 1 to 2% for typical voltage drops of 0.5 to 1 V due to flame attenuation of laser light.

Average soot volume fraction across the tunnel width was computed using a Rayleigh formulation,

$$k_{\text{ext}} = \frac{1}{L} \ln \left( \frac{I_0}{I} \right) \quad [12]$$

$$k_{\text{ext}} = \frac{\lambda^2}{\pi} \text{Im} \left( \frac{m^2 - 1}{m^2 + 2} \right) N \alpha^3 \quad [13]$$

$$\alpha = \frac{\pi D}{\lambda} \quad [14]$$

and,

$$\phi = N \frac{\pi}{6} D^3 \quad [15]$$

where

- $k_{\text{ext}}$  = extinction coefficient,
- $L$  = path length (in this case, the width of the tunnel)
- $I$  = attenuated light intensity at photodiode
- $I_0$  = unattenuated light intensity at photodiode
- $\text{Im}$  = imaginary part
- $\lambda$  = wavelength of incident light (m)
- $m$  = refractive index of particles =  $1.57 - 0.56i$
- $i = (-1)^{1/2}$
- $N$  = particle concentration ( $\text{m}^{-3}$ )
- $D$  = particle diameter, assumed uniform (m)
- $\phi$  = soot volume fraction (-)

The refractive index used was that of Dalzell and Sarofim (19). Under these assumptions, the soot volume fraction was computed from the diode intensity as:

$$\phi = 8.18 \times 10^{-8} \ln \left( \frac{I_0}{I} \right) \quad [15a]$$

To examine the assumption that light attenuation was due principally to soot absorption, a series of particulate samples was collected from the flame and post-flame regions using a point-to-plane electrostatic precipitator. These samples were examined by transmission electron microscopy (TEM). Large numbers of soot particles in the size range of 10 - 30 nm were found in the flame regions (Figure 6). Ash particles were present in the post-flame region, but soot still appeared to be the predominant form. The soot volume is, at any rate, relatively insensitive to the value of  $m$  for fairly large changes in its magnitude. No calibrations were attempted, nor was multiple scattering considered to be significant in comparison to the attenuation from soot absorption ( $0.5 \leq I/I_0 \leq 0.8$ ).

#### Operating conditions:

Inlet air temperature was monitored by a thermistor located between the flow straightening screens in the inlet section, and later by a type T thermocouple placed near the inlet of the combustion test section. Inlet relative humidity was monitored near the screens by a polymeric humidity transducer (Phys-Chem Scientific model PCRC-11, New York, NY). These sensors were connected to a separate electronic datalogger (Campbell Scientific model CR21X, Logan Utah) with digital values stored on a microcomputer. Also connected to the datalogger were the stack and impinger thermocouples, the stack anemometer, and a sensor for measuring conveyor speed. The conveyor speed was measured by counting switch closures on a switch operated by an eight lobe cam fixed on the end of the drive motor gear head shaft. Conveyor travel (total displacement) was obtained by integrating conveyor speed over time. Instantaneous fuel consumption rate was obtained from the conveyor speed and the predetermined loading rate. Total fuel consumption was determined directly from loaded fuel weight and from total conveyor travel. All sensors were scanned at 1 minute intervals, with the exception of the stack anemometer (scanned at 1 Hz and averaged over 1 minute), and the conveyor speed, which was monitored continuously. Average stack gas velocity was computed across the twelve traverse positions.

Fuel was manually loaded and spread at a constant  $680 \text{ g m}^{-2}$  wet basis. For these tests, fuel moisture content was similar (overall range of 6.4 to 10.1% wet basis), and the dry weight loading rate was therefore similar. Fuel samples were collected every two hours and bagged in plastic. These samples were later tested for moisture by oven drying. A single source of fuel was used for all tests, and was supplied in multiple bales weighing

300 to 400 kg each. The fuel was rice straw, including both lower and upper plant parts (stubble and straw), and was obtained by swathing (cutting close to ground level) and baling a harvested field.

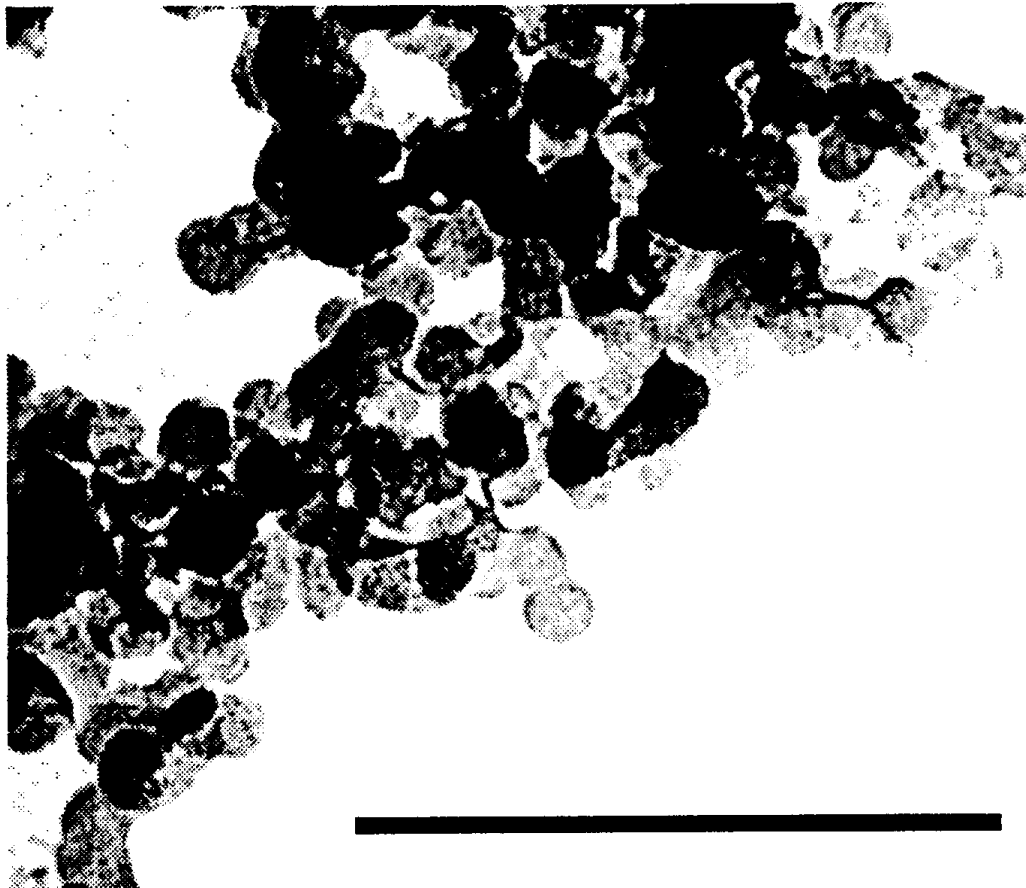


Figure 6. Transmission electron micrograph of soot particles collected from the flame region, 63 mm above the fuel surface, on a point-to-plane electrostatic precipitator. The length of the reference bar represents 250 nm.

Each test was started by loading the conveyor along its full length and about 3 m into the combustion test section, igniting the fuel across the width of the tunnel with a hand-held propane burner, and allowing the tunnel to stabilize over 10 to 15 minutes. A fine stainless steel wire mesh was interwoven among the stainless steel rods, which, in the case

of the configurations with no floor installed, prevented fines from falling through to the refractory floor and causing ignition of the incoming fuel ahead of the fire front. The region between the rod conveyor and the refractory brick was baffled by placing transverse steel sheets vertically up to the bottom of the rod conveyor along the tunnel floor at 1 m intervals (Figure 2). The baffling was intended to be representative of the stubble layer in a field burn.

Ash was collected throughout each experiment and weighed. Fuel rate, stack gas velocity, and ash rate were used to determine the inlet air mass flow rate and average velocity by mass balance. The inlet velocities from the x-probe anemometer were qualitatively in good agreement with those determined by mass balance, although total flow rates could not be determined from the anemometer results.

## Results

Average results for each of the eight cases (four configurations with two wind speeds) are listed in Table 1. Results for individual experiments are included in the appendix. The low wind speed setting was in the range of 2.1 - 2.2 m s<sup>-1</sup>. The high speed setting was 3.1 - 3.2 m s<sup>-1</sup>. Average fuel moisture varied between 7.8 and 9.3% wet basis. The residual ash fraction was typically 20% of fuel dry weight, and overall air-fuel ratios ranged from about 550 to 900. The fire spreading velocities were 0.5 - 0.6 m min<sup>-1</sup> (8-10 mm s<sup>-1</sup>) except for the CRNF high wind speed configuration for which the mean spreading velocity was significantly different at about 0.7 m min<sup>-1</sup> (range of 0.58 to 0.82 m min<sup>-1</sup>). Faster spreading rates were obtained during three consecutive experiments in the CRNF high wind speed configuration. These all used fuel from a single bale of straw and were conducted under higher ambient air temperatures than most other tests. Spreading rate was not well correlated with air temperature, although a trend towards increased spreading rate with increased temperature was observed. Spreading rates were also observed to change occasionally as one bale was exhausted and a new bale started. These differences are thought to be related to the bulk density of straw as loaded on the conveyor (with constant loading rate), as well as to differences in properties of the straw. Further studies are needed to investigate these influences.

Average emission factors for PM varied from 0.5 to 0.7% of fuel mass (global mean = 0.635%, standard deviation = 0.097%). There were significant differences in the emission

factors among the various configurations, however. The incidence table for a three-way analysis of variance (ANOVA) is given in Table 2.

The floor (probability  $p = 0.0003$ ) and wind speed ( $p = 0.0005$ ) had the largest effect on PM emission factor, while the ceiling position had little effect by itself ( $p = 0.8015$ ). The extremes in the average PM emission factor were 0.505% for the CEWF high wind speed configuration, and 0.727% for the CRNF low wind speed configuration. Most of the following discussion is therefore focused on these two cases, the other cases being intermediate in effect. Full results for all cases are included in the appendix.

Table 1. Means of operating results for four configurations and two wind speeds.

	CRNF Low Wind Speed	CRNF High Wind Speed	CENF Low Wind Speed	CENF High Wind Speed	CEWF Low Wind Speed	CEWF High Wind Speed	CRWF Low Wind Speed	CRWF High Wind Speed
Mean Inlet Air Velocity (m/s)	2.20	3.17	2.11	3.18	2.18	3.13	2.10	3.21
Fuel Moisture Content (% wet basis)	8.62	8.28	8.31	7.83	8.15	9.33	8.42	9.13
Fire spreading velocity (m/minute)	0.53	0.69	0.52	0.60	0.52	0.47	0.51	0.50
Ash Fraction (g/g)	0.19	0.19	0.21	0.21	0.19	0.20	0.19	0.18
Overall Air-Fuel Ratio (g/g)	565.68	636.36	541.98	718.02	559.21	917.73	560.15	907.51
PM Concentration (mg/m <sup>3</sup> )	15.84	10.57	15.12	10.88	14.33	6.74	12.33	7.98
PM Emission Factor (%)	0.727	0.560	0.681	0.645	0.636	0.505	0.562	0.597

Table 2. Three-way incidence table on PM emission factor (% , number of experiments shown in parentheses).

Floor Configuration		No Floor		With Floor		Totals
		< 3 m/s	> 3 m/s	< 3 m/s	> 3 m/s	
Ceiling	Retracted	(13) 0.727	(6) 0.560	(9) 0.562	(4) 0.597	(32) 0.633
	Extended	(11) 0.681	(6) 0.645	(11) 0.636	(4) 0.505	(32) 0.637
Totals		(24) 0.706	(12) 0.602	(20) 0.603	(8) 0.551	(64) 0.635

### Inlet Velocity Profiles and Turbulence Characteristics:

Inlet streamwise and vertical velocity profiles and turbulence intensities for both wind speeds are shown in Figures 7a-p for the CEWF configuration, and Figures 8a-p for the CRNF configuration. The floor had little effect on the velocity profiles, and results for comparable wind speeds and ceiling positions in the other two configurations are similar. For convenience, a test in which no fire was present in the tunnel is referred to as cold flow, and for a fire present in the tunnel, hot flow (the terms are based on stack conditions). Apparent in the profiles shown below is the limited traverse depth possible in the hot flow conditions at the downstream position. Nor could the flow be probed close to the fuel surface because of fuel elements which extended above the mean fuel surface. Turbulence measurements with x-probe hot-film anemometers are well known to be unreliable very near rough surfaces at any rate (20); turbulence characteristics reported at lower heights are somewhat qualitative in nature.

### Ceiling Extended Configuration

The high speed CEWF streamwise velocities for the upstream and downstream positions are shown in Figures 7a and 7e, respectively. Maximum freestream velocities were  $3.5 \text{ m s}^{-1}$  in cold flow and  $3.9 \text{ m s}^{-1}$  in hot flow. The maximum velocities at the upstream and downstream positions were essentially the same. Boundary layers over the fuel surface as well as below the ceiling were evident. The traverse integrated velocities were higher in hot flow than in cold flow (Table 3).

The respective vertical velocities appear in Figures 7b and 7f. The vertical velocity in the upstream position started near zero just above the fuel surface and increased to about  $0.09 \text{ m s}^{-1}$  at 110 cm above the rod conveyor and then jumped to about  $0.2 \text{ m s}^{-1}$  at the highest sampling point due to leakage through the probe access hole in the ceiling. The downstream vertical velocities also started near zero at the fuel surface but increased to between  $0.2$  and  $0.3 \text{ m s}^{-1}$ . Vertical velocities in hot flow were slower than in cold flow at both positions, whereas the opposite was observed with the streamwise velocities.

Plots of local turbulence intensities for the high wind speed runs, including upstream streamwise, upstream vertical, downstream streamwise, and downstream vertical turbulence intensities are shown in Figures 7c, 7d, 7g, and 7h respectively. Freestream local turbulence intensities were 2% in the streamwise direction and 1% in the vertical

direction. Within the lower boundary layer (which was approximately 60 cm thick) the turbulence intensities increased to maximum values of 25% to 35% in the streamwise direction and 10% to 12% in the vertical direction as the surface was approached. Hot flow turbulence intensities in the boundary layer were slightly higher than those of cold flow. The upstream and downstream comparisons were remarkably similar. They also compared very well with the CENF configuration. Ratios of the vertical turbulence intensities to the streamwise turbulence intensities are 0.35 to 0.40. This is consistent with other wind tunnel and atmospheric data (20 - 24).

Profiles of the streamwise velocities for the low wind speed are given in Figure 7i for the upstream position and in Figure 7m for the downstream position. The maximum cold flow velocities were between 1.9 and 2.1 m s<sup>-1</sup>. The hot flows reached about 2.2 m s<sup>-1</sup>. The upstream and downstream vertical velocities are shown in Figures 7j and 7n, respectively. The vertical velocity in the upstream position again started near zero at the fuel surface and increased to about 0.07 m s<sup>-1</sup> at 110 cm and then increased to about 0.2 m s<sup>-1</sup> at the highest sampling point near the probe access hole in the ceiling. In the downstream case, the cold flow vertical velocity started at zero near the fuel surface and increased uniformly with height to 0.2 m s<sup>-1</sup>. These two profiles are very similar to the respective CEWF high speed cases in Figures 7b and 7f.

The streamwise and vertical turbulence intensities at the upstream position are shown in Figures 7k and 7l, respectively. The corresponding profiles for the downstream position appear in Figures 7o and 7p. The hot and cold flow freestream turbulence intensities in the streamwise direction were 3-4% for both the upstream and downstream positions. The freestream vertical turbulence intensities were 1-2%. The intensities increased to values of 40-50% in the streamwise direction and 10-20% in the vertical direction as the fuel surface was approached. In the upstream case, the hot flow turbulence intensities were higher in the boundary layer. The traverse depth in the downstream position was not sufficient to observe any differences between the hot and cold flow conditions.

#### Ceiling Retracted Configuration

The streamwise velocity profiles for the CRNF high wind speed, upstream and downstream positions appear in Figures 8a and 8e, respectively. Maximum velocities were 3.2 to 3.3 m s<sup>-1</sup> in cold flow and 3.5 to 3.6 m s<sup>-1</sup> in hot flow. The hot flow condition at the upstream position exhibited a thicker boundary layer and a faster freestream velocity

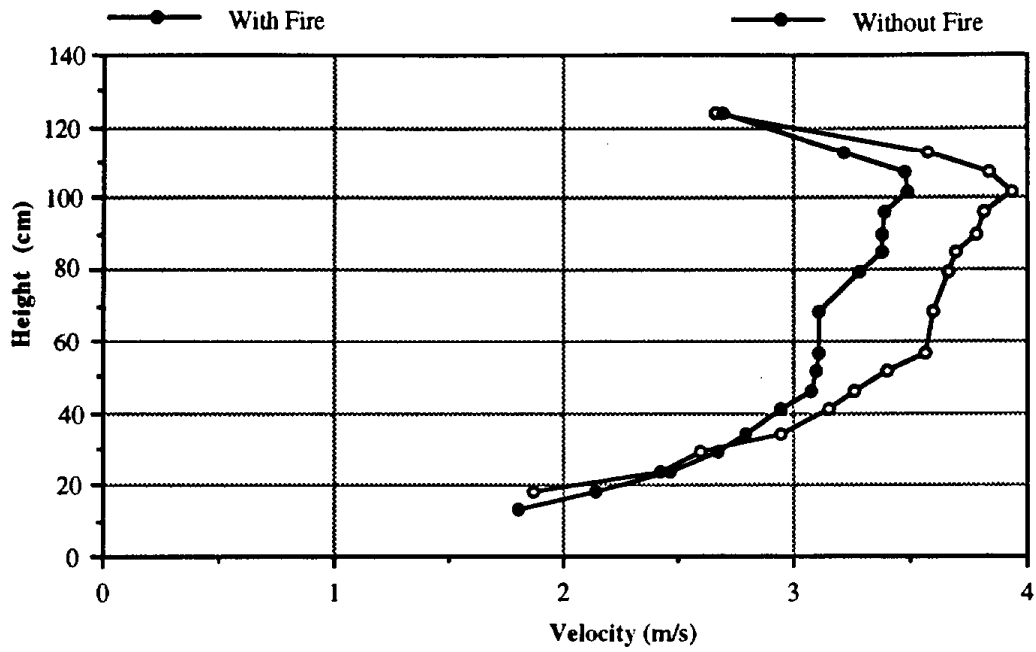


Figure 7a. Streamwise velocity, CEWF, high wind speed, upstream position.

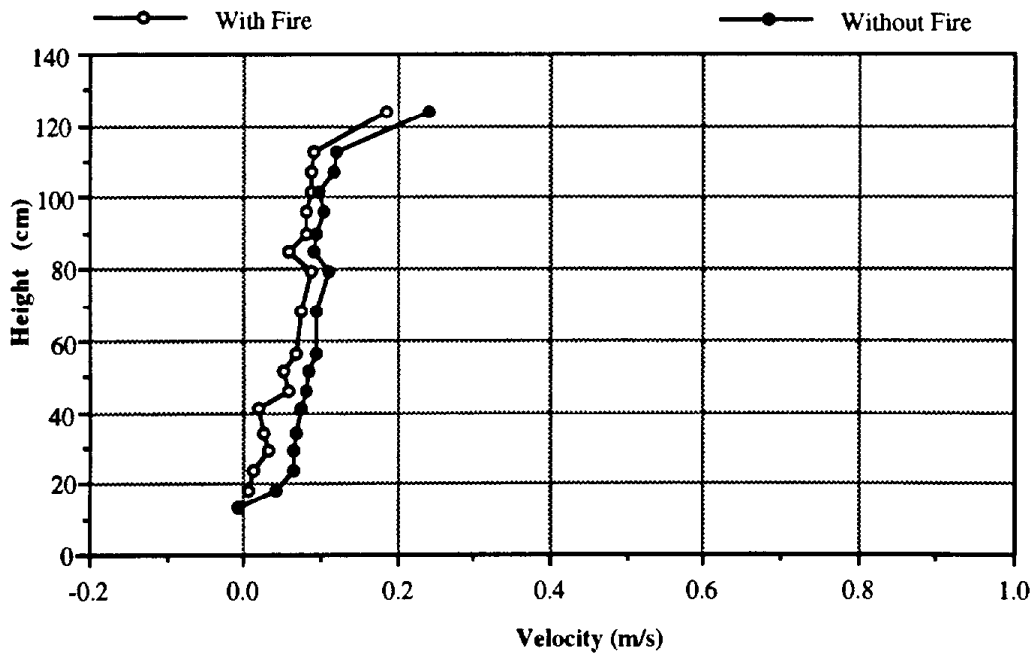


Figure 7b. Vertical velocity, CEWF, high wind speed, upstream position.

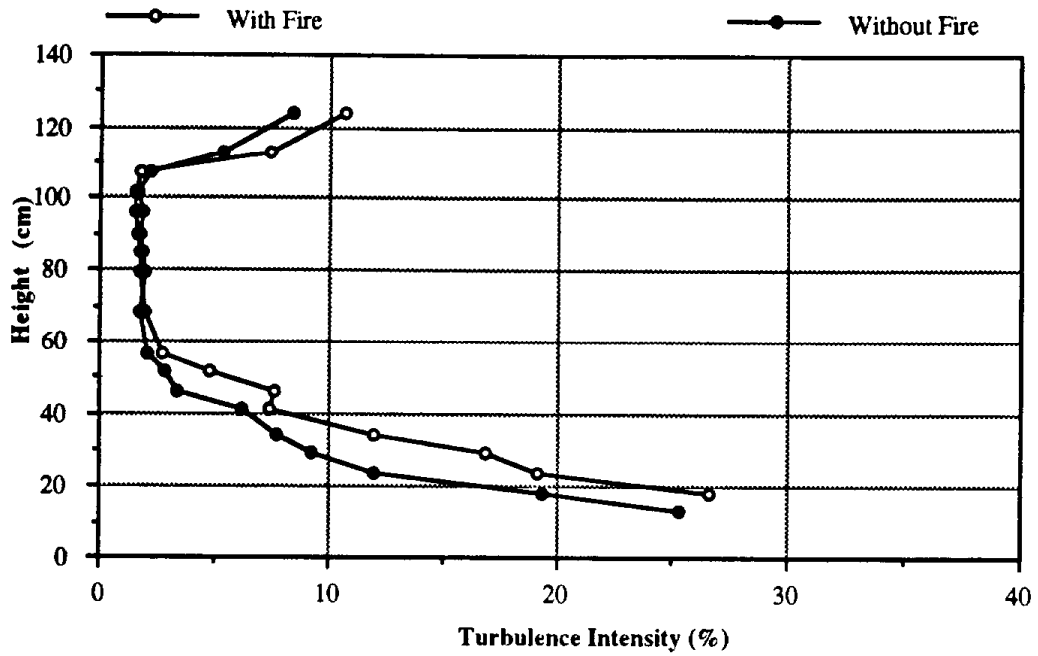


Figure 7c. Streamwise turbulence intensity, CEWF, high wind speed, upstream position.

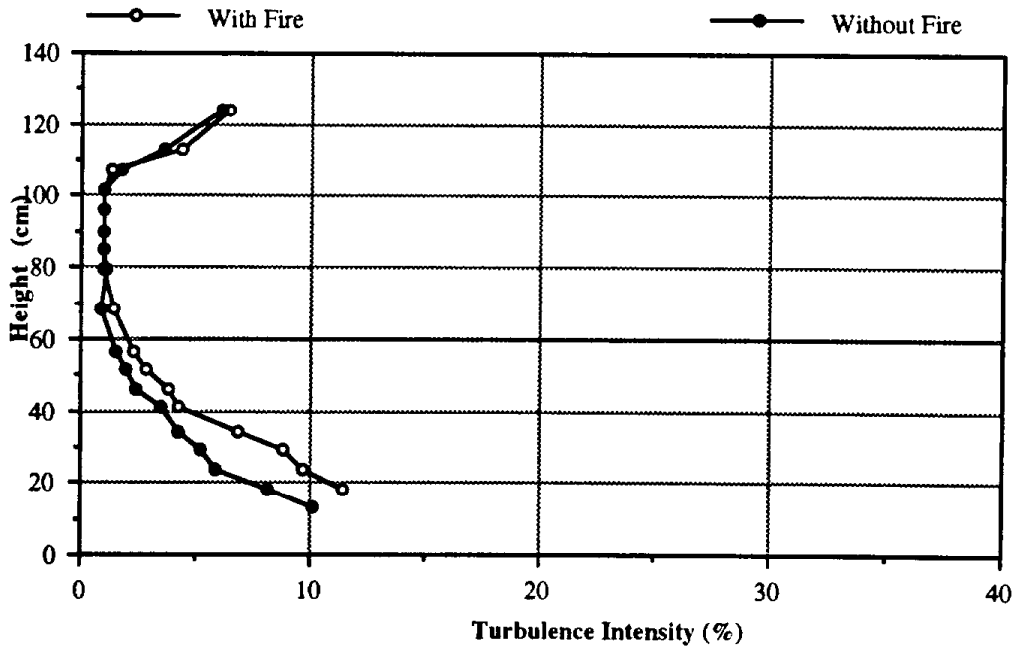


Figure 7d. Vertical turbulence intensity, CEWF, high wind speed, upstream position.

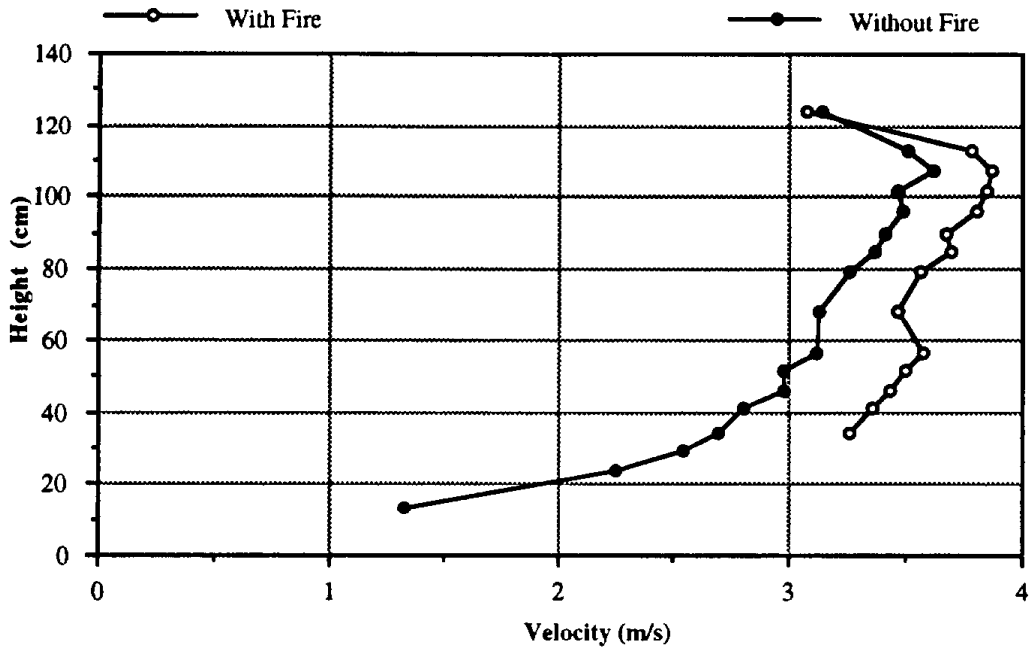


Figure 7e. Streamwise velocity, CEWF, high wind speed, downstream position.

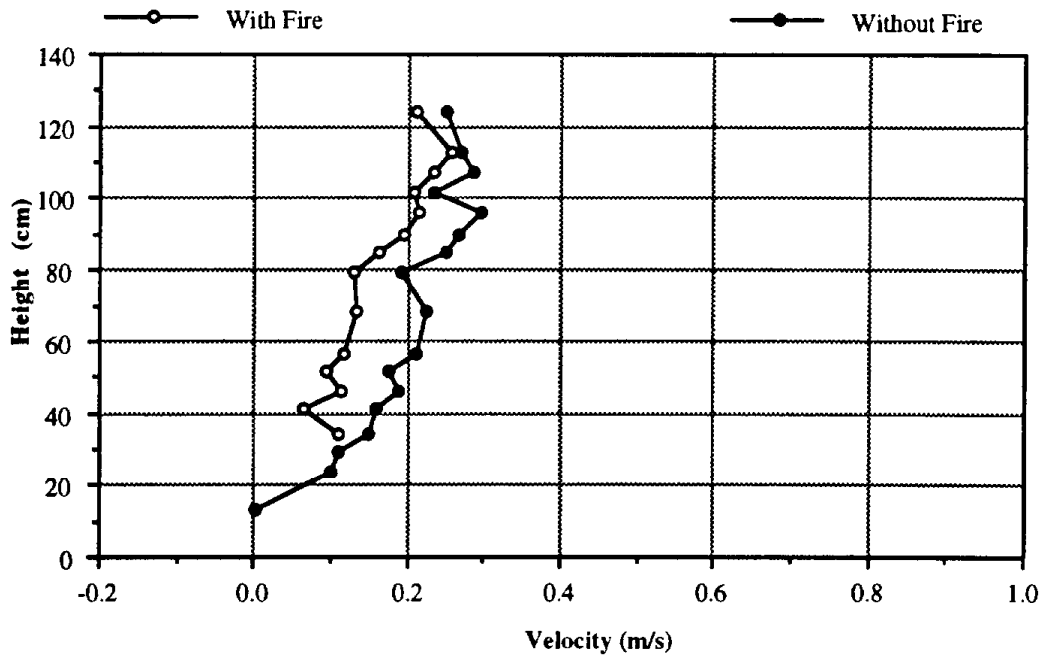


Figure 7f. Vertical velocity, CEWF, high wind speed, downstream position.

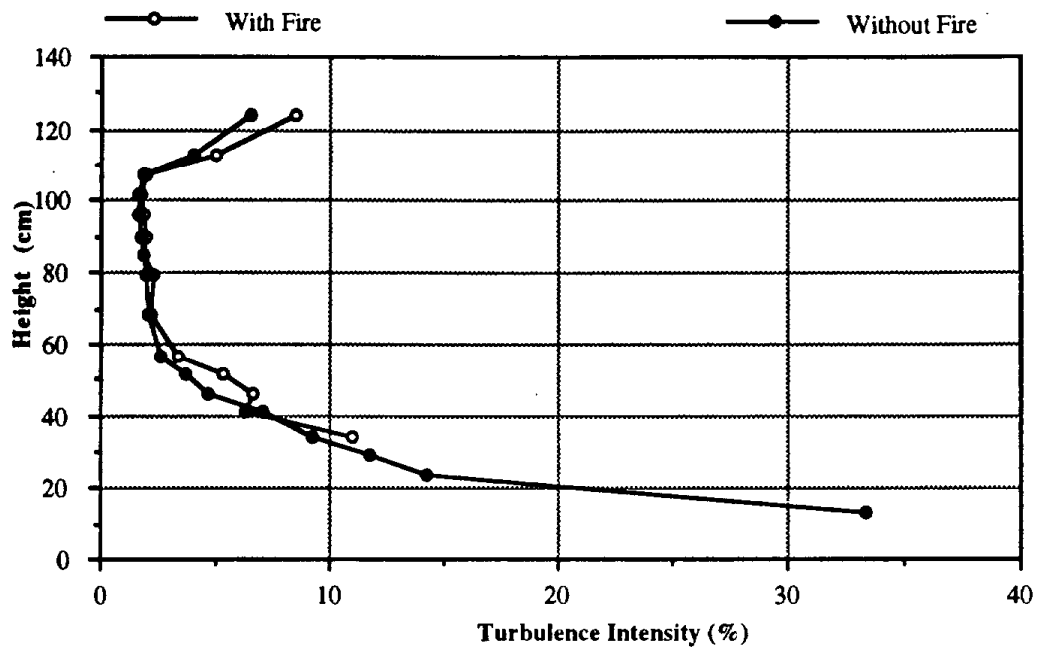


Figure 7g. Streamwise turbulence intensity, CEWF, high wind speed, downstream position.

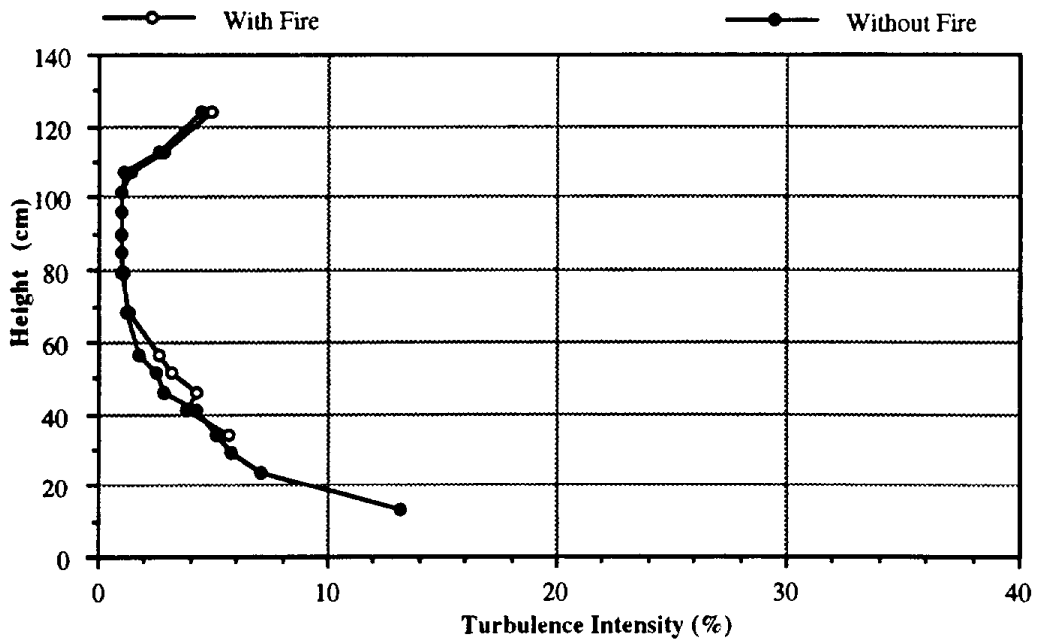


Figure 7h. Vertical turbulence intensity, CEWF, high wind speed, downstream position.

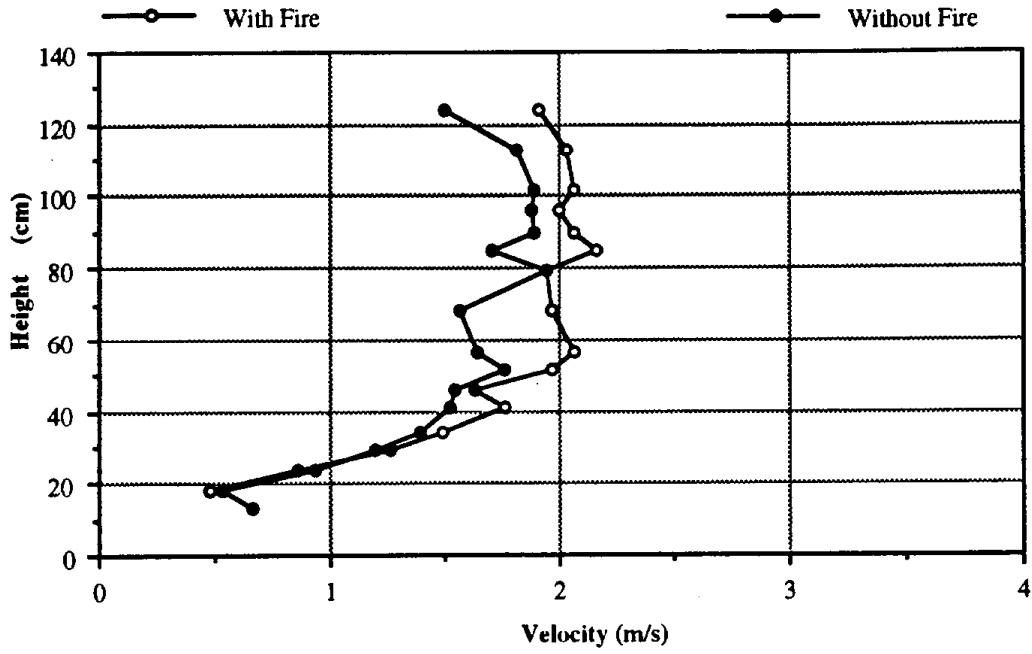


Figure 7i. Streamwise velocity, CEWF, low wind speed, upstream position.

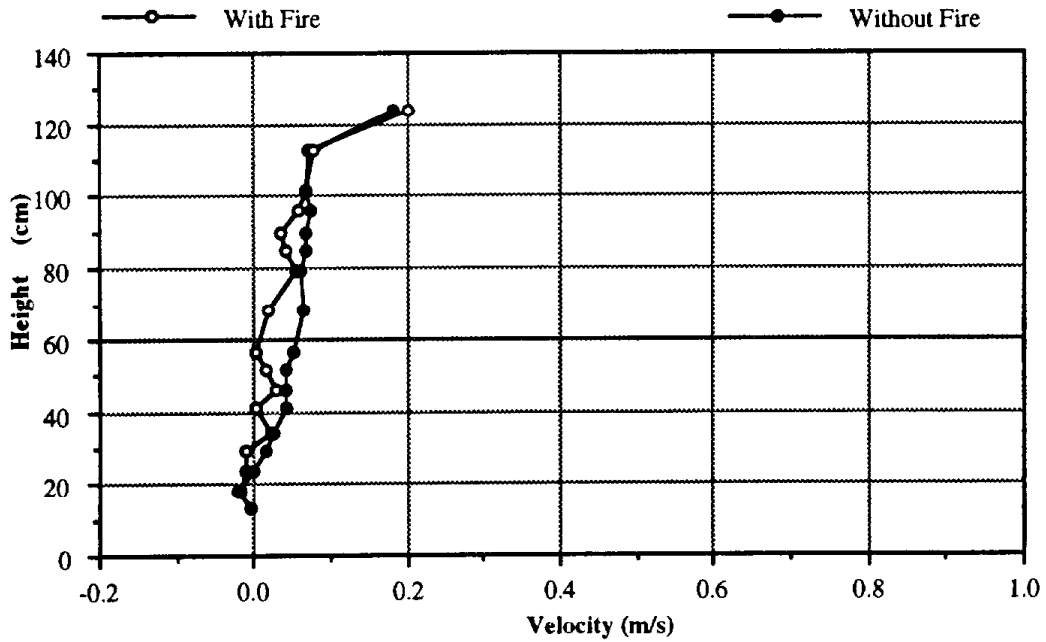


Figure 7j. Vertical velocity, CEWF, low wind speed, upstream position.

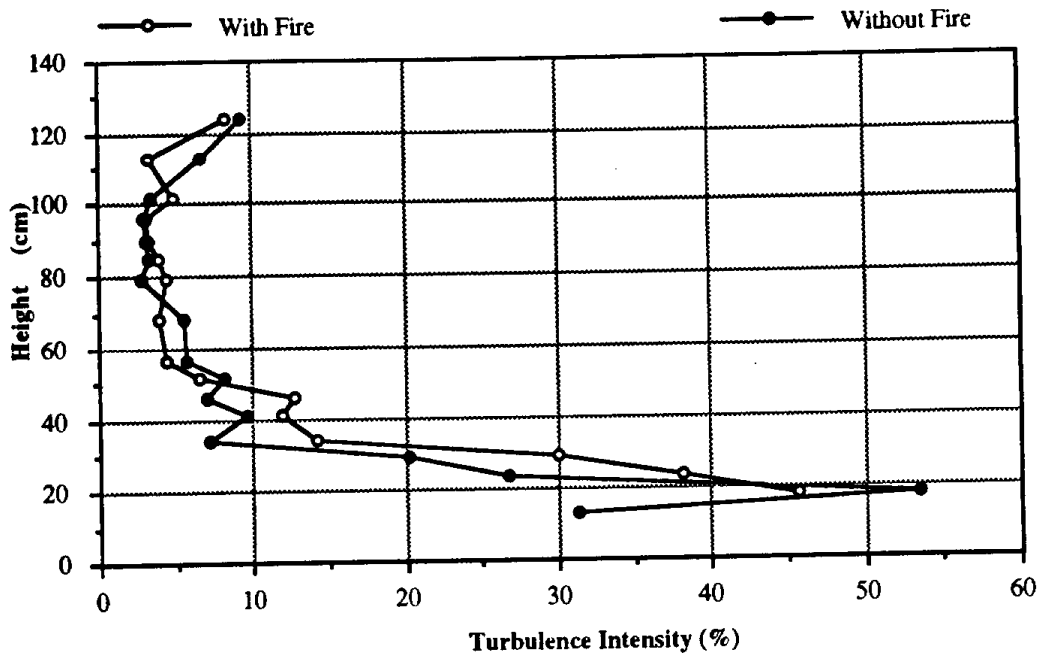


Figure 7k. Streamwise turbulence intensity, CEWF, low wind speed, upstream position.

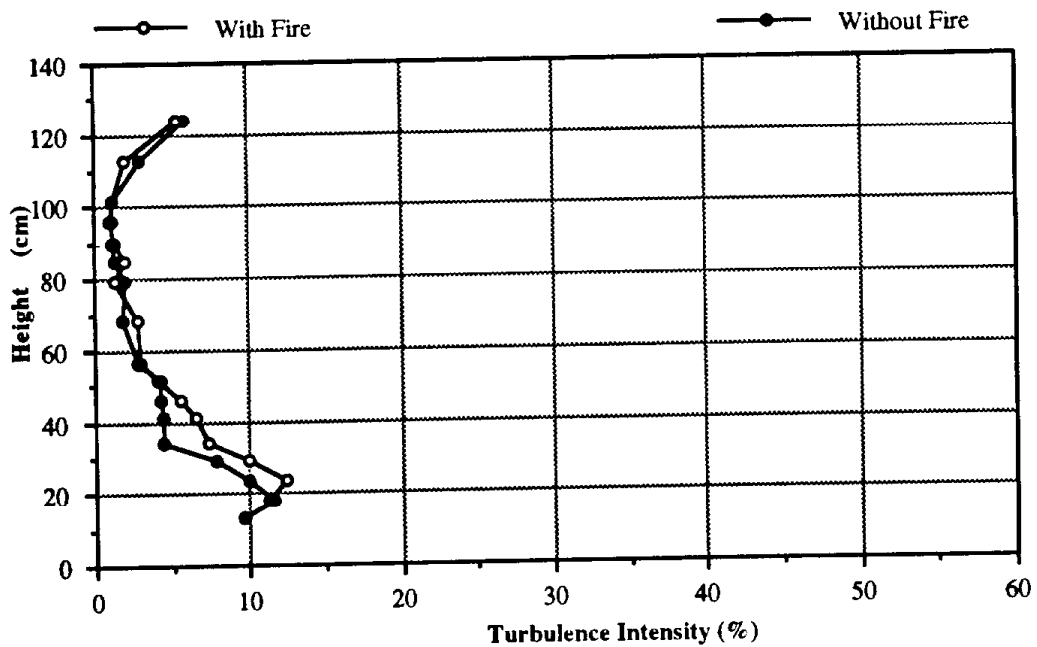


Figure 7l. Vertical turbulence intensity, CEWF, low wind speed, upstream position.

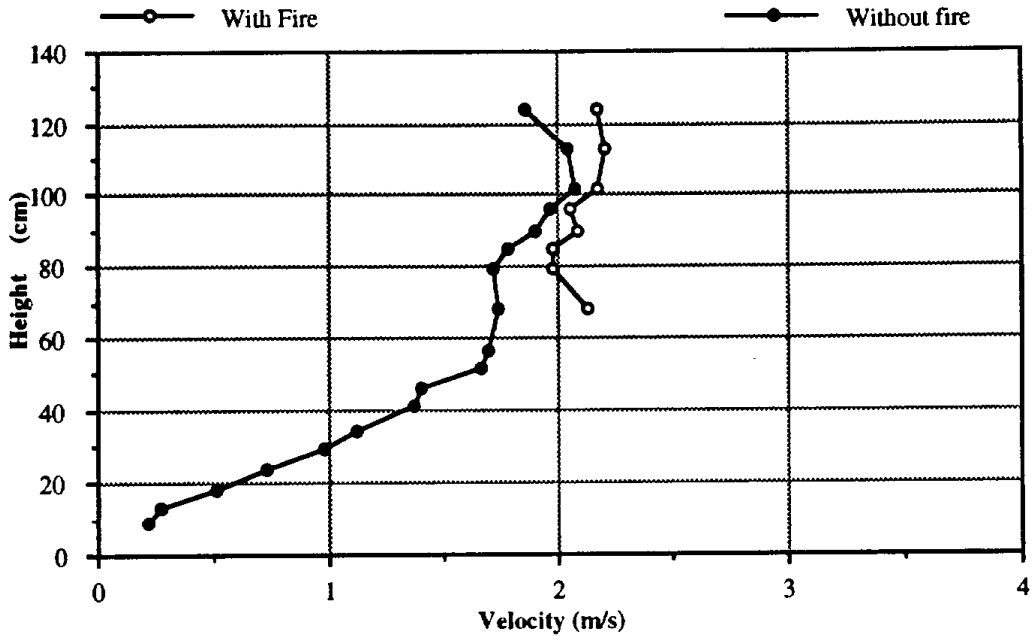


Figure 7m. Streamwise velocity, CEWF, low wind speed, downstream position.

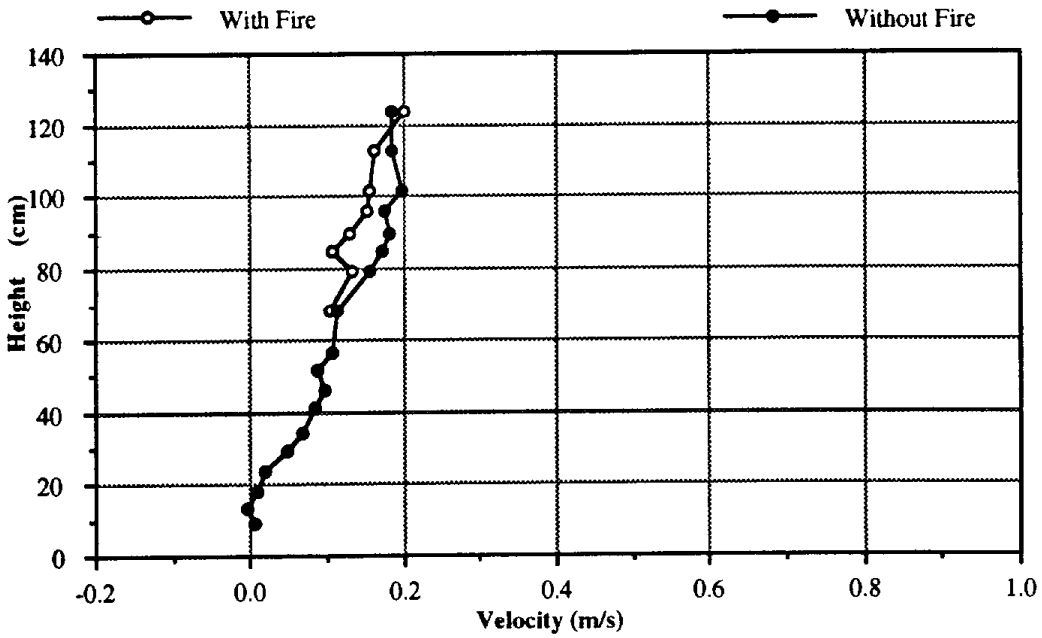


Figure 7n. Vertical velocity, CEWF, low wind speed, downstream position.

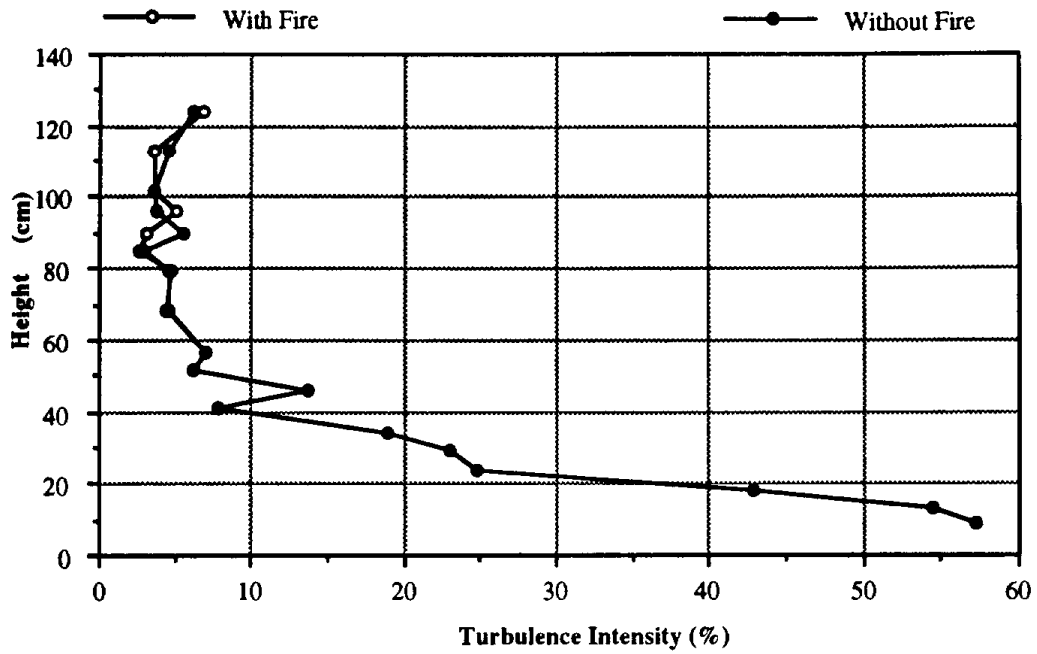


Figure 7o. Streamwise turbulence intensity, CEWF, low wind speed, downstream position.

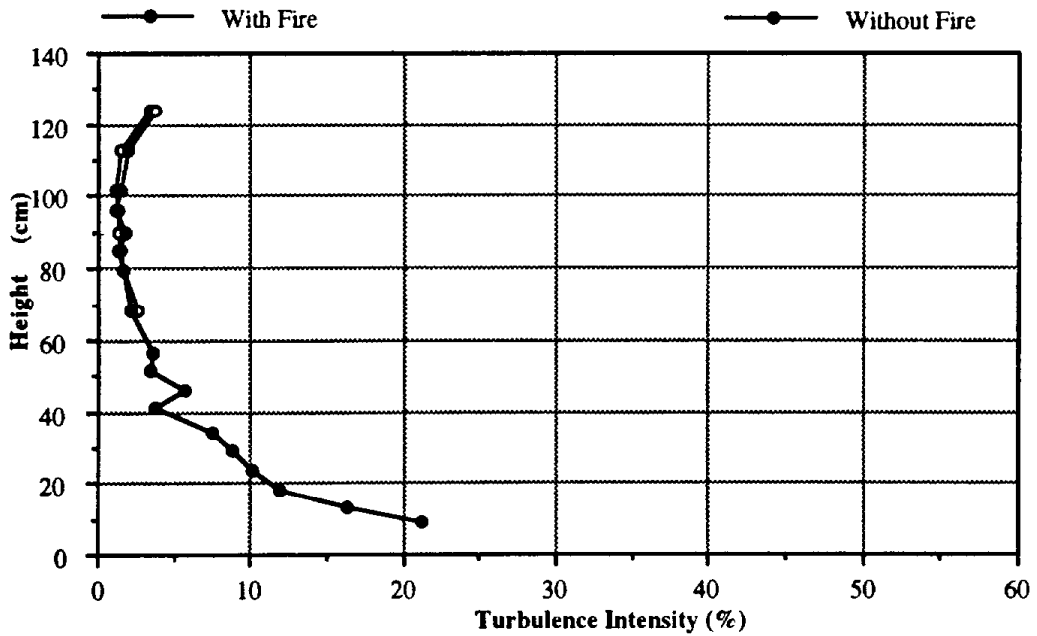


Figure 7p. Vertical turbulence intensity, CEWF, low wind speed, downstream position.

than the cold flow. Both positions showed a relatively deep boundary layer over the fuel surface. No ceiling boundary layer was apparent at the downstream location, but the remnant of a ceiling boundary layer was suggested by the slower velocities at the top of the traverse in the upstream cold flow case.

The vertical velocity profiles for the upstream and downstream positions are shown in Figure 8b and Figure 8f, respectively. Although they are similar to each other, they are quite different from the vertical velocity profiles in the ceiling extended configurations. With the ceiling retracted, there was considerable upward velocity, increasing to 0.7 - 0.9  $\text{m s}^{-1}$  at the top of the traverse.

The streamwise and vertical turbulence intensities for the high wind speed upstream position are plotted in Figures 8c and 8d, respectively. The corresponding downstream profiles can be seen in Figures 8g and 8h. Freestream intensities were 2-3% in the streamwise direction and 1-2 % in the vertical direction. The intensities increased as the fuel surface was approached to a maximum of about 40% in the streamwise direction and about 15% in the vertical direction. Moving downwards from the top of the traverse, the upstream hot flow turbulence intensities were greater than those in cold flow.

The low speed streamwise velocity profiles appear in Figure 8i for the upstream position and in Figure 8m for the downstream position. These profiles are distinctly different from any observed with the ceiling extended or at the higher wind speed. At the upstream position, the flow was more or less constant at 0.25  $\text{m s}^{-1}$  between 10 and 30 cm above which it increased with height to a maximum of 1.5  $\text{m s}^{-1}$  cold flow and 1.9  $\text{m s}^{-1}$  hot flow. The downstream cold flow condition exhibited this constant velocity region between 10 and 40 cm. Above, the velocity increased to about 1.6  $\text{m s}^{-1}$ .

The corresponding vertical velocities are plotted in Figures 8j and 8n. Unlike the high wind speed vertical velocities with the ceiling retracted (which started at zero and increased approximately linearly with height), the low wind speed vertical velocities remained essentially zero until a height of 45 cm at the upstream location, and approximately 60 cm at the downstream location. At both the upstream and downstream locations, the hot flow reached a maximum vertical velocity of about 0.4  $\text{m s}^{-1}$  and the cold flow reached a maximum of 0.5  $\text{m s}^{-1}$ .

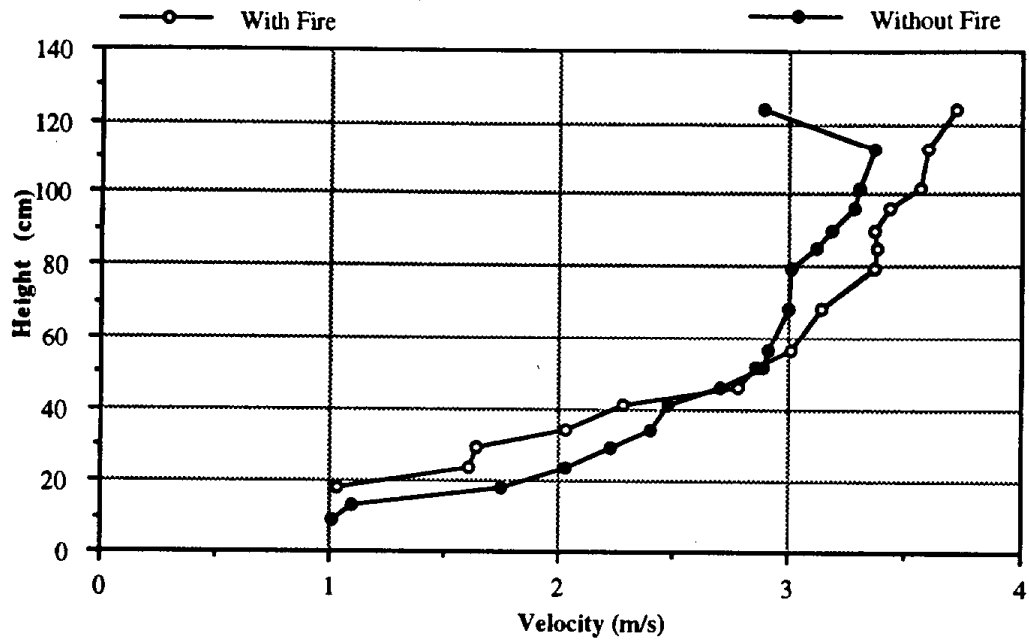


Figure 8a. Streamwise velocity, CRNF, high wind speed, upstream position.

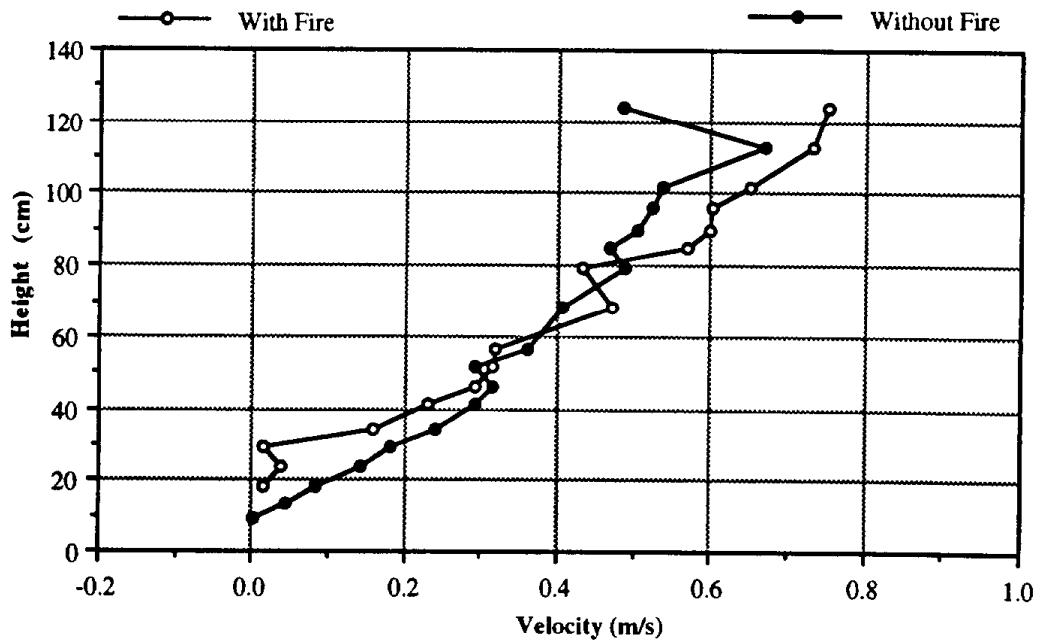


Figure 8b. Vertical velocity, CRNF, high wind speed, upstream position.

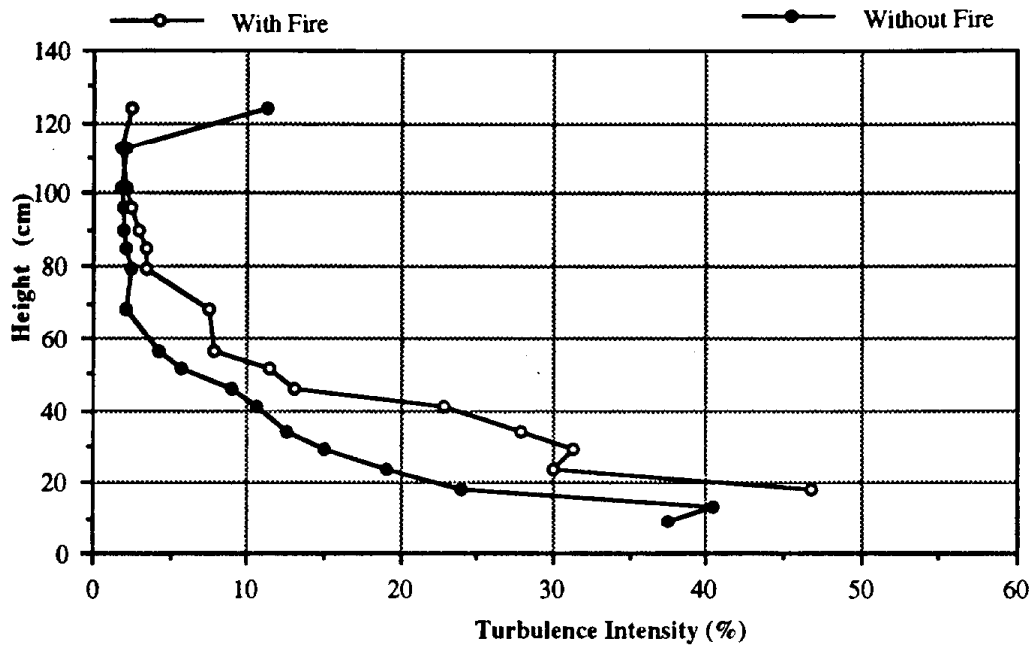


Figure 8c. Streamwise turbulence intensity, CRNF, high wind speed, upstream position.

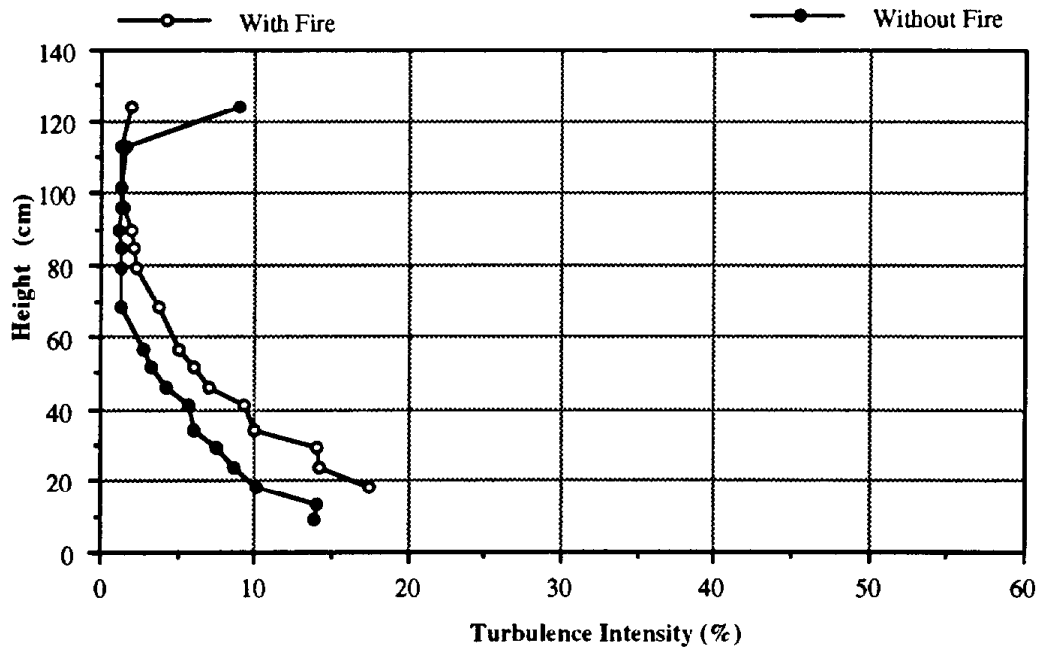


Figure 8d. Vertical turbulence intensity, CRNF, high wind speed, upstream position.

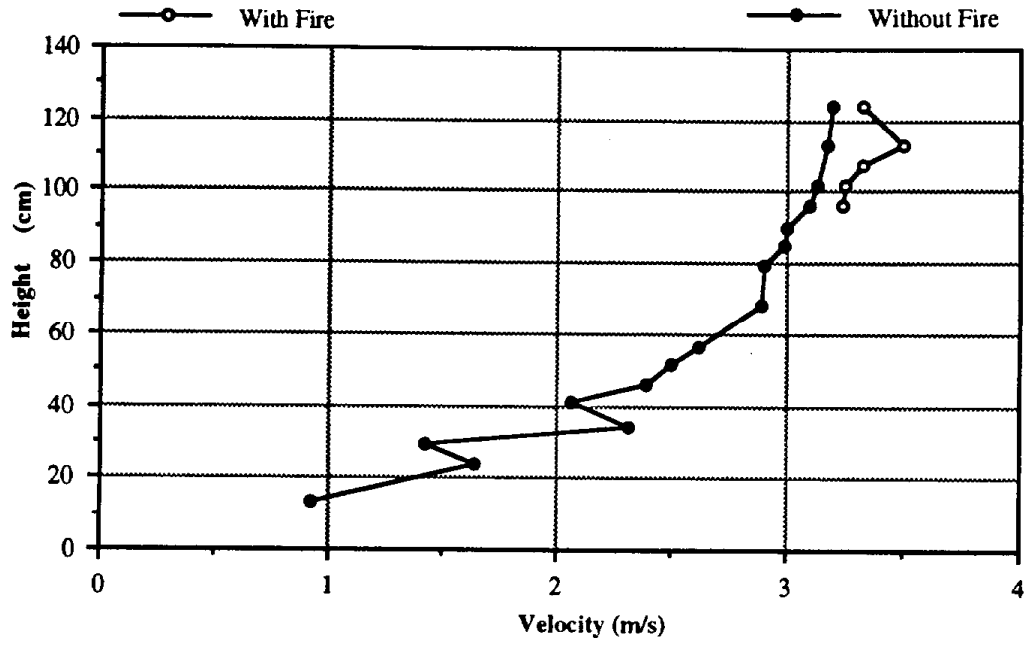


Figure 8e. Streamwise velocity, CRNF, high wind speed, downstream position.

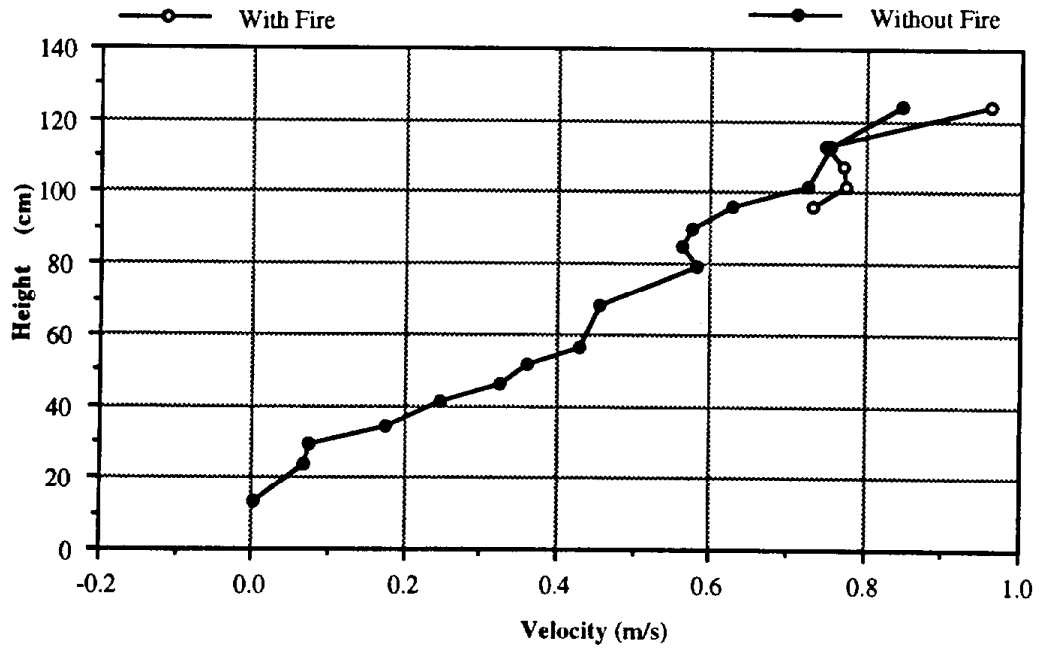


Figure 8f. Vertical velocity, CRNF, high wind speed, downstream position.

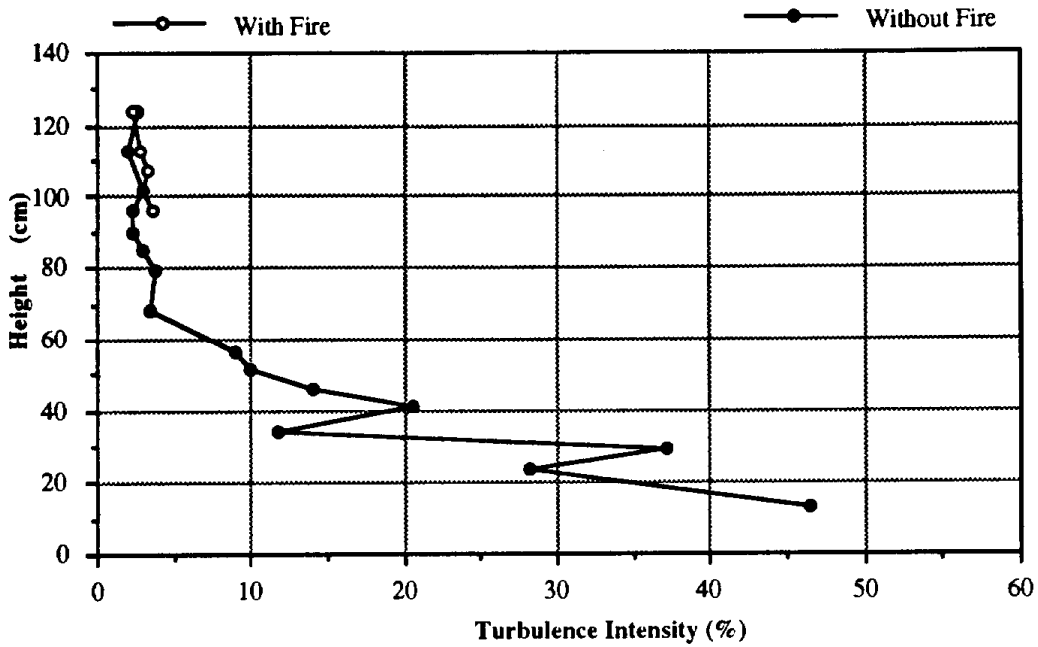


Figure 8g. Streamwise turbulence intensity, CRNF, high wind speed, downstream position.

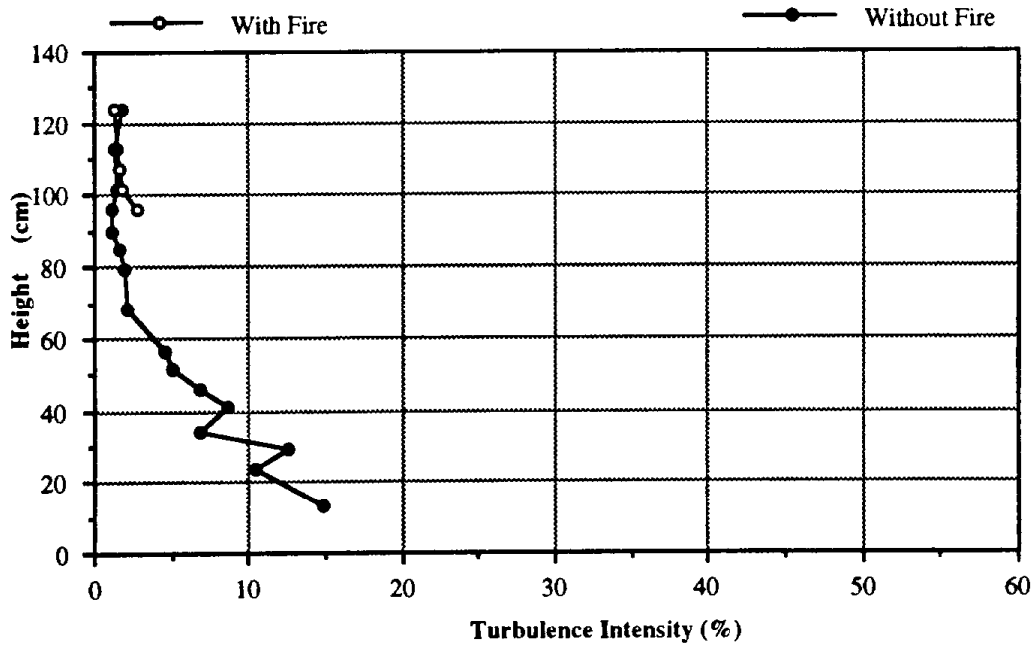


Figure 8h. Vertical turbulence intensity, CRNF, high wind speed, downstream position.

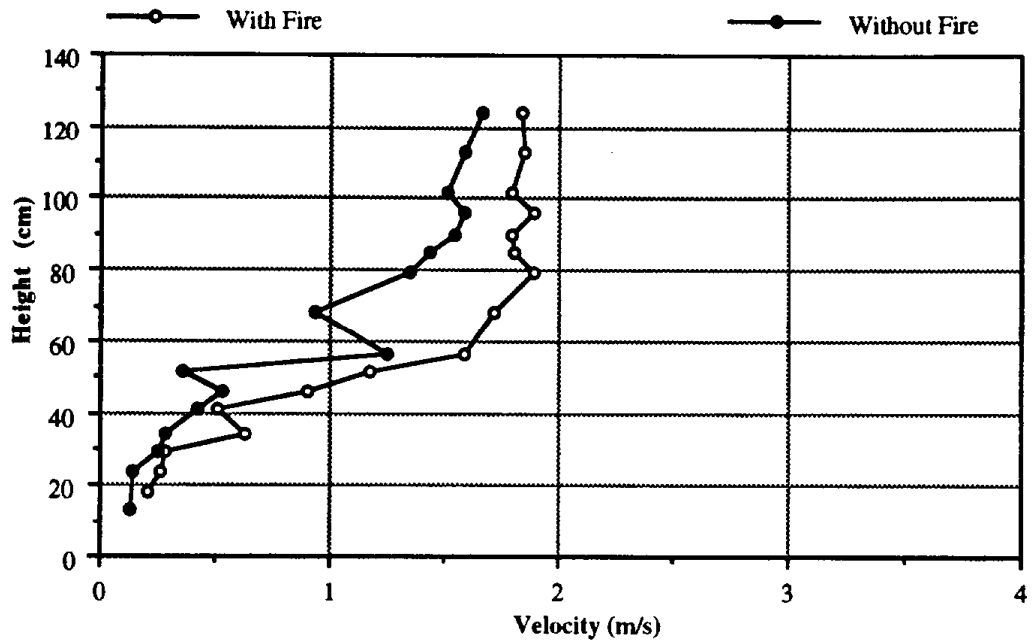


Figure 8i. Streamwise velocity, CRNF, low wind speed, upstream position.

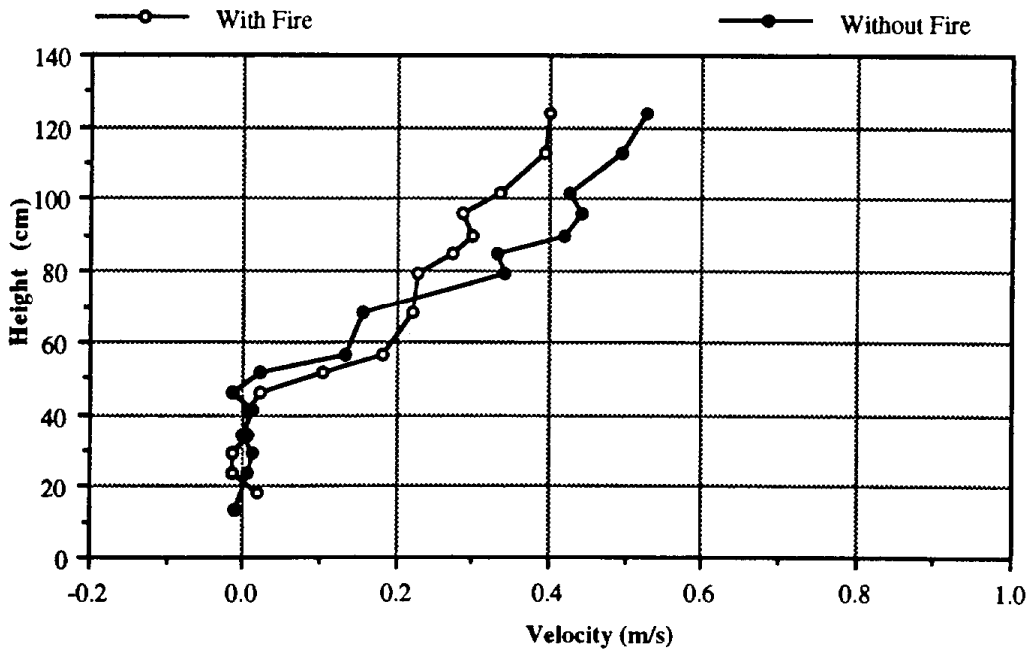


Figure 8j. Vertical velocity, CRNF, low wind speed, upstream position.

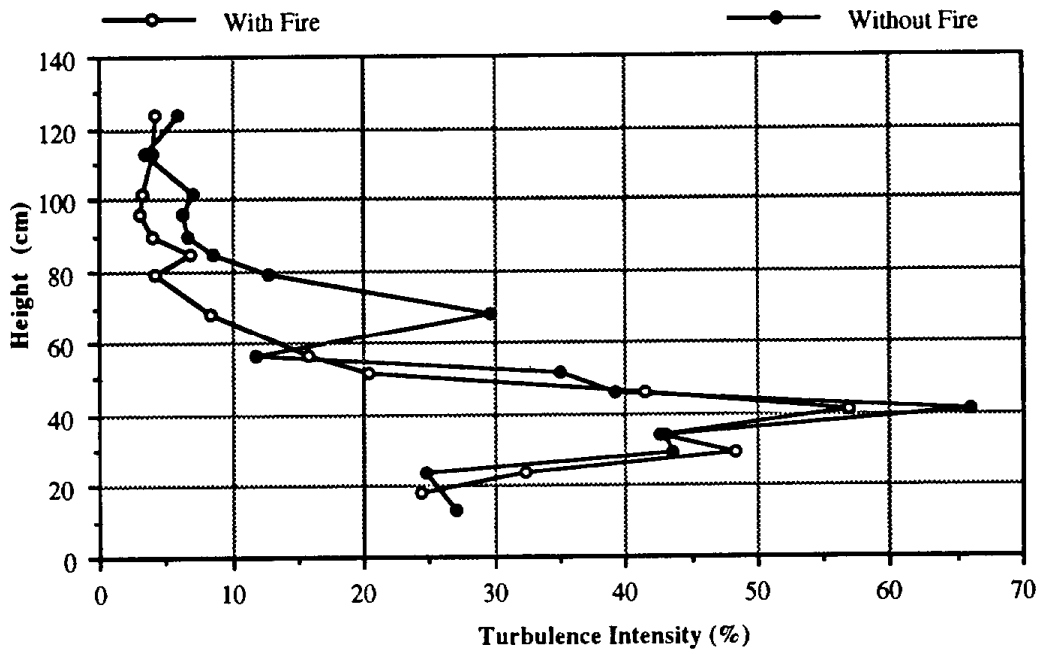


Figure 8k. Streamwise turbulence intensity, CRNF, low wind speed, upstream position.

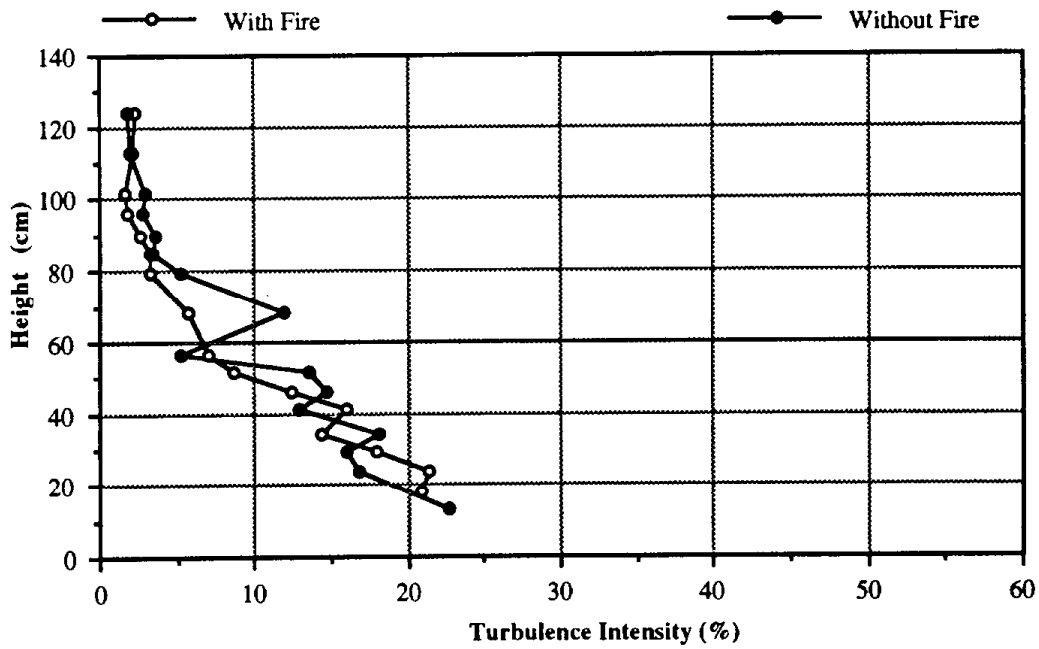


Figure 8l. Vertical turbulence intensity, CRNF, low wind speed, upstream position.

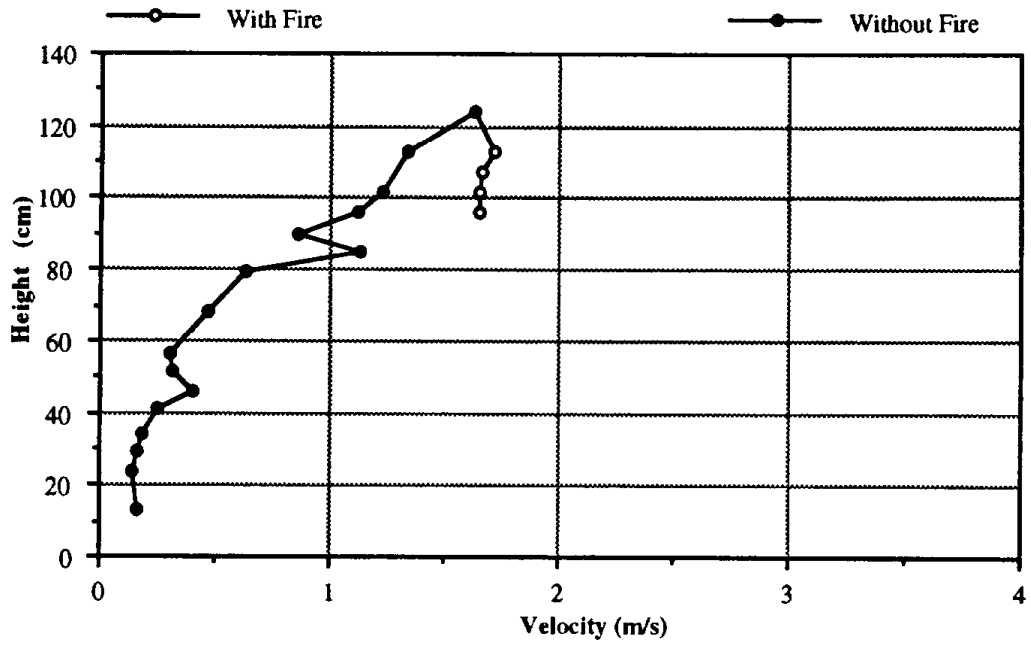


Figure 8m. Streamwise velocity, CRNF, low wind speed, downstream position.

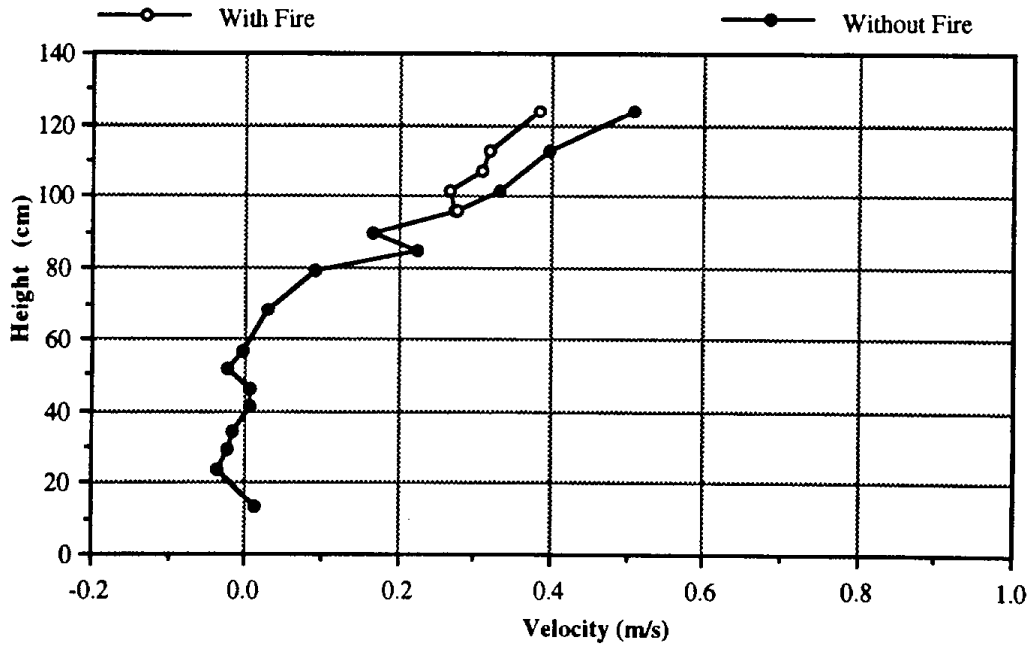


Figure 8n. Vertical velocity, CRNF, low wind speed, downstream position.

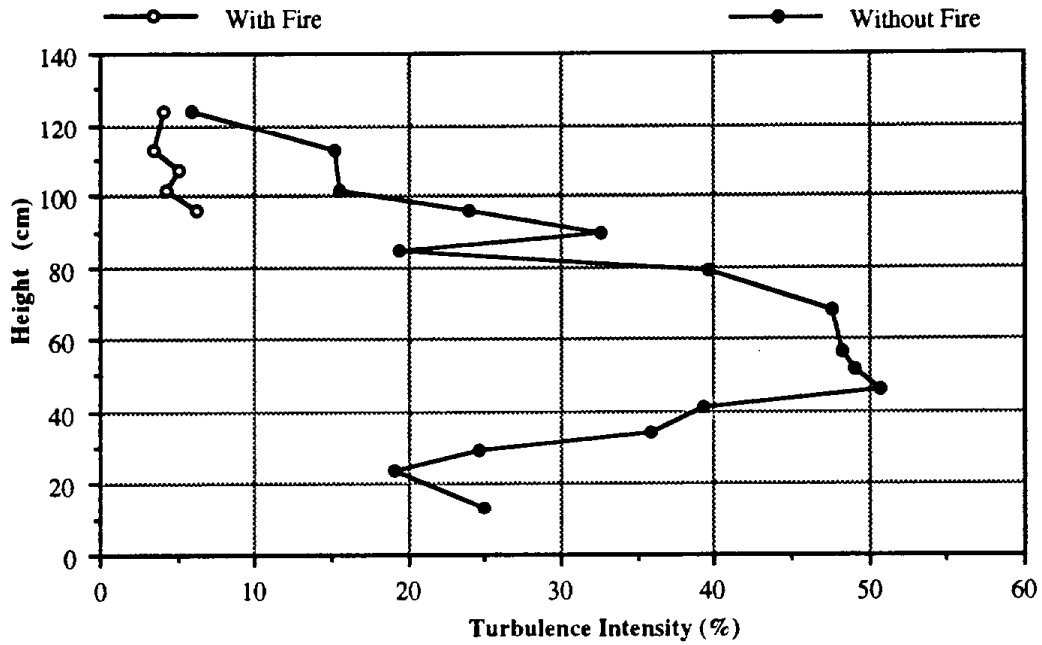


Figure 8o. Streamwise turbulence intensity, CRNF, low wind speed, downstream position.

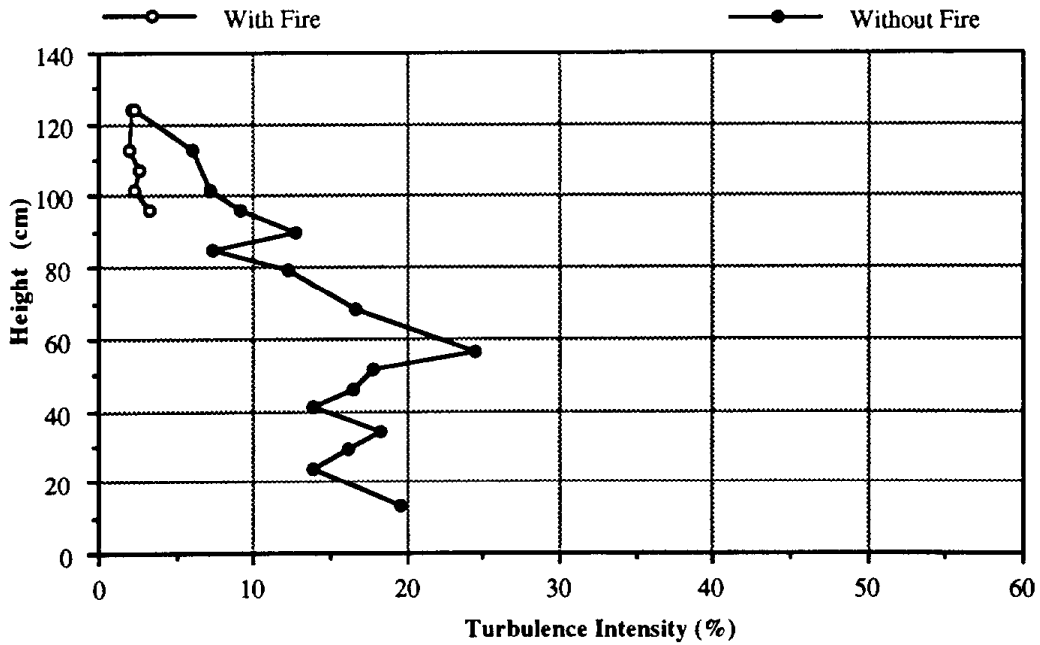


Figure 8p. Vertical turbulence intensity, CRNF, low wind speed, downstream position.

The upstream streamwise and vertical turbulence intensities for the low wind speed are shown in Figures 8k and 8l, respectively. The downstream turbulence intensities are shown in Figures 8o and 8p. The magnitudes in the freestream were 5-8% for the streamwise direction and 2-4% in the vertical direction. The streamwise turbulence intensities reached maximum values of 50 to 60% just above the region of constant velocity below 40 cm. The upstream vertical turbulence intensities decreased with increasing height from a maximum of 23%. The cold flow downstream turbulence intensities both showed an increase with a decrease in height downwards to the top of the constant velocity region. Below that level the streamwise intensities declined.

Streamwise velocity profiles were integrated over height to obtain average wind speed in the profile. The results are shown in Table 3. The average velocity was higher in hot flow than in cold flow due to the buoyancy introduced by the fire. The relative increase was greater at low speed than at high speed, which is consistent with the greater relative buoyancy strength at lower velocity (13). Taking representative conditions for both configurations, the relative buoyancy strength,  $(T_{st} - T_0)/T_0$ , where  $T_{st}$  is the stack gas temperature and  $T_0$  is the reference inlet temperature, is 20% greater at the low wind speed than at the high wind speed.

The thickness of the boundary layer,  $\delta$ , above the fuel surface was also determined when a boundary layer was observed to be reasonably well developed. Intermittency was not considered for this analysis. The top of the boundary layer is generally evident where turbulence intensity begins to increase from its low, nearly constant value in the freestream. The Reynolds stress was also used in estimating the boundary layer thickness. In the boundary layer, the Reynolds stress is non-zero, but in the freestream, with constant streamwise velocity, the Reynolds stress vanishes. Intermittent turbulence at the edge of the boundary layer makes the boundary layer thickness more difficult to define. Both methods for determining  $\delta$  were in fairly good agreement, and averages are given in Table 3. The traverse depth was insufficient to determine  $\delta$  for all of the downstream hot flow tests. Developed boundary layers were not observed in the CRNF low wind speed configurations, although in one case (upstream, hot, see Figure 8i), an apparent depth was determined. With the higher wind speed, the hot flow boundary layers tend to be thicker than the cold flow, which would be expected from the higher velocities in hot flow. Boundary layers are turbulent for Reynolds numbers based on momentum thickness of 5000 and possibly lower (25). For the configurations tested here, the momentum

thickness Reynolds numbers range from 9,000 at the lower wind speeds to 19,000 at the higher wind speeds.

Table 3. Computed wind speed, boundary layer thickness, roughness height, and friction velocity.

Configuration	Integrated Wind Speed (m s <sup>-1</sup> )	Position	Flow Condition	$\delta$ (m)	$z_0$ (m)	$u^*$ (m s <sup>-1</sup> )
CEWF	2.98	upstream	cold	0.45	0.023	0.42
CEWF	3.19	upstream	hot	0.65	0.050	0.61
CEWF	2.93	downstream	cold	0.60	0.055	1.26
CEWF	3.16	downstream	hot	0.65*	*	*
CEWF	1.53	upstream	cold	0.70	0.096	0.44
CEWF	1.71	upstream	hot	0.55	0.131	0.60
CEWF	1.53	downstream	cold	0.60	0.119	0.45
CEWF	*	downstream	hot	*	*	*
CRNF	2.75	upstream	cold	0.60	0.047	0.49
CRNF	2.77	upstream	hot	0.80	0.090	0.63
CRNF	2.52	downstream	cold	0.70	0.069	0.51
CRNF	*	downstream	hot	*	*	*
CRNF	0.96	upstream	cold	+	0.352+	0.69+
CRNF	1.29	upstream	hot	0.60+	0.298+	0.94+
CRNF	0.65	downstream	cold	+	0.540+	0.81+
CRNF	*	downstream	hot	*	*	*

\* partial traverse.

+ fully developed boundary layer not observed.

Estimates of roughness heights and friction velocities are also listed in Table 3. Roughness heights varied from about 0.02 to 0.13 m, except in the case of the CRNF low wind speed tests. The roughness heights estimated for these tests were much higher as a result of the low velocity regions extending upwards from the fuel surface. Friction velocities were 0.4 to 0.6 m s<sup>-1</sup>, with the exception of one CEWF high wind speed configuration and the CRNF low wind speed configurations. The model fit of equation [9] (page 20) is good for the CEWF configurations, and for the higher speed CRNF configurations. An example is given in Figure 9.

The velocity profiles for the CEWF high wind speed and CRNF low wind speed configurations are distinctly different. The difference is more readily seen by the similarity analysis of Figure 10. The average velocity has been divided by the velocity at the "edge" of the boundary layer,  $U_e$ , taken at a height  $\delta$ . The height,  $z$ , has been divided by the

boundary layer height,  $\delta$ . Three profiles are shown. Upstream positions are used because full traverses are available in all three cases. The CEWF high wind speed configuration in both cold and hot flow displays characteristics of an adverse pressure gradient (26) which is not unexpected in this tunnel. The CRNF low wind speed configuration exhibits the characteristics of a flow in an extremely adverse pressure gradient, with a separated flow. Thus it makes little sense to attempt to model the CRNF low wind speed profiles using the logarithmic law-of-the-wall, as this model is not valid under these conditions. The values given for  $z_0$  and  $u^*$  therefore should not be construed as meaningful in these cases. Potential complications arise in this interpretation because of the possibility for secondary flows originating at the junction between the flexible conveyor and the rod conveyor, particularly from buoyancy induced entrainment at the lower wind speeds. The potential for such flows was subsequently removed by sealing this area.

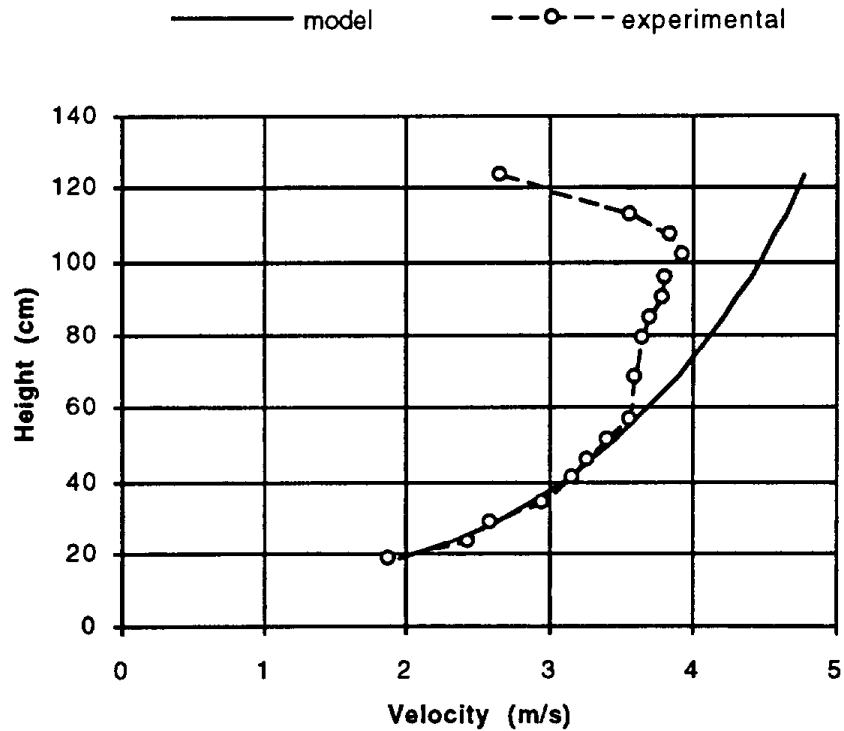


Figure 9. Velocity profile, CEWF, with fire, high wind speed, upstream position, with logarithmic law-of-the-wall model shown for comparison ( $u^* = 0.61 \text{ m s}^{-1}$ ,  $z_0 = 0.05 \text{ m}$ ).

Energy spectra for the CEWF high wind speed, hot flow condition, at the upstream position are shown in Figure 11. Those for the CRNF low wind speed, hot flow condition, upstream position are shown in Figure 12. The spectrum for each of four different heights above the rod conveyor is given in each graph. The abscissa in each case has been stretched for clarity. The highest wavenumber in each spectrum is always between  $10^3$  and  $10^4$  for the high wind speed configuration in Figure 11. This is also true for the spectra in Figure 12 with the exception of that at 180 mm height, for which the range extends to  $10^5$  because of the low velocity at this height in this configuration.

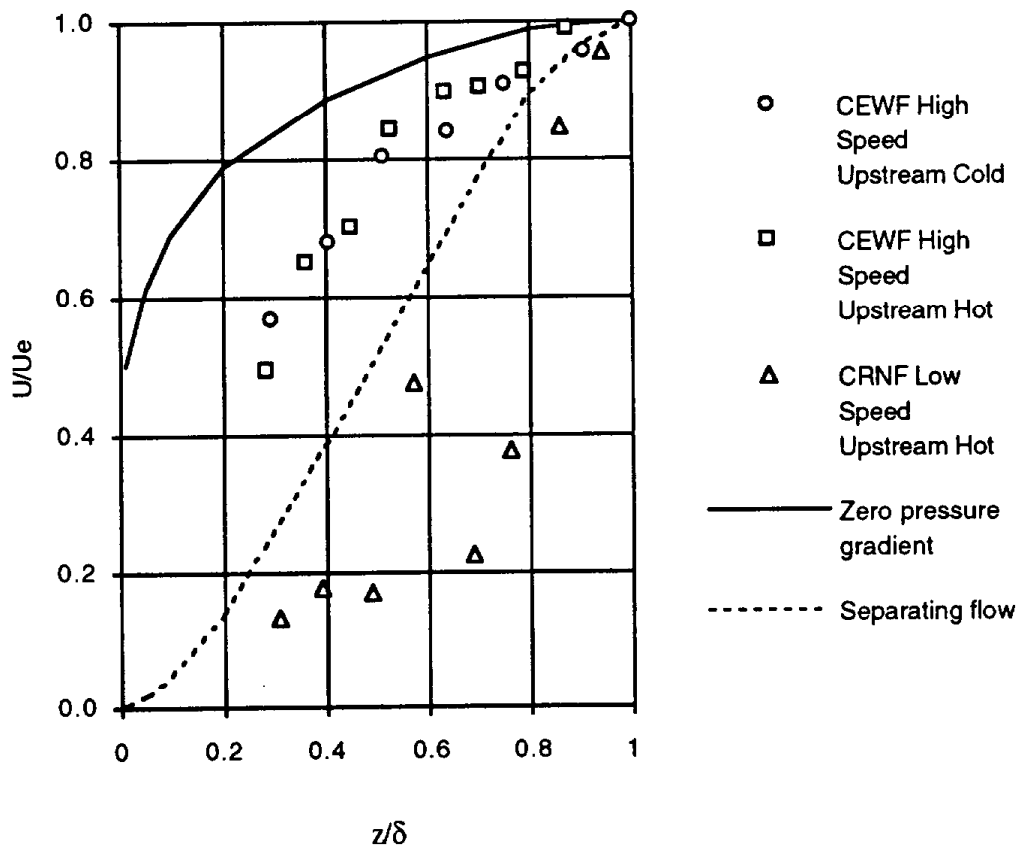


Figure 10. Non-dimensional velocity profiles for CEWF high wind speed and CRNF low wind speed configurations (data for zero pressure gradient and separating flows from reference 26, p 470).

The spectra for the three lowest positions in Figure 11 all exhibit a region of wavenumbers extending from about 10 to 700 where  $E$  varies as  $\kappa_1^{-5/3}$ . Maximum energy at  $\kappa_1$  near  $5 - 10 \text{ m}^{-1}$  for the 180 mm height suggests an integral length scale on the order of 0.1 - 0.2 m, although the data are sparse in this region. A maximum is not clearly seen for the other two locations in the boundary layer. Results from autocorrelations at all three locations give integral length scales of 0.16 - 0.19 m. The spectrum for the 800 mm height does not give a  $-5/3$  slope as it is outside the boundary layer. The autocorrelation at this height gives an integral length scale of 0.65 m, which is within the physical limit imposed by the width and height of the tunnel. The dissipation range starts at wavenumbers around 700 for the lower positions. Visually, the spectra suggest the Kolmogorov scale,  $\eta$ , may be on the order of 0.3 - 0.5 mm at wavenumbers of 2000 - 3000  $\text{m}^{-1}$ . The Kolmogorov scale and the integral length scale are related by (14),

$$\frac{\eta}{\ell} = \left( \frac{U\ell}{\nu} \right)^{-3/4} = \text{Re}_\ell^{-3/4} \quad [16]$$

where  $\ell$  is the integral length scale (m),  $\nu$  is the kinematic viscosity ( $\text{m}^2 \text{s}^{-1}$ ), and  $\text{Re}_\ell$  is the Reynolds number. For  $\ell = 0.16 \text{ m}$  and  $U = 2 \text{ m s}^{-1}$ ,  $\eta = 0.1 \text{ mm}$ , which suggests a Kolmogorov scale at wavenumbers of  $10^4$ , which is beyond the range observed for a 2.2 kHz sampling frequency. Equation [16] applied in the freestream also gives  $\eta$  on the order of 0.1 mm.

Because of the dependence of  $\kappa_1$  on  $U$ , the low velocities in the CRNF low wind speed configuration extend the spectra of Figure 12 over an additional decade at the lower positions. The poor boundary layer development in this configuration shifts the spectrum at 180 mm relative to the other heights. Although there is still a region of  $-5/3$  slope in each of the three lowest spectra, there is no clear point of maximum energy. Nor is the dissipation range well defined. Autocorrelations yield  $0.12 \leq \ell \leq 0.15 \text{ m}$  between 180 and 510 mm height, and  $\ell = 0.77 \text{ m}$  at 800 mm height. For  $U = 0.25 \text{ m s}^{-1}$ , equation [16] suggests  $\eta = 3 \text{ mm}$ , which corresponds to wavenumbers of 300. At 500 mm, equation [16] suggests  $\eta = 1 \text{ mm}$ , and in the freestream at 800 mm,  $\eta = 0.2 \text{ mm}$ . The peculiar nature of the flow in the CRNF low wind speed configuration causes the characteristic small scales to vary over the profile. The application of Taylor's hypothesis is at any rate questionable for this flow.

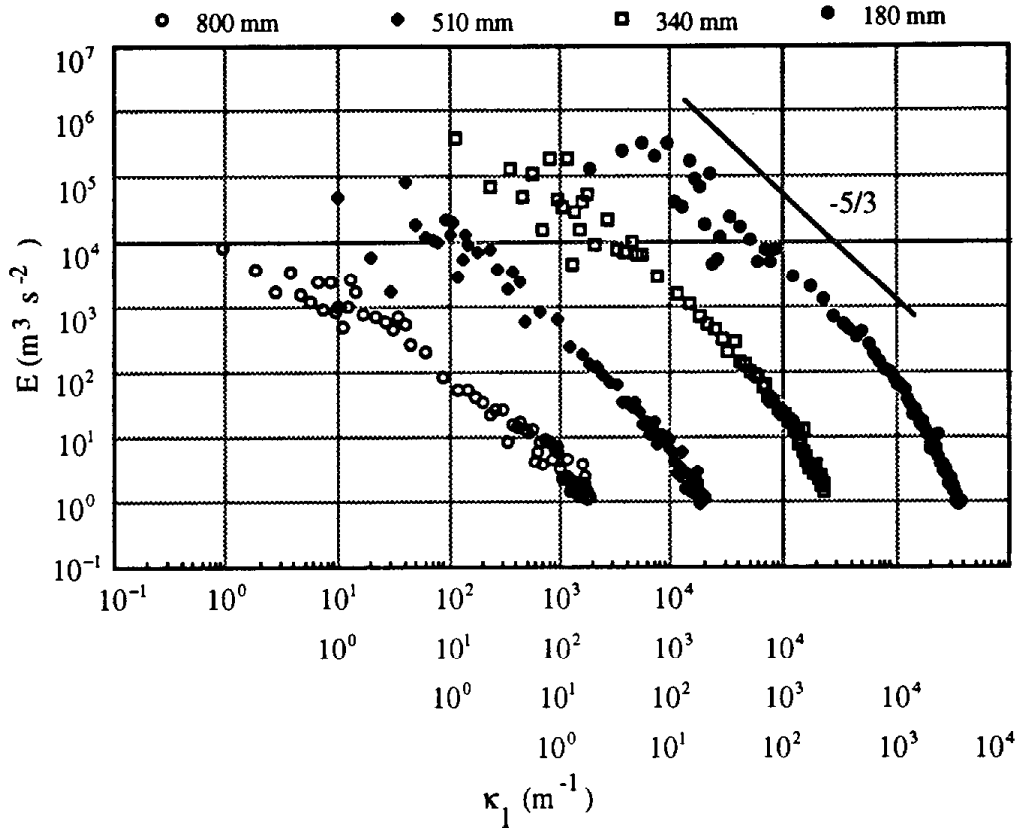


Figure 11. Energy spectrum, CEWF, with fire, high wind speed, upstream position (locations shown are height above rod conveyor).

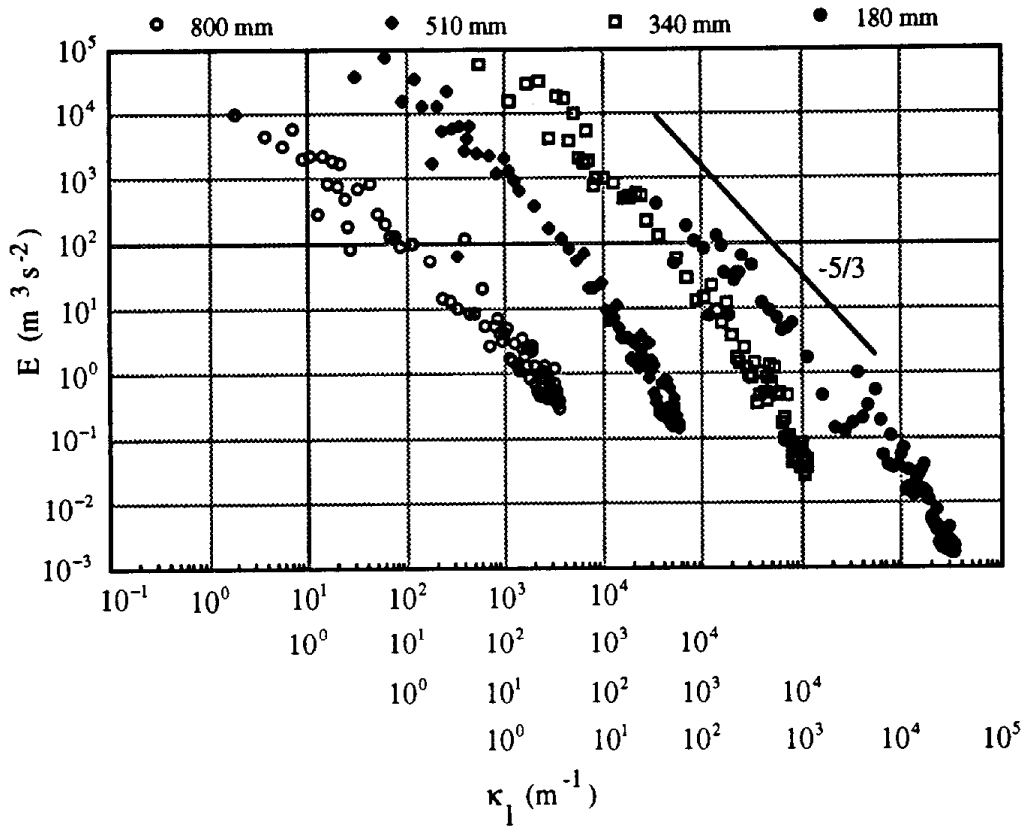


Figure 12. Energy spectrum, CRNF, with fire, low wind speed, upstream position (locations shown are height above rod conveyor).

Particle Size Distributions:

Particle size distributions for replicated experiments of the CEWF high wind speed configuration are shown in Table 4a, while those for the CRNF low wind speed configuration are shown in Table 4b. Computed mass median aerodynamic diameters (MMAD) and geometric standard deviations ( $\sigma_g$ ) are also shown. All distributions showed a large fraction of fine particulate matter, with 70% or more collected on the final filter stage of the cascade impactor. The distributions generally reached a minimum at around 2 to 5  $\mu\text{m}$ , with increasing mass collected on the larger stages. No substantial differences were seen between the CEWF high speed and CRNF low speed configurations. The CEWF experiments bracket the CRNF experiments in MMAD.

Table 4a. Particle size distributions for replicates of CEWF high wind speed configuration.

1.					2.				
MMAD = 0.101 $\mu\text{m}$ $\sigma_g = 3.92$					MMAD = 0.062 $\mu\text{m}$ $\sigma_g = 3.38$				
Stage	Effective Diameter ( $\mu\text{m}$ )	Mass (mg)	Mass Fraction (%)	Cumulative Mass Fraction (%)	Stage	Effective Diameter ( $\mu\text{m}$ )	Mass (mg)	Mass Fraction (%)	Cumulative Mass Fraction (%)
1	13.69	0.3	4.2	100.0	1	13.57	0.5	7.4	100.0
2	7.67	0.1	1.4	95.8	2	7.60	0.1	1.5	92.6
3	4.09	0.1	1.4	94.4	3	4.05	0.0	0.0	91.2
4	2.16	0.1	1.4	93.0	4	2.14	0.0	0.0	91.2
5	1.24	0.2	2.8	91.5	5	1.23	0.2	2.9	91.2
6	0.73	0.4	5.6	88.7	6	0.73	0.3	4.4	88.2
7	0.38	0.5	7.0	83.1	7	0.38	0.5	7.4	83.8
filter		5.4	76.1	76.1	filter		5.2	76.5	76.5

Table 4b. Particle size distributions for replicates of CRNF low wind speed configuration.

1.					2.				
MMAD = 0.087 $\mu\text{m}$ $\sigma_g = 3.57$					MMAD = 0.091 $\mu\text{m}$ $\sigma_g = 4.32$				
Stage	Effective Diameter ( $\mu\text{m}$ )	Mass (mg)	Mass Fraction (%)	Cumulative Mass Fraction (%)	Stage	Effective Diameter ( $\mu\text{m}$ )	Mass (mg)	Mass Fraction (%)	Cumulative Mass Fraction (%)
1	15.61	0.5	4.9	100.0	1	15.56	0.7	5.6	100.0
2	8.74	0.2	1.9	95.1	2	8.72	0.4	3.2	94.4
3	4.66	0.3	2.9	93.2	3	4.65	0.4	3.2	91.1
4	2.47	0.2	1.9	90.3	4	2.46	0.3	2.4	87.9
5	1.42	0.1	1.0	88.3	5	1.41	0.3	2.4	85.5
6	0.83	0.4	3.9	87.4	6	0.83	0.5	4.0	83.1
7	0.44	0.5	4.9	83.5	7	0.43	0.7	5.6	79.0
filter		8.1	78.6	78.6	filter		9.1	73.4	73.4

Temperature profiles:

Isotherms from the thermocouple array are plotted in Figures 13 and 14 for the CEWF high wind speed and CRNF low wind speed configurations, respectively. Also shown are representative relative frequency densities for the flame tip, flame center, and fuel surface derived from measurements with the fast response type-R thermocouple. Sampling locations are indicated on the graphs. The time scale of the original measurements was converted to distance (travel) by the measured spreading rate for each experiment. Profiles showing means and standard deviations of temperature from measurements with the fast response thermocouple are shown in Figures 15 and 16 for two traverses in each configuration--upwards through the flame center, and upwards over a region of glowing combustion 150-200 mm behind the flame.

Distinct differences existed in the flame shape for the two configurations. The CEWF high wind speed configuration exhibited high flame tilt and short flame length. The burning zone length in the bed was 550 to 600 mm, with a duration of approximately 60 s. The flame angle was about 30° from the horizontal, and was substantially shallower than the flame angle in the CRNF configuration. The flaming zone in the bed was approximately 300 mm long, with a region of glowing combustion extending behind for another 200 - 300 mm. The flame length was approximately 400 mm.

The CRNF low speed configuration gave tall, erect flames with flame angles in excess of 60° from the horizontal. The burning zone in the fuel bed was 600 to 650 mm in length, corresponding to a duration of about 50 s. The flaming zone extended about 200 mm behind the front, with a region of glowing combustion extending beyond. Cooling was quite rapid behind the flame (Figure 14), apparently due to entrainment of air from below the fuel bed. Increasing the wind speed for this configuration caused the flame to become noticeably tilted, with an angle of 40 to 50°, and a burning length varying between 500 and 1,000 mm. Flame length was about 600 mm.

The relative frequency densities of temperature are similar in many respects, differences being due principally to the greater unsteadiness of the flame with the higher wind speed in the CEWF configuration. Peak temperatures measured at the fuel surface were somewhat lower in the CEWF configuration, 1200 vs. 1350°C for the CRNF configuration, but this is likely due to the relatively poor frequency response of the thermocouple (about 200 Hz).

Some averaging would therefore have occurred as the thermocouple was exposed to higher frequency turbulent fluctuations of the flow between ambient and flame temperature. As indicated earlier, true peak temperatures were no doubt higher than measured. Heat loss from the thermocouple along with averaging in the turbulent flame would reduce the measured temperature below the actual flame temperature. True flame temperatures are probably below 1700°C due to heat loss from soot radiation. Soot particle temperatures of 1480°C have been measured by emission and absorption of near-infrared radiation in an atmospheric pressure, laminar ethylene-air diffusion flame (27).

Shown in Figure 17 are the temperature contours and relative frequency densities for the CENF high wind speed configuration. This configuration differs markedly from the CEWF case at the same speed. The flame angle is also about 30°, but the flame is comparable in length to the CRNF configuration (about 600 mm). The flame shape appeared to be sensitive to both the ceiling and floor configurations. Flame length was increased by removing the floor or retracting the ceiling. The CENF configuration resembles temperature profiles collected during an actual field burn in rice straw. An example is shown in Figure 18.

#### Flame Radiation:

Flame radiation results for all configurations are shown in Figures 19a and b. The results are plotted against the distance D between the leading edge of the fire at the fuel surface and the heat flux sensor, as in Figure 5. All values have been corrected for background.

Total emitted power averaged over all samples in each configuration is given in Table 5. Total flame radiation ranged from 8 to 20 kW, with a mean of 13 kW. Total heat release by the fire was computed from the loading rate, spreading velocity, residual ash fraction, and the heating values of the fuel (16 MJ/kg) and ash (5 MJ/kg). The total heat release averages about 107 kW. Of this, flame radiation accounts for 8 to 20%, with an average of 12%. The emitted fraction is also shown graphically for all configurations in Figure 20. The emitted fraction tends to be higher with the ceiling extended. Both low wind speed configurations with the floor installed (CEWF low and CRWF low) have higher emitted fractions than the other configurations with the same ceiling position. Average spreading rate was not clearly correlated with average emitted fraction.

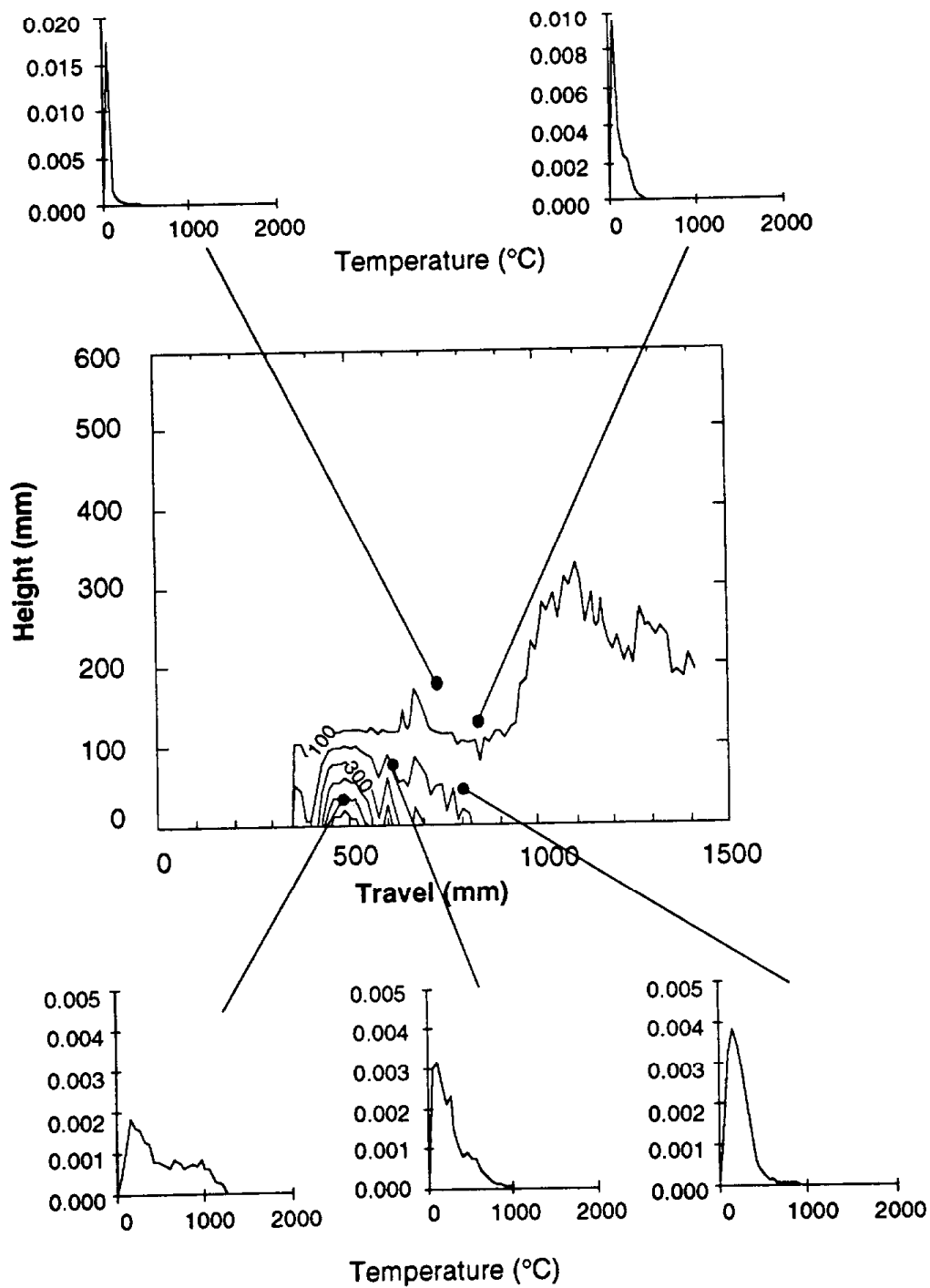


Figure 13. Temperature contours and relative frequency densities of temperature from fast response thermocouple at indicated positions in flame, CEWF high wind speed configuration. Contour interval = 100°C, height given above fuel surface.

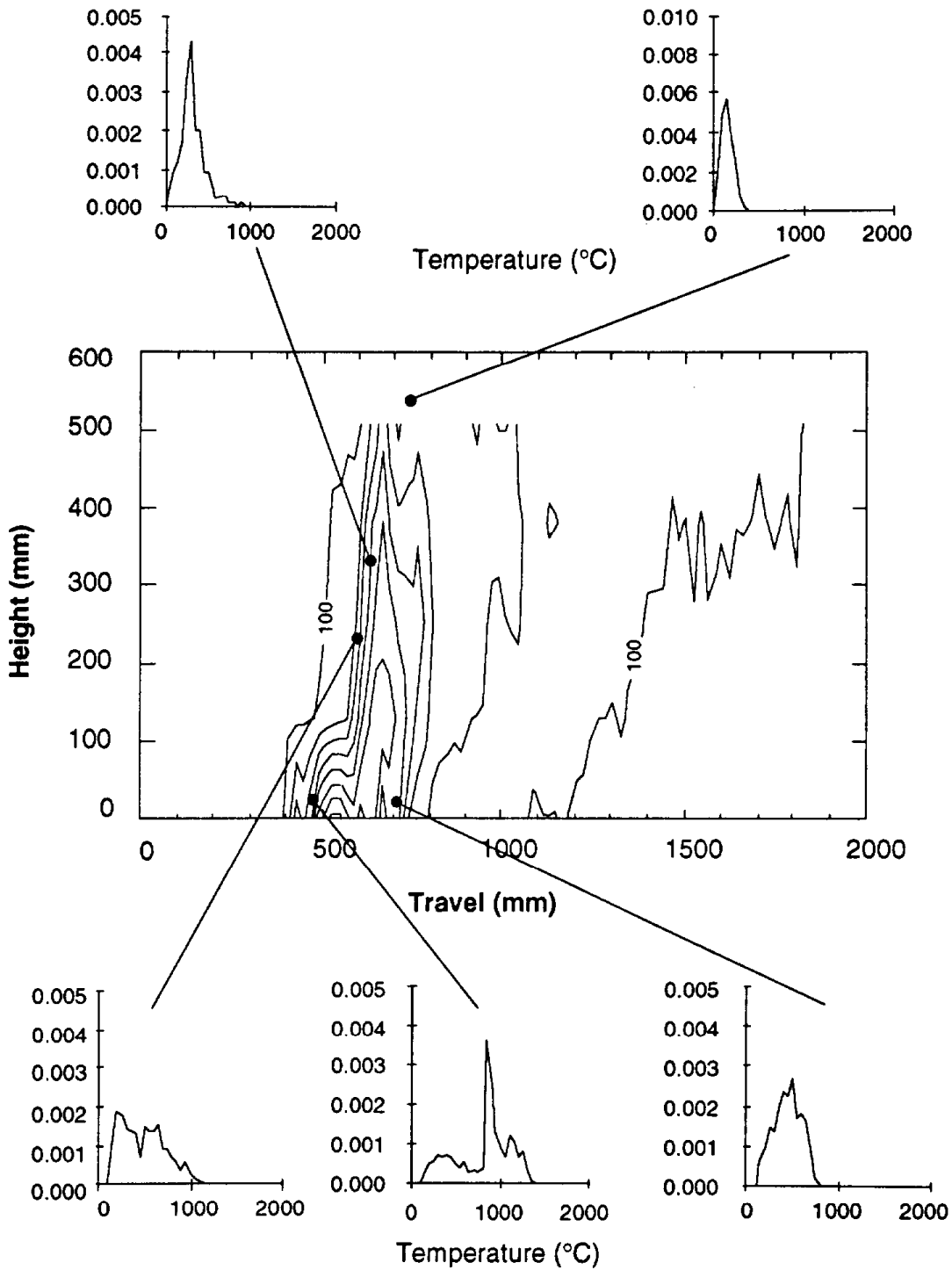
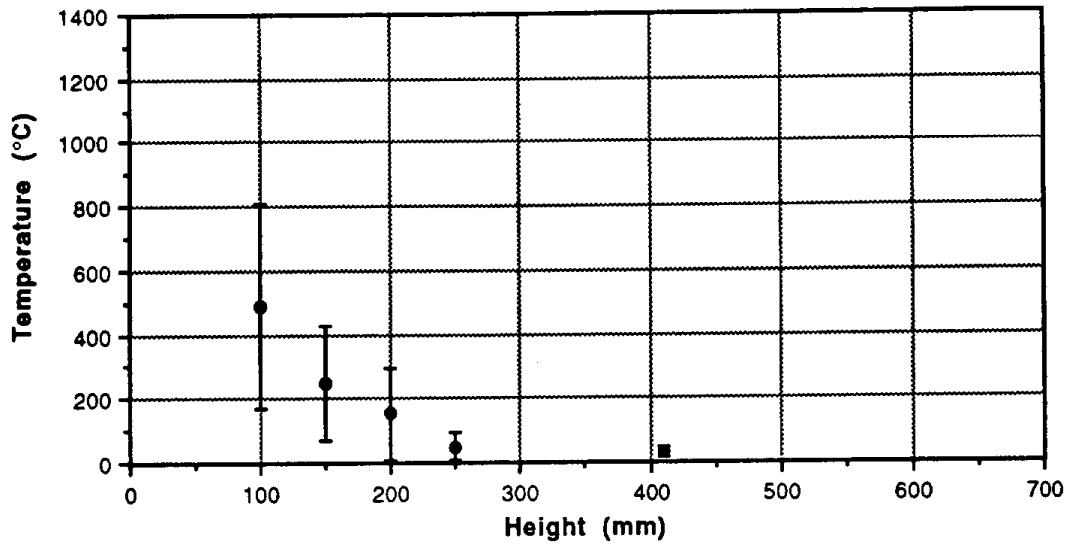
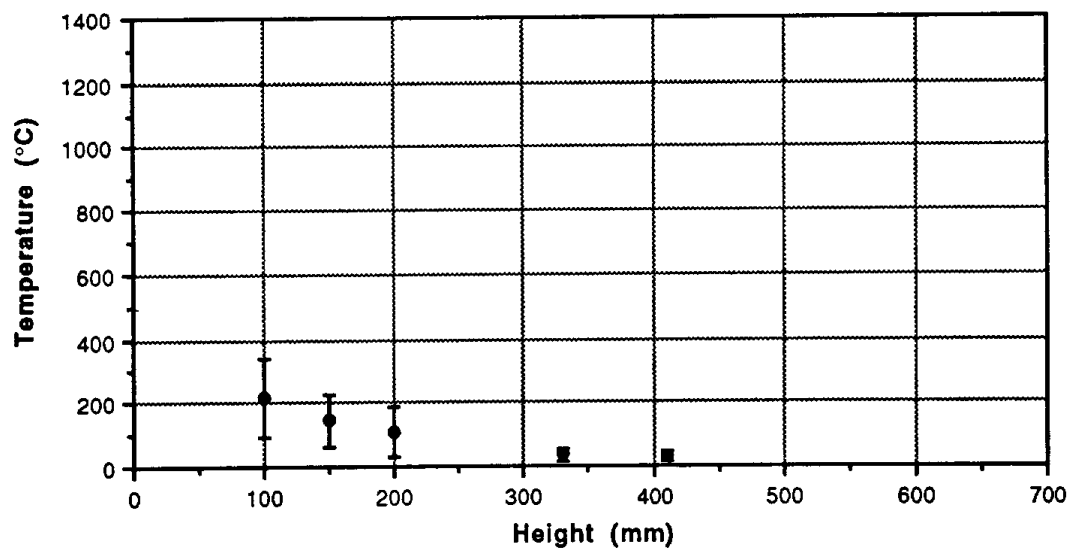


Figure 14. Temperature contours and relative frequency densities of temperature from fast response thermocouple at indicated positions in flame, CRNF low wind speed configuration. Contour interval = 100°C, height given above fuel surface.

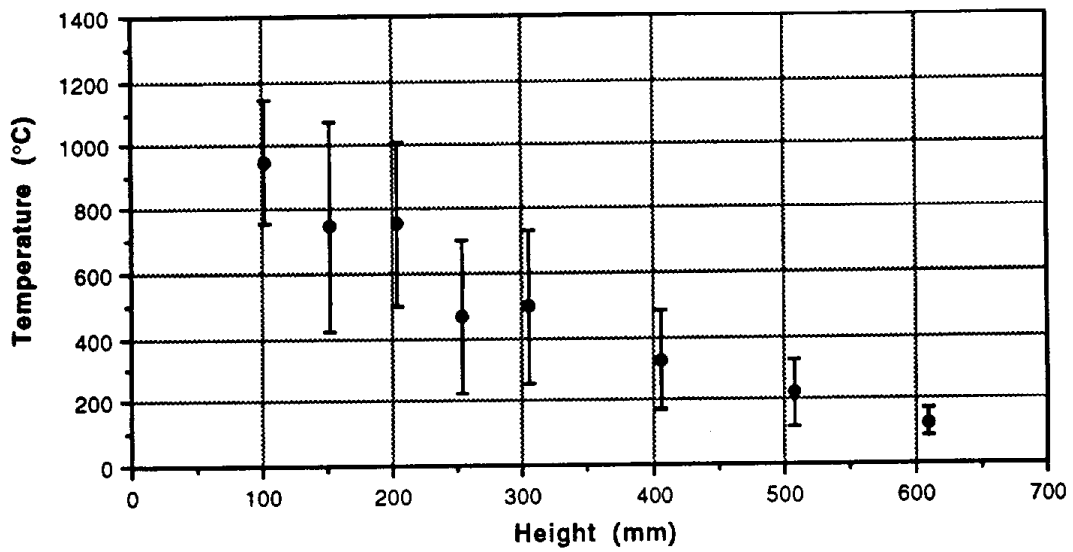


(a)

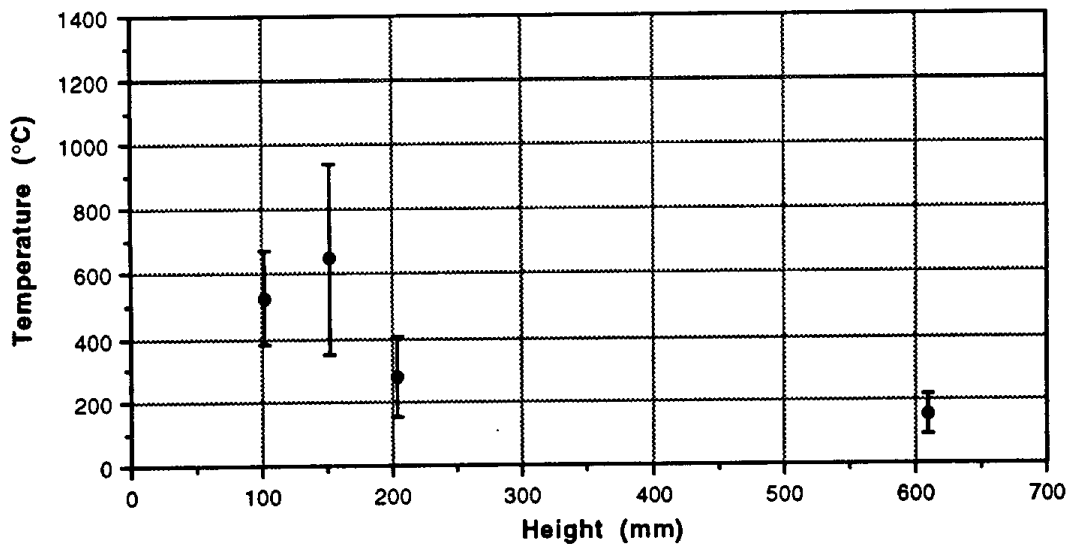


(b)

Figure 15. Temperature profiles showing mean and standard deviation for the CEWF high wind speed configuration. (a) upwards through flame center, (b) upwards over glowing combustion zone.



(a)



(b)

Figure 16. Temperature profiles showing mean and standard deviation for the CRNF low wind speed configuration. (a) upwards through flame center, (b) upwards over glowing combustion zone.

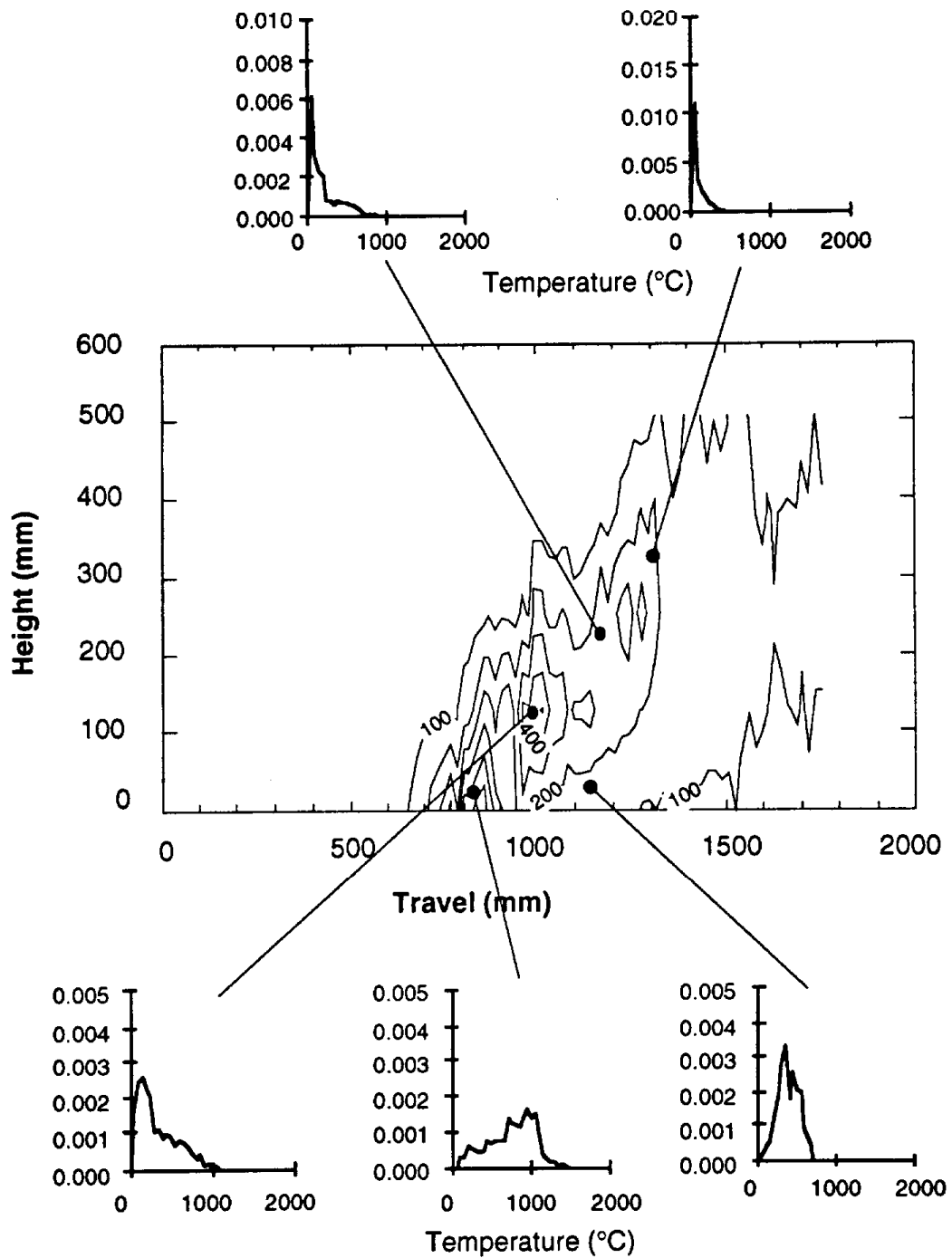


Figure 17. Temperature contours and relative frequency densities of temperature from fast response thermocouple at indicated positions in flame, CENF high wind speed configuration. Contour interval = 100°C, height given above fuel surface.

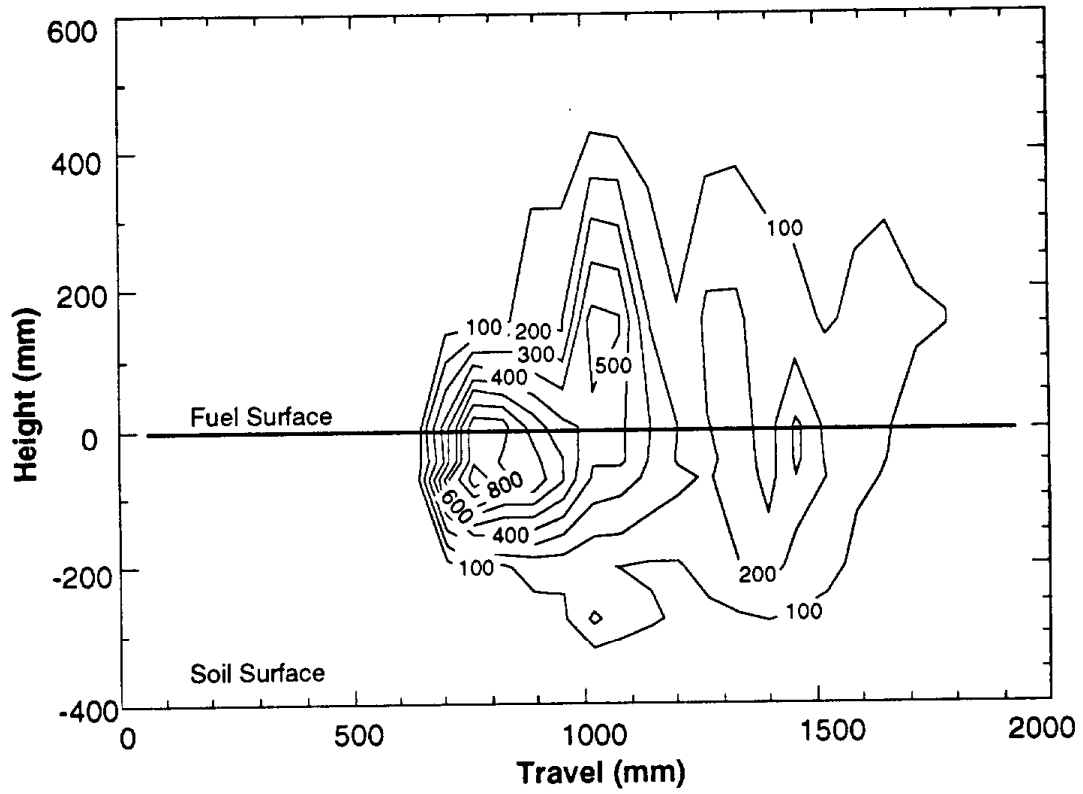
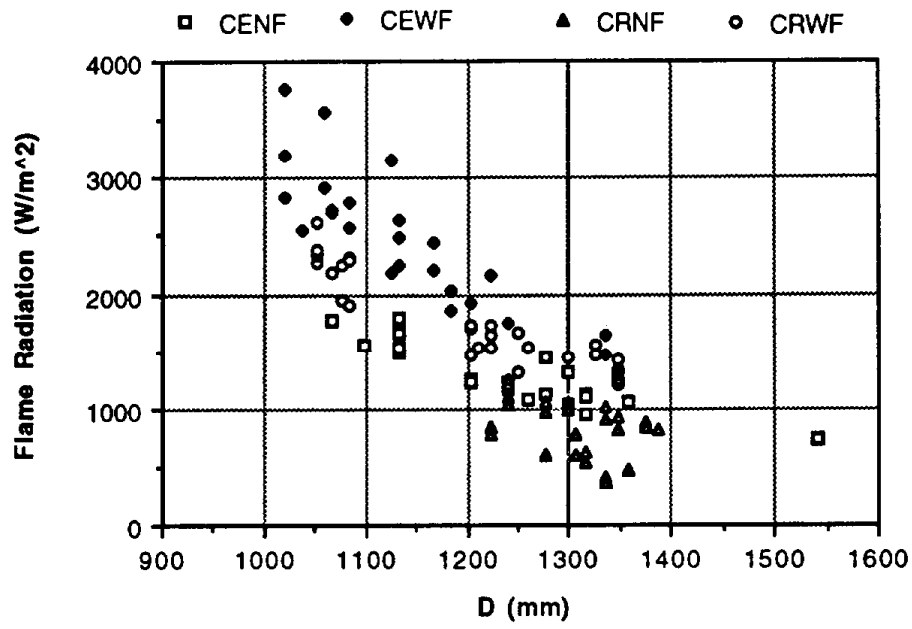
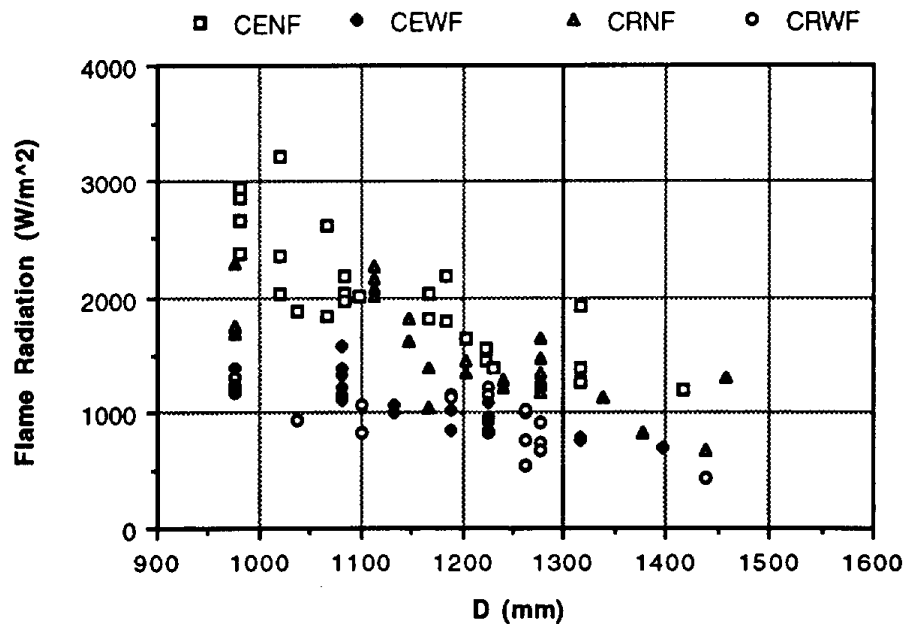


Figure 18. Temperature contours, field burn in rice straw spreading against the wind (Contour interval = 100°C).



(a)



(b)

Figure 19. Flame radiation for four configurations. (a) low wind speed, (b) high wind speed (see Figure 5 for definition of D).

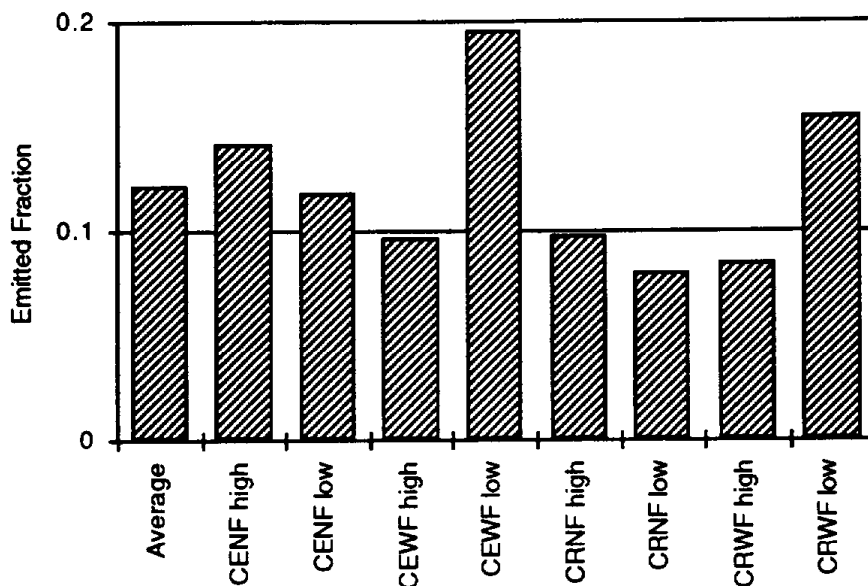


Figure 20. Radiation emitted as a fraction of total fire heat release.

Table 5. Total emitted power, heat release, and fraction emitted as flame radiation.

Configuration	Wind Speed	Total Emitted Power (W)	Fire Spreading Rate (m/min)	Total Heat Release Rate (W)	Emitted Fraction
CEWF	low	20,161	0.52	103,017	0.20
CEWF	high	8,991	0.47	93,112	0.10
CENF	low	12,179	0.52	103,017	0.12
CENF	high	16,915	0.60	118,866	0.14
CRWF	low	15,711	0.51	101,036	0.16
CRWF	high	8,335	0.50	99,055	0.08
CRNF	low	8,456	0.53	104,998	0.08
CRNF	high	13,332	0.69	136,696	0.10
Average		13,010	0.54	107,475	0.12

Local Gas Concentrations:

Gas concentrations measured in the flame region are listed in Table 6 for the CEWF high wind speed configuration, and in Table 7 for the CRNF low wind speed configuration. Concentration profiles for oxygen, carbon monoxide, and carbon dioxide through the flame center and over the glowing combustion zone behind the flame are plotted in Figure 21 for the CEWF high wind speed and in Figure 22 for the CRNF low wind speed configuration. The height is measured from the upper surface of the conveyor. The fuel depth is approximately 60 mm for these tests.

The lowest oxygen concentrations detected were about 5% in the flame near the fuel surface in both configurations. CO concentrations in the flame at the fuel surface were 7% in the CEWF configuration, and 9% in the CRNF configuration. CO<sub>2</sub> concentrations reached 13% and 14% for the CEWF and CRNF configurations, respectively. Approximately 250 mm behind the flame, the oxygen concentration decreased to 16% at the fuel surface in the CEWF configuration, but remained near ambient in the CRNF configuration.

Table 6. Local gas concentrations, CEWF, high wind speed.

Height above conveyor (mm)	254	152	76	76	152	76
Height above fuel surface (mm)	190	88	12	12	88	12
Distance behind flame front (mm)	483	229	64	64	330	254
Approximate location	flame tip	flame	flame	flame	behind flame	behind flame
Species						
H <sub>2</sub> (% v/v)	0.027	0.091	0.484	1.026	0.048	0.103
O <sub>2</sub> (% v/v)	20.739	17.259	11.613	5.207	19.575	15.687
N <sub>2</sub> (% v/v)	77.860	75.221	73.089	67.452	75.790	74.447
CO (% v/v)	ND	0.347	3.131	7.200	T	0.732
CO <sub>2</sub> (% v/v)	0.655	3.099	7.627	12.951	1.177	3.971
CH <sub>4</sub> (ppm)	170	372	3,363	7,687	70	280
C <sub>2</sub> H <sub>4</sub> (ppm)	10	169	1,553	3,609	26	120
C <sub>2</sub> H <sub>6</sub> (ppm)	50	16	251	651	5	T
C <sub>2</sub> H <sub>2</sub> (ppm)	1	86	525	1,164	7	20
Total	99.304	96.081	96.513	95.147	96.401	94.982

ND = not detected. T = trace.

Table 7. Local gas concentrations, CRNF, low wind speed.

Height above conveyor (mm)	406	254	152	102	64
Height above fuel surface (mm)	342	190	88	38	0
Distance behind flame front (mm)	229	190	127	102	64
Approximate location	flame	flame	flame	flame	flame
<b>Species</b>					
H <sub>2</sub> (% v/v)	0.036	0.072	0.250	2.394	2.590
O <sub>2</sub> (% v/v)	19.331	16.665	13.968	5.485	7.705
N <sub>2</sub> (% v/v)	77.584	78.004	76.491	66.526	66.774
CO (% v/v)	T	0.606	1.231	9.219	8.758
CO <sub>2</sub> (% v/v)	1.732	3.581	6.776	13.947	11.480
CH <sub>4</sub> (ppm)	140	620	940	15,670	15,350
C <sub>2</sub> H <sub>4</sub> (ppm)	30	200	710	8,200	10,170
C <sub>2</sub> H <sub>6</sub> (ppm)	<10	10	30	1,060	860
C <sub>2</sub> H <sub>2</sub> (ppm)	40	140	630	2,820	5,660
Total	98.704	99.025	98.947	100.346	100.511
Height above conveyor (mm)	610	152	102	64	
Height above fuel surface (mm)	546	88	38	0	
Distance behind flame front (mm)	330	280	178	254	
Approximate location	flame tip	behind flame	behind flame	behind flame	
<b>Species</b>					
H <sub>2</sub> (% v/v)	ND	0.027	0.043	0.019	
O <sub>2</sub> (% v/v)	20.578	19.748	20.318	20.437	
N <sub>2</sub> (% v/v)	78.503	77.097	76.971	77.270	
CO (% v/v)	ND	0.258	0.134	0.125	
CO <sub>2</sub> (% v/v)	0.941	1.240	0.758	0.749	
CH <sub>4</sub> (ppm)	20	160	110	40	
C <sub>2</sub> H <sub>4</sub> (ppm)	<10	<10	40	20	
C <sub>2</sub> H <sub>6</sub> (ppm)	<10	10	60	<10	
C <sub>2</sub> H <sub>2</sub> (ppm)	10	<10	ND	<10	
Total	100.025	98.387	98.245	98.606	

ND = not detected. T = trace.

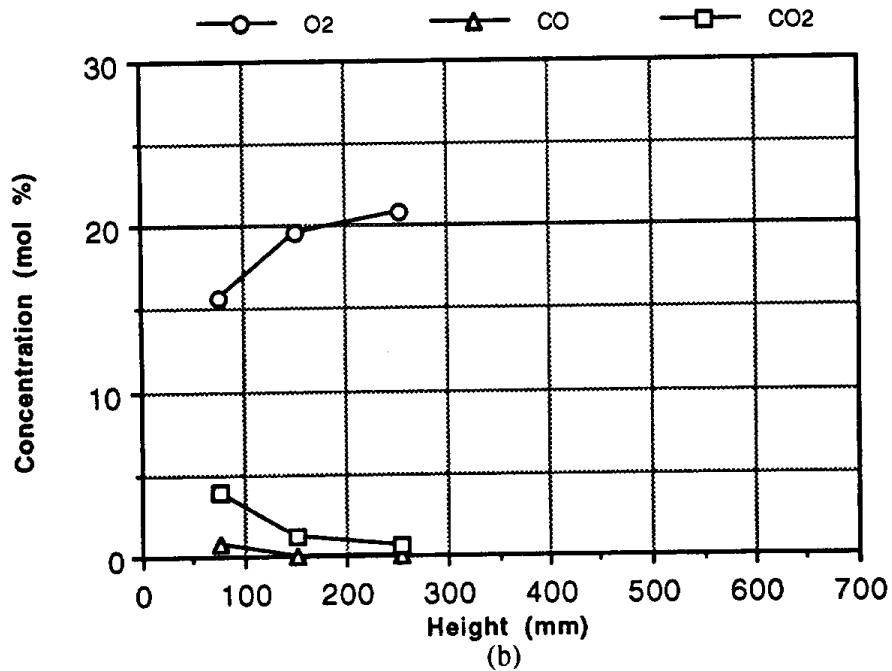
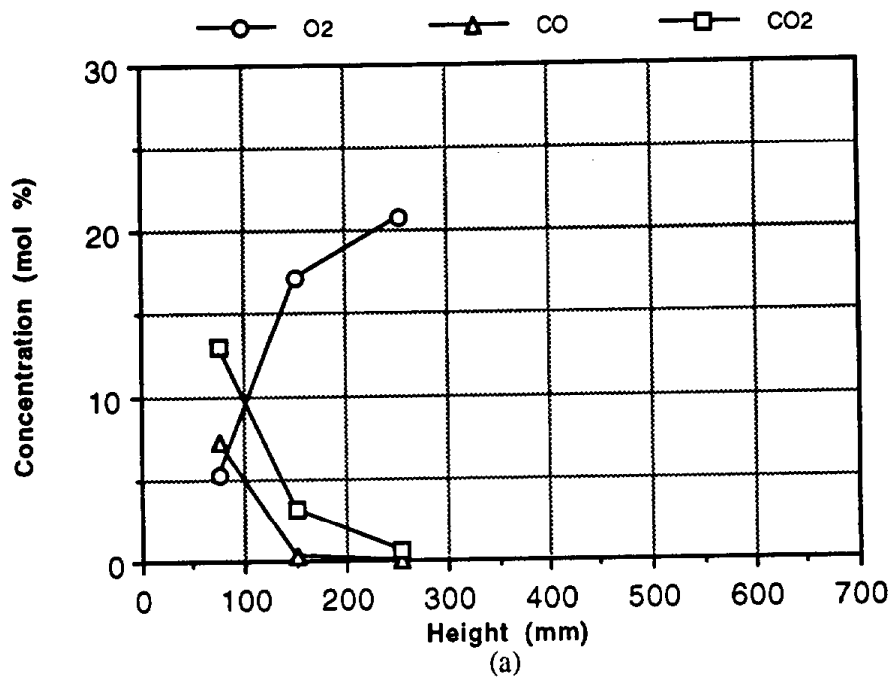


Figure 21. Gas concentration profiles for the CEWF high wind speed configuration. (a) upwards through the flame center, (b) upwards over the glowing combustion zone.

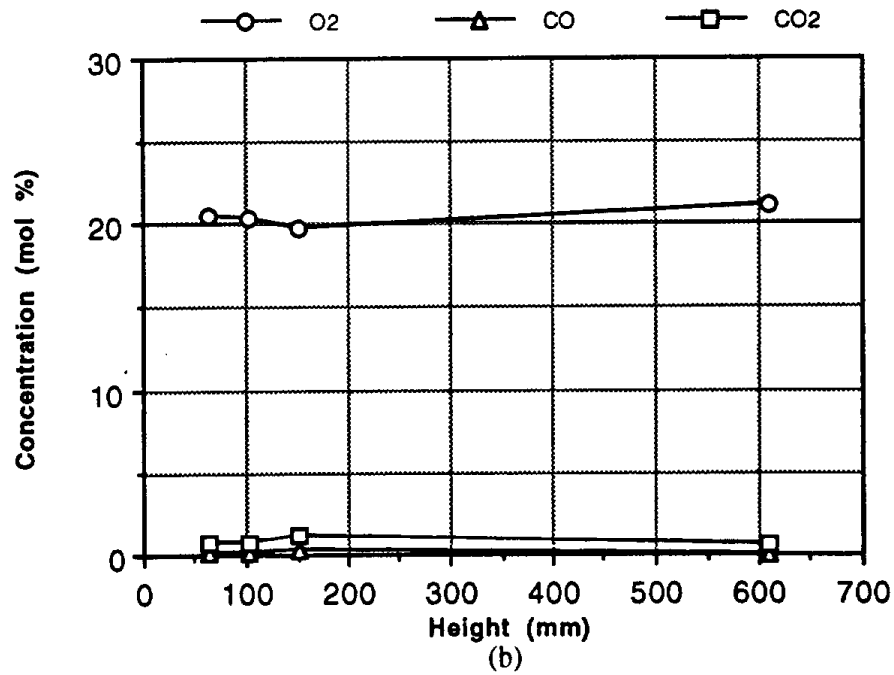
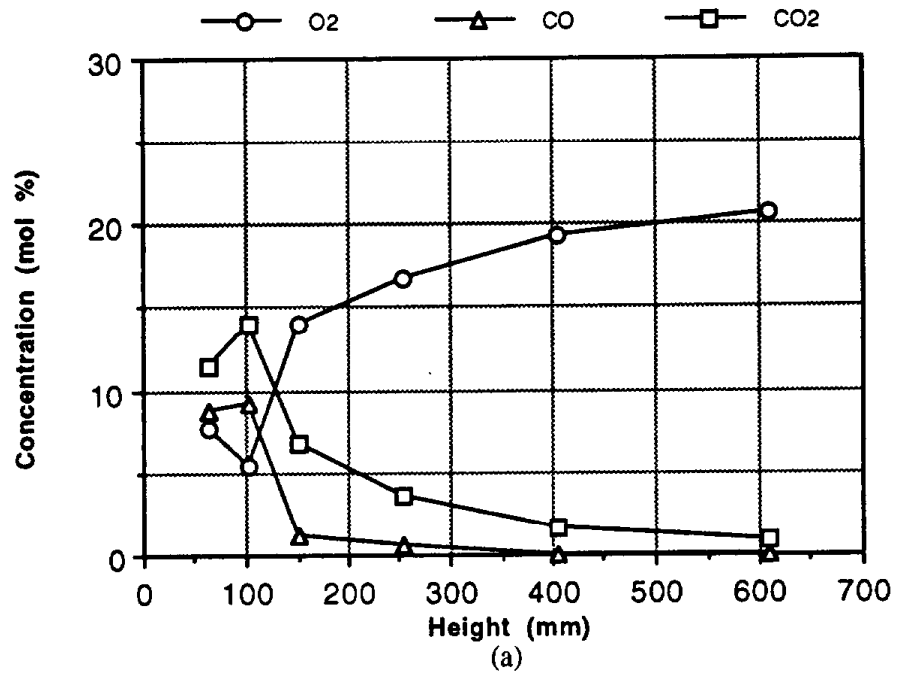


Figure 22. Gas concentration profiles for the CRNF low wind speed configuration. (a) upwards through flame center, (b) upwards over glowing combustion zone.

Maximum total hydrocarbon concentrations were 2.5 to 3% in the flame near the fuel surface in the CRNF configuration. The maximum concentration observed in the CEWF configuration was about 1%, also in the flame near the fuel surface. The concentrations drop off rapidly upwards. The pyrolysis products hydrogen, methane, ethylene, acetylene, and ethane were observed in quantity as expected for fuels of this type. The gas composition was, however, dominated by O<sub>2</sub> and N<sub>2</sub> until near the fuel surface where dilution was not so large or the products had not yet burned.

#### Soot Volume Fractions:

Vertical profiles of soot volume fraction are plotted against height above the conveyor in Figure 23a for the CEWF high wind speed configuration and in Figure 23b for the CRNF low wind speed configuration. Shown on each graph are five profiles at positions along the surface extending from the point at which the fire first begins to pass the location of the beam (0 mm), in the flame (67 - 220 mm), over the glowing combustion zone (520 - 630 mm), and well behind the flame over the char smoldering zone (1200 - 1330 mm). The peak volume fractions were higher for the CRNF low speed configuration, and there was a higher concentration in the plume behind the fire as well, which is consistent with the higher PM emission for this configuration.

Under both conditions of wind speed the maximum soot loading was obtained at about 200 mm behind the front edge of the fire. Peak soot volume was found about 100 mm above the fuel surface in the low speed case and about 50 mm above the fuel in the high speed case. The soot peaks are located near the center of the flame in each case. Profiles taken behind the flames show that the soot loading increases at large heights above the fuel bed, suggesting a plume of smoke that is evolved from the fire. The relatively small values of extinction that were obtained at the far downstream locations near the fuel bed may be due to smoldering combustion in the bed which continues to yield some particles.

#### Discussion

Turbulent flows are characterized by a range of length scales from the largest energy-containing eddies that are described by the integral length scale down to the smallest scales of the flow, the Kolmogorov scales, in which viscous dissipation terminates the cascade of energy through the spectrum. When a flow contains chemically reacting zones within it,

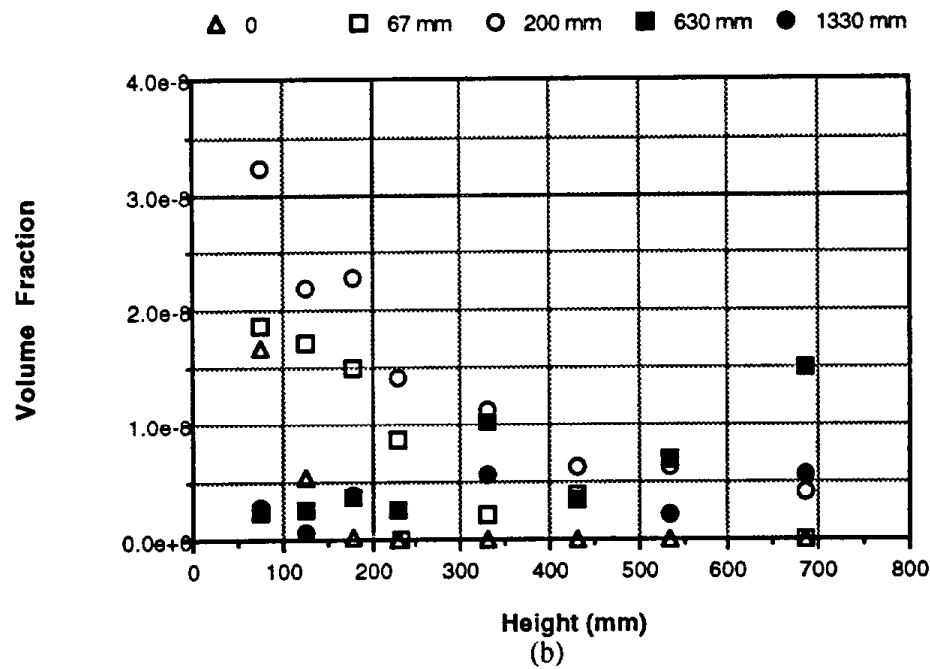
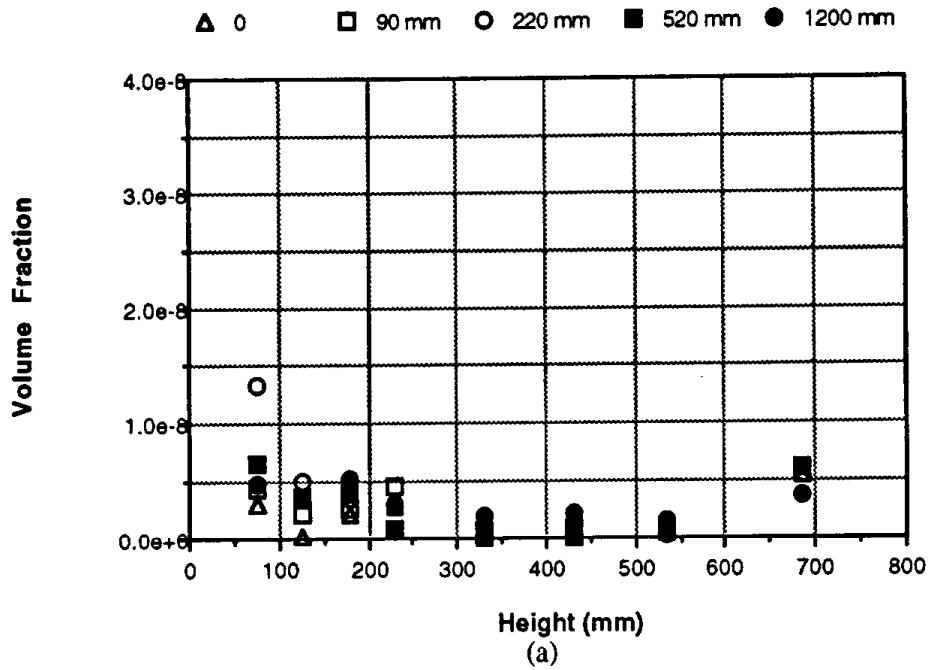


Figure 23. Profiles of soot volume fraction for five streamwise positions. (a) CEWF high wind speed, (b) CRNF low wind speed. Positions shown are distances downstream from the leading edge of the fire.

such as a flame, it is useful to compare the length or time scales of the turbulence with characteristic length or time scales of the reaction zone. A comparison of these scales serves to identify regimes of combustion (28) which may extend from a distributed reaction zone regime that resembles a chemical reactor to a system that resembles laminar flamelets that are strained and contorted by the turbulent flow field. An analysis of these time or length scale ratios is instructive in terms of determining if model experiments behave in a similar manner to full-scale systems. Variations in these ratios may affect the structure of the flame and the emission of pollutants. A fundamental comparison of time scales in combustion is the Damköhler number,  $Da$ , which relates a characteristic fluid mechanical time scale,  $\tau_F$  to a time scale for chemical reaction,  $\tau_C$ , i.e.,

$$Da = \frac{\tau_F}{\tau_C} \quad [17]$$

As  $\tau_C \rightarrow 0$  the reactions tend towards equilibrium. As  $\tau_F \rightarrow 0$  and  $Da$  approaches zero the reactions are far from equilibrium as the chemistry cannot keep up with the supply of reactants that is imposed by the flow field. In a turbulent flow it is possible to associate the fluid time scale with the turbulence characteristics, in particular, the turbulence intensity and a length scale. Most mixing in turbulent flows is due to the large eddies so that an appropriate fluid time scale would be the large eddy life time, found in terms of the integral length scale,  $\ell$ , and the turbulence kinetic energy,  $E_k$ , as

$$\tau_F = \frac{\ell}{\sqrt{2E_k}} \quad [18]$$

The integral length scale was found by examination of the velocity spectra and velocity autocorrelations as described earlier. Results of spectral analyses on both the CEWF high speed and CRNF low speed configurations were given in Figure 11 and 12, respectively. The spectra cover approximately 2.5 decades up to the maximum frequency allowed by the sampling (1100 Hz or half the sampling frequency).

Approximate turbulent kinetic energies were estimated from the anemometer data by assuming the intensities of the vertical and transverse fluctuations were half that of the streamwise, whence

$$E_k = \frac{3}{4} \overline{u'^2} \quad [19]$$

where  $\overline{u'^2}$  is the variance of the velocity fluctuations in the streamwise direction, as before. The time scale for chemical reaction will be approximately the same for rice straw combustion in both the wind tunnel and in the field burn. Therefore, the question of comparative Damköhler numbers becomes one of relative turbulence kinetic energies and length scales.

For the CEWF high wind speed configuration, at a typical height of 200 mm (approximate height of the flame tip), the rms velocity fluctuation is about  $0.5 \text{ m s}^{-1}$ . The value of  $E_k$  is then about  $0.19 \text{ m}^2 \text{ s}^{-2}$ . The integral length scale at this height is 0.16 m; this yields an approximate fluid time scale of 260 ms. In the CRNF low speed configuration at 200 mm height, the rms velocity fluctuation is about  $0.06 \text{ m s}^{-1}$ , the integral length scale is 0.12 m, and the corresponding fluid time scale is about 1700 ms. The time scales converge for the two configurations above 300 mm (Figure 24). Both are approximately 500 ms at 350 mm height. The low intensity of turbulence gives very large values for  $\tau_F$  outside the boundary layer (e.g., 800 mm height). The trend towards increasing time scale for the CRNF configuration as the fuel surface is approached is opposite that of the CEWF configuration.

Above the canopy of a field in an atmospheric boundary layer, the integral length scale is much greater than in the tunnel, of the order of 100 m (29). However, this length scale is clearly inappropriate in terms of mixing within a flame burning within the first 200 to 300 mm above the surface. In this case, a more appropriate measure of large scale turbulence would be of the order of the flame height; larger eddies would appear simply as an unsteadiness of the flow on the scale of the fire. Consequently, the relevant large length scales would be of the same order in both field and tunnel flows, i.e. a flame height of several hundred mm for the opposed flow condition over a straw layer. The estimated turbulence intensity in the atmospheric boundary layer is approximately 15% of the mean velocity at heights from 2 m to 30 m above the ground (30), and just above plant canopies measurements range from approximately 30% to 120% (22 - 24, 31). The lower values are typical of the turbulence intensities in the tunnel at the height of the fire. Consequently, the relevant large eddy time scale in the field will be of the order of 100 to 500 ms at similar wind speeds.

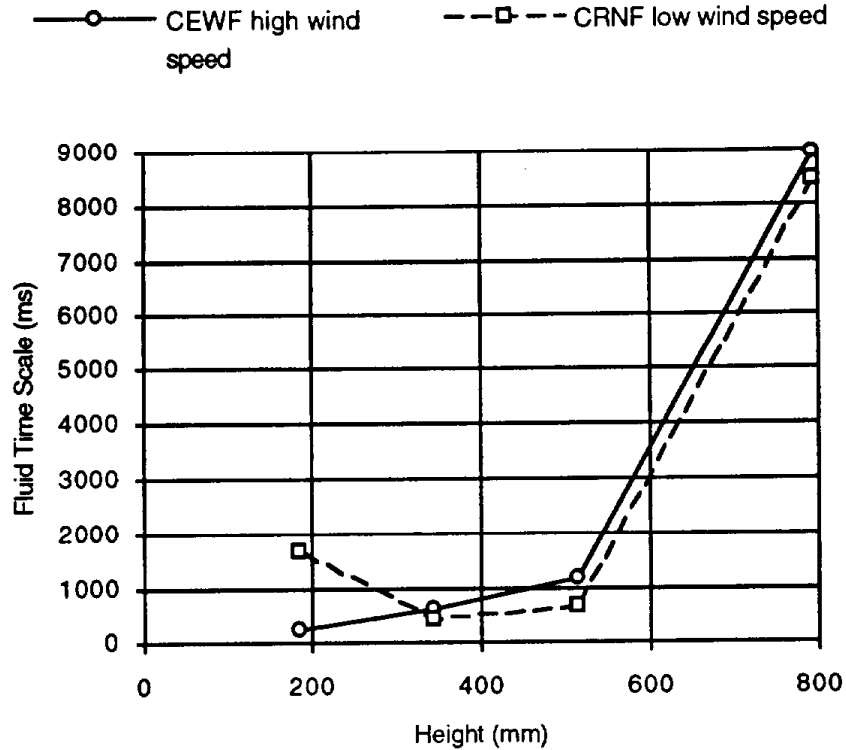


Figure 24. Estimated fluid time scales based on integral length scales and velocity fluctuations for the CEWF high wind speed and CRNF low wind speed configurations.

Another important comparison of scales relates to the local structure of the flame itself. This comparison necessitates an examination of the small length scales, the Kolmogorov scales, in relation to a characteristic flame thickness. The characteristic flame thickness depends on the local flow field which may be described in terms of the strain rate or, alternatively, the scalar dissipation rate. Following Peters (32), the typical thickness,  $\Delta y$ , of a laminar diffusion flame may be written as

$$\Delta y = \sigma_r \sqrt{\frac{2\mathcal{D}}{\chi_{st}}} \quad [20]$$

in which  $\sigma_r$  is a non-dimensional heat release rate,  $\mathcal{D}$  is a typical diffusivity and  $\chi_{st}$  is the scalar dissipation rate at the stoichiometric location. The latter quantity fluctuates in a

turbulent flame. It is very difficult to measure the mean scalar dissipation rate although estimates can be obtained from measurements of the turbulent kinetic energy and viscous dissipation rate. For the present purposes, it is necessary to estimate  $\chi_{st}$  from data for the extinction of laminar diffusion flames. Methane is an appropriate choice to approximate the fuel in the flames although the fuel actually consists of dilute hydrogen and methane with CO. The value of  $\chi_{st}$  for methane-air flames is about  $8 \text{ s}^{-1}$ . The flames in this study are far from extinction. The upper limit of  $\chi_{st}$  is taken as  $1 \text{ s}^{-1}$ . At 1500 K, the diffusivity of nitrogen in air is about  $10^{-4} \text{ m}^2 \text{ s}^{-1}$ . From Peters (32), the value of  $\sigma_r$  for methane at a low strain rate is around 0.01. These values lead to a lower estimate of the characteristic flame thickness of 0.14 mm. Actual strain rates may be lower and would lead to higher values of  $\sigma_r$  and smaller values of  $\chi_{st}$ . Typical flame thicknesses may then be somewhat greater.

The Kolmogorov scale in the atmosphere is about 1 mm (29). In the CEWF high wind speed configuration, the Kolmogorov scale was estimated to lie in the range of 0.1 to 0.5 mm. The uncertainty was greater in the case of the CRNF low wind speed configuration, where the Kolmogorov scale was estimated to lie in the range of 0.2 to 3 mm. The flame thickness is of the same order or slightly larger than the estimated Kolmogorov scales, at least where a reasonably well developed boundary layer can be observed. Although the conditions for a flamelet description of the flame structure may not be rigorously satisfied, we may expect nevertheless that the structure of the flames will be similar in the field and in the wind tunnel, given the similarity of the flame kinetics and the Kolmogorov scales. A similar conclusion applies with regard to the large scale structures of the flames in the field and tunnel.

In the case of the CEWF configuration, it has been possible to estimate surface roughness heights and friction velocities from models of the flow based on the logarithmic law-of-the-wall. With the higher wind speed,  $20 \leq z_0 \leq 50 \text{ mm}$ , and  $0.4 \leq u^* \leq 1.2 \text{ m s}^{-1}$ . At lower wind speeds,  $z_0 \cong 100 \text{ mm}$ , and  $0.4 \leq u^* \leq 0.6 \text{ m s}^{-1}$ . Similar conditions apply to the CRNF high wind speed configuration, in which  $40 \leq z_0 \leq 90 \text{ mm}$ , and  $0.5 \leq u^* \leq 0.6 \text{ m s}^{-1}$ . However, for the CRNF low wind speed configuration, the logarithmic law-of-the-wall model is not appropriate to determine  $z_0$  and  $u^*$ . Roughness heights for the atmosphere were reported by Counihan (30) to range from 1.4 mm over open ground to 150 mm over rural terrain. A grassy surface with height 150 mm was reported to have a roughness height of 6.6 mm. Raupach (20) gave  $z_0$  from 15 to 50 mm for wheat fields depending on canopy height, and 4 to 10 mm for model crops and regularly arrayed elements in wind tunnels. Sutton (33) estimated  $z_0$  to be 20 mm over a 50 mm tall grass.

Estimates from Counihan show the friction velocity for the lower atmosphere to be of the order of 0.2 to 0.4 m s<sup>-1</sup> (30). For the experiments described here, the higher wind speeds and the configurations with the ceiling extended give values of  $z_0$  and  $u^*$  which are at least comparable with atmospheric values. The values of  $z_0$  computed from the CRNF low wind speed velocity profiles are not.

That the flame temperature profiles are affected strongly by the change in wind tunnel conditions is immediately apparent from Figures 13 and 14. As one would expect, the flame burning under the high velocity conditions is bent over by the approaching flow and appears to be considerably shorter than the low speed flame. The peak temperatures that were measured under both conditions were similar, about 1200 to 1300°C although it must be born in mind that these temperatures represent lower bounds due to the averaging effect of the thermocouple which had a finite response time to flame fluctuations. The accompanying frequency distributions of temperature at similar positions in both flames are quite similar in both cases. The most interesting distributions are at the foot of the flames. The distributions appear to be bi-modal, with the lower mode indicating free stream cold air at these locations. The form of the distributions may be important eventually in understanding the sources of NO in these flames; measurements of NO were not obtained however in these tests.

The reduction in the flame height with the increase in wind speed suggests that mixing may be enhanced. The estimates of the time scale for large eddy mixing showed that in the high speed condition this time scale was about 300 ms near the surface, and about 6 times this value in the low speed case. Therefore, it is plausible, and not unexpected, that increased wind speed would improve the mixing rates of fuel and air in these diffusion flames. This is supported by an examination of the probe sampling results through the flame that were presented in Figures 21 and 22. In particular, the O<sub>2</sub> concentration profiles are of interest. At low speeds, the O<sub>2</sub> mole fraction reaches the free stream value at about 400 to 500 mm above the fuel bed. On the other hand, at high speeds the free stream O<sub>2</sub> mole fraction is attained at a height of 200 mm above the fuel bed. CO and CO<sub>2</sub> concentrations confirm the trend. It is worth noting that there are no significant differences (within the experimental uncertainty) in the O<sub>2</sub>, CO<sub>2</sub> and CO concentrations near the fuel bed at the flame location with and without the floor. However, the O<sub>2</sub> concentration is lower and the product concentrations are higher downstream of the flame front when the floor is present. This observation suggests that transport of air through the floor may be important in the downstream smoldering zone.

Laser extinction was used to measure line-of-sight soot volume fractions. Typical peak values measured in the flames were of the order of  $10^{-8}$ . Much higher values have been obtained in measurements of the local soot volume fractions in hydrocarbon flames. For example, Santoro, et al. (16) reported peak values of about  $10^{-5}$  in a laminar ethylene air diffusion flame. Neill and Kennedy (34) measured values of about  $6 \times 10^{-7}$  in a turbulent ethylene air flame and about  $2 \times 10^{-7}$  in a turbulent propane air flame. Portions of the laser path were outside the flame region because it was necessary to define the path length in terms of the tunnel width due to the unsteadiness of the flame. No other satisfactory measure of the path length was possible. For this reason, the reported soot volume fractions are much lower than one would obtain by measuring over a much shorter distance through a laminar or confined turbulent diffusion flame.

It is apparent from comparing the two sets of profiles that the wind speed has an important impact on the soot formation within the fire itself. The soot loading under the low speed conditions is about a factor of three higher than for the high speed flame. The trend is consistent with the results on particulates that were obtained from particulate sampling in the stack of the wind tunnel although the effect is greatly diminished through sampling in the stack gases.

Soot formation in flames is a relatively slow process and its kinetics are far from equilibrium. Therefore, the amount of soot that forms in a diffusion flame depends critically on the time that is available. A shorter residence time will lead to a reduction in the amount of soot that forms. Both laminar and turbulent diffusion flames exhibit this effect. Increasing the flow rate of fuel in a laminar diffusion flame will increase the amount of soot that forms as a result of the greater length of the flame. Eventually, the flame will start to emit soot when it reaches its so-called sooting height (35). On the other hand, a turbulent flame at a fairly high Reynolds number does not change its height as the flow rate of fuel is increased. Instead, the intensity of the turbulence and the mean velocity increase. As a result, the rate of mixing of fuel and air increases and less soot forms (36). These examples serve to demonstrate the impact of residence times or mixing rates on soot production. Increases in mixing rates within the rice straw flames are manifested as a reduction in the soot loading.

The magnitudes of the PM emission factors determined here can be compared with those of Darley (4,5), who was also able to perform direct mass balances for computing the

emission factor. At similar moisture content (8-10% wet basis), Darley reports three values for backing fires in rice straw: 0.11% (5), 0.35% (4, fuel bed on a 25° slope), and 0.46% (4, fuel bed on a 15° slope). The PM emission factor in the 64 tests over all four configurations of the wind tunnel using the same source of straw for all tests ranged from a low of 0.45% (CEWF, 3.4 m s<sup>-1</sup>) to a high of 0.79% (CRNF, 2.2 m s<sup>-1</sup>). The lowest values here are about the same as the highest values obtained by Darley. Rice straw from other sources tested at the same moisture and loading rate have subsequently yielded values as low as 0.2% in the CEWF high wind speed configuration. MMAD found here of approximately 0.1 µm are similar to those reported for field burns with rice straw (8). Reasons for the differences between the results reported here and those of Darley are therefore uncertain, but may be due to differences in the burning conditions, fuel composition, or sampling technique. Some effects due to differences in burning conditions have been noted above. Differences due to sampling technique probably exist; the wind tunnel samples were withdrawn from the stack flow at lower temperatures than Darley encountered (4,5), and this could affect aerosol particle mass. Influences of physical and chemical differences within fuels of the same type have not been explored, and make for interesting future work.

## Conclusions and Recommendations

Average emission factors for particulate matter were found to differ significantly among the four wind tunnel configurations, ranging from 0.5% for the ceiling extended configuration with the floor installed and the wind speed over 3 m s<sup>-1</sup>, to 0.7% for the ceiling retracted configuration without the floor and the wind speed at 2 m s<sup>-1</sup>. Significant differences were observed with the floor installed, which tends to reduce the emission factor, and for the wind speed, which when increased tends also to reduce the emission factor. The ceiling position by itself was not found to significantly alter the emission factor. Instead, the effect of the ceiling position appears to be related to the change in wind speed at the fire. With a higher wind speed in the ceiling retracted configuration, PM emission factors were comparable to those obtained with the ceiling extended.

Velocity profiles from tests with low wind speeds and the ceiling retracted are distinctively different from those of other tests. A region of very low velocity extends upward from the fuel surface for 100 to 200 mm, and suggests an extremely adverse pressure gradient with separated flow.

The gas sampling results did not suggest significant effects of the tunnel floor on the gas composition near the fuel bed at the front of the flame. Further downstream it is possible that air flow through the smoldering bed is important. The laser measurements lend credence to the hypothesis that the wind speed is a dominant parameter in the emission of particles, especially soot which is an important component of the stack particulate loading. Estimates of fluid mechanical time scales from velocity measurements support these observations. Some correlation between wind speed and particulate loading may be expected on the basis of these results.

Measures of soot volume fraction by laser light extinction were about  $10^{-8}$  and are at least an order of magnitude lower than values commonly reported for turbulent flames. The path length of the light could only be defined in terms of the tunnel width, as the true path length in the flame could not be determined. The low values of soot volume fraction are indicative of the unsteadiness of the flames. Trends in soot volume fraction are consistent with PM measurements in the stack, showing increased levels for the lower wind speed and ceiling retracted conditions.

Peak temperatures measured in the flames were similar under all configurations although flame temperature profiles were affected strongly by wind speed. Flames burning under higher wind speed conditions were bent over and considerably shorter than those burning under lower speed conditions, especially with the ceiling retracted. Temperature distributions at the foot of the flames near the fuel surface were bi-modal, with the lower mode indicating free stream cold air at these positions. Temperature contours down to the fuel surface obtained in the wind tunnel under the CENF high wind speed configuration were quite similar to those obtained during an actual field burn in rice straw conducted under similar conditions of wind speed and direction. The average PM emission factor for the CENF high wind speed configuration was intermediate to the emission factors of the CEWF high wind speed and CRNF low wind speed configurations.

Local turbulence intensities in the wind tunnel boundary layer were in the range of those expected for the field. Measurements just above the fuel surface in the wind tunnel extend up to about 35% intensity for the CEWF high wind speed configuration, and 65% for the CRNF low wind speed configuration. Values reported for the field just above plant canopies range from about 30% to 120%. Estimates of friction velocities and surface roughness heights computed from a logarithmic law-of-the-wall model for the ceiling extended configurations and the higher wind speed ceiling retracted configurations seem

also to compare reasonably well with values reported for the field. Wind tunnel friction velocities from 0.4 to 1.2 m s<sup>-1</sup> are somewhat higher than values reported for the lower atmosphere of 0.2 to 0.4 m s<sup>-1</sup>. Atmospheric surface roughness heights range from 1.4 mm to 150 mm over open ground and rural terrains. Wind tunnel roughness heights range from about 20 to 130 mm. The velocity profiles for the low wind speed ceiling retracted configurations do not fit a logarithmic law-of-the-wall model.

The total variation in average PM emission factor amounts to 35% out of the global mean for the four configurations. This variation is surprisingly narrow given the distinct differences in the appearance of the fire under the different configurations. Emission factors were significantly different, however, and the effect of changing the configuration with other fuel types was not evaluated. It is recommended that the two configurations yielding the extremes in PM emission factor (CEWF high wind speed and CRNF low wind speed) be used in further experiments with spreading fires. The influence of wind tunnel configuration on particulate matter and other emissions can thereby be explored. Average values should yield suitable measures of field emission factors for the purposes of determining offset allowances.

### **Acknowledgements**

The authors acknowledge and appreciate the support of Jim Mehlschau, Lowell Jahn, Burt Vanucci, Charles Barden, Wayne Andrade, and other members of the University of California, Davis, Engineering Mechanical Shop. Monem Beitelmal provided much assistance in carrying out the experiments described in the report. The authors are indebted to Andrew Wortman, Jack Paskind, Manjit Ahuja, and Robert Grant of the California Air Resources board for their support of this project, and to Forman Williams of the University of California, San Diego, for his thorough review of the manuscript.

## References

- (1) Jenkins, B.M.; Turn, S.Q.; Williams, R.B. *Agriculture, Ecosystems and Environment* 1992, 38, 313-330.
- (2) Jenkins, B.M.; Turn, S.Q.; Williams, R.B. *California Agriculture* 1991, 45(4), 12-16.
- (3) Darley, E.F. *Air pollution from forest and agricultural burning*. CARB Project 2-017-1, Statewide Air Pollution Research Center, University of California, Riverside, CA 1972.
- (4) Darley, E.F. *Emission factors from burning agricultural wastes collected in California*. Final Report, CA/ARB Project 4-011, Statewide Air Pollution Research Center, University of California, Riverside, CA 1977.
- (5) Darley, E.F. *Hydrocarbon characterization of agricultural waste burning*. Final report, CARB Project A7-068-30, Statewide Air Pollution Research Center, University of California, Riverside, CA 1979.
- (6) EPA. *Compilation of air pollutant emission factors*, Volume 1, AP-42 U.S. Environmental Protection Agency, Research Triangle Park, NC 1985.
- (7) Boubel, R.W.; Darley, E.F.; Schuck, E.A. *APCA Journal* 1969, 19(7), 497-500.
- (8) Goss, J.R.; Miller, G.E. *Study of abatement methods and meteorological conditions for optimum dispersion of particulates from field burning of rice straw*. ARB Project 1-101-1, University of California, Davis, CA 1973.
- (9) Carroll, J.J.; Miller, G.E.; Thompson, J.F.; Darley, E.F. *Atmos. Environ.* 1977, 11, 1037-1050.
- (10) Jenkins, B.M.; Chang, D.P.Y.; Raabe, O.G.; Jones, A.D.; Miller, G.E.; Turn, S.Q.; Williams, R.; Teague, S.; Mehlschau, J.; Raubach, N.; Uyeminami, D. *Development of test procedures to determine emissions from open burning of agricultural and forestry wastes*. Phase I Final Report, Contract No. A5-126-32, California Air Resources Board, Sacramento, CA 1990.
- (11) Jenkins, B.M.; Turn, S.Q.; Williams, R.B.; Chang, D.P.Y.; Raabe, O.G.; Paskind, J.; Teague, S. Chapter 37 in Levine, J.S. (ed.), *Global Biomass Burning: Atmospheric, Climatic, and Biospheric Implications*, MIT Press, Cambridge, MA 1991.
- (12) California Air Resources Board. *Stationary Source Test Methods*, Vol. 1, Sacramento, CA 1987.
- (13) Williams, R.B. *A wind tunnel investigation of the turbulent flow upstream of a freely spreading fire*. Unpublished M.S. dissertation, University of California, Davis 1992.
- (14) Tennekes, H.; Lumley, J.L. *A First Course in Turbulence*, MIT Press, Cambridge, MA 1972.
- (15) Hinze, J. O. *Turbulence*, McGraw-Hill, New York, N.Y. 1975.

- (16) Santoro, R.J.; Yeh, T.T.; Horvath, J.J.; Semerjian, H.G. *Combustion Sci. Tech.* **1987**, *53*, 89-115.
- (17) Bradley, D.; Entwistle, A.G. *Brit. J. Appl. Phys.* **1961**, *12*:708.
- (18) Hall, S.G. In-situ measurement of line-of-sight soot volume fraction by laser light extinction in a combustion wind tunnel. Unpublished M.S. dissertation, University of California, Davis 1992.
- (19) Dalzell, W.H.; Sarofim, A.F. *Trans. ASME:J. Heat Transfer*, **1969**, *91*:100-104.
- (20) Raupach, M.R.; Antonia, R.A.; Rajagopalan, S. *Appl. Mech. Rev.* **1991**, *44*(1), 1-25.
- (21) Stein, W.; White, B.R.; Kavanagh, J.; Brucker, D.; Castro, E.; Bagheri, N.; Strataridakis, C.J. *Wind-tunnel study of atmospheric dispersion of exhausts from the stack of building 222*. Lawrence Livermore National Laboratory, UCRL-21200, Livermore, CA 1989.
- (22) Maitani, T. *Boundary-layer Meteorology* **1979**, *17*, 213-222.
- (23) Ohtaki, E. *Boundary-layer Meteorology* **1980**, *19*, 315-336.
- (24) Ohtou, A.; Maitani, T; Seo, T. *Boundary-layer Meteorology* **1983**, *27*, 197-207.
- (25) Cebeci, T; Smith, A.M.O. *Analysis of Turbulent Boundary Layers*, Academic Press, New York 1974.
- (26) White, F.M. *Viscous Fluid Flow*, McGraw-Hill, New York 1974.
- (27) Flower, W.L. *Combustion Flame* **1989**, *77*, 279-293.
- (28) Williams. F. A. *Combustion Theory*, 2nd edition, Benjamin/Cummings, Menlo Park, CA 1985.
- (29) Wyngaard, J. C. *Probing the Atmospheric Boundary Layer*, Donald H. Lenschow, Editor, American Metrological Society, Boston MA 1986.
- (30) Counihan, J. *Atmos. Environ.* **1975**, *9*, 871-905.
- (31) Cionco, R.M. *Boundary-layer Meteorology* **1972**, *2*, 453-465.
- (32) Peters, N. 1991. Length scales in laminar and turbulent diffusion flames, in E.S. Oran and J.P. Boris, eds., Numerical approaches to combustion modeling, *Progress in Astronautics and Aeronautics*, v. 135.
- (33) Sutton, O.G. *Atmospheric Turbulence*, John Wiley and Sons, New York 1960.
- (34) Neill, T. ; Kennedy, I. M. *A.I.A.A. J.* **1991**, *29*, 932-935.
- (35) Haynes, B S.; Wagner, H. Gg. *Prog. Energy Combustion Sci.* **1981**, *7*, 229-273.
- (36) Kent, J. H.; Bastin, S.; *Combustion Flame* **1984**, *56*, 29-42.